Theses and Dissertations

1-2017

Plasmon-mediated Energy Conversion in Metal Nanoparticle-doped Hybrid Nanomaterials

Jeremy Dunklin
University of Arkansas, Fayetteville

Plasmon-mediated Energy Conversion in Metal Nanoparticle-doped Hybrid Nanomaterials

A dissertation submitted in partial fulfillment
of the requirements for the degree of
Doctor of Philosophy in Engineering

by

Jeremy R. Dunklin
Southern Arkansas University
Bachelor of Science in Engineering-Physics, 2012

May 2017
University of Arkansas

This dissertation is approved for recommendation to the Graduate Council.

_____
Dr. D. Keith Roper
Dissertation Director

_____   _____
Dr. Jingyi Chen   Dr. Lauren F. Greenlee
Committee Member   Committee Member

_____   _____
Dr. Robert H. Coridan   Dr. Jerry A. Havens
Committee Member   Committee Member

ABSTRACT

Climate change and population growth demand long-term solutions for clean water and energy. Plasmon-active nanomaterials offer a promising route towards improved energetics for efficient chemical separation and light harvesting schemes. Two material platforms featuring highly absorptive plasmonic gold nanoparticles (AuNPs) are advanced herein to maximize photon conversion into thermal or electronic energy. Optical extinction, attributable to diffraction-induced internal reflection, was enhanced up to 1.5-fold in three-dimensional polymer films containing AuNPs at interparticle separations approaching the resonant wavelength. Comprehensive methods developed to characterize heat dissipation following plasmonic absorption was extended beyond conventional optical and heat transfer descriptions, where good agreement was obtained between measured and estimated thermal profiles for AuNP-polymer dispersions. Concurrently, *in situ* reduction of AuNPs on two-dimensional semiconducting tungsten disulfide (WS_2) addressed two current material limitations for efficient light harvesting: low monolayer content and lack of optoelectronic tunability. Order-of-magnitude increases in WS_2 monolayer content, enhanced broadband optical extinction, and energetic electron injection were probed using a combination of spectroscopic techniques and continuum electromagnetic descriptions. Together, engineering these plasmon-mediated hybrid nanomaterials to facilitate local exchange of optical, thermal, and electronic energy supports design and implementation into several emerging sustainable water and energy applications.

TABLE OF CONTENTS

LIST OF FIGURES

1. INTRODUCTION

1.1 Motivation

The accelerated pace of human development necessitates major advancement in sustainable water and energy technologies. Projections place half of the world's population and grain production at serious risk from water scarcity by 2050.[1] Membrane separations, like reverse osmosis or pervaporation, are an emerging alternative for efficient water purification.[2] Concomitantly, global warming and reliance on fossil fuels necessitate a shift towards clean, renewable energy. Advancements in solar and other renewable energy technologies have diminished fossil fuel dependence by 10% in recent years; however, significant work remains to meet policies aiming for 160 gigaton carbon dioxide emission reduction by 2035.[3] Thus, continued development of solar energy harvesting and storage schemes is of increasing importance. Herein, two material platforms featuring highly absorptive plasmonic gold nanoparticles (AuNPs) are developed to facilitate photon conversion into thermal or electronic energy for potential use in alternative chemical separation or light harvesting applications.

1.2 Key Advances

Plasmon resonant nanostructures offer an extraordinary ability to concentrate electromagnetic fields and confine light to sub-wavelength dimensions. However, resistive losses in plasmonic noble metal systems have traditionally hampered device performance.[4] Popular approaches to minimize losses include development of new plasmonic materials with low interband losses and high carrier mobility[4] or use of coupled lattice resonances in ordered arrays of traditional noble metal structures.[5,6] Alternatively, the work herein seeks to maximize femto- to picosecond

1

dissipation of plasmon energy into phonons in condensed matter dispersions or energetic electrons in adjacent two-dimensional (2D) semiconductors. Intense localized plasmonic heating has drawn considerable interest in biomedicine,[7–10] catalysis,[11,12] and chemical separations.[13–15] Electron injection from resonantly excited NPs into adjacent 2D semiconductors[16] could serve as an independent source of carriers in photocatalytic devices[17] and field-effect transistors.[18]

This work advanced three key elements of plasmonic energy conversion in systems containing small, highly absorptive AuNPs with negligible scattering cross-sections:

1. *Diffraction-enhanced optical extinction in 3D polymer dispersions*

2. *Comprehensive characterization of plasmonic heat dissipation in 3D polymer dispersions*

3. *Bulk processing and functionalization of 2D semiconductors by in situ AuNP reduction*

Diffraction-induced internal reflection at interparticle separations approaching the resonant wavelength, reported herein, enhanced optical extinction up to 1.5-fold in ca. 1 mm thick three-dimensional (3D) polymer films. This phenomenon does not appear in analogous 3D fluid dispersions and had been reported previously only in systems containing larger, scattering AuNPs arranged in regular lattices. Concurrently, heat dissipation following plasmonic absorption was extensively characterized for these 3D polymer dispersions. Excellent agreement was obtained between measured and theoretical descriptions extending beyond conventional optics and one-dimensional heat transfer. Finally, fabrication and processing of low-dimensional tungsten disulfide (WS$_2$) nanosheets were improved by *in situ* reduction of AuNPs, where monolayer content and resulting optoelectronic properties were enhanced beyond prior benchmarks. Improved Au-WS$_2$ broadband optical extinction and plasmonic dissipation into hot electrons was probed using a combination of far-field optical spectroscopy, numeric discrete dipole approximation, and near-field electron energy loss spectroscopy. Together, this study could offer

2

a new paradigm for engineering these hybrid plasmon-mediated nanomaterials containing highly absorptive plasmonic NPs for use in a variety of applications.

1.3 Organization

Chapters 2 through 4 broadly cover approaches and key results pertaining to the three key advances outlined above. Chapter 2 studies plasmonic optical extinction in AuNP-polymer nanocomposite films. Chapter 3 characterizes thermal dissipation of plasmon energy in AuNP-polymer nanocomposite films. Chapter 4 describes Au-decoration of low-dimensional WS_2 nanosheets and optoelectronic properties of resulting heterostructures. Chapter 5 presents prospective applications for both AuNP-polymer films and Au-WS_2 heterostructures. Chapter 6 summarizes work and outlines future research opportunities.

2. OPTICAL EXTINCTION IN GOLD NANOPARTICLE-POLYMER FILMS

The optical properties of gold nanoparticles (AuNPs) dispersed in transparent polymer have received significant interest for improved photovoltaics,[19] photonic circuitry,[20,21] membrane separations,[22] and sensing.[23,24] The optical response of plasmonic nanostructures, typically noble metals, are determined by the interaction between their conduction electrons and the electric field associated with incident light. Plasmons are the quantization of electron density oscillations in response to this external electric field. Surface plasmons propagate at the interface between a normal dielectric, i.e. air, and a material with a negative real dielectric function, i.e. Au. A localized surface plasmon resonance (LSPR) occurs at the light frequency that matches these plasma oscillations acting against the positive nuclei restoring force; LSPR is dependent on NP size,[25] material composition,[26] geometry,[5,27] and host environment.[28] Plasmon-photon interactions can enhance light trapping,[29,30] induce intense near-field effects,[5,6,28] and permit broadband coupled lattice resonances at dielectric interfaces.[5,6]

Absorption, scattering, and diffraction by particles smaller than the wavelength of light give distinct signatures in photonic systems.[31] Mie theory indicates the scattering contribution to LSPR extinction is ca. 1% for the AuNPs used primarily herein less than 20 nm in diameter; this effectively eliminates extinction due to multiple scattering effects present for 3D films containing larger, highly scattering AuNPs.[30,32] Optical extinction by NPs with negligible scattering cross-sections in the Rayleigh size regime results from resonant absorption[33] and is described by Beer-Lambert law for isolated particles[34] and colloidal[35] dispersions in homogeneous dielectric environments. Optical extinction resulting from interaction between these sub-wavelength particles and their local environment is often characterized using Maxwell Garnett effective

medium theory (EMT) for random dispersions or dipole approximations[36,37] for well-defined NP distributions. Wavelength-scale interference of transmitted, i.e. forward scattered, light due to an obstacle,[38] interface,[39] or applied field[40] may result in diffraction that contributes to total optical extinction. As examples, refraction in media containing sub-wavelength inclusions is describable by Snell's law,[41] while Kirchoff's equation defines diffraction from well-described obstacles like a single slit, grating, or circular aperture.[41] Characterizing interparticle interactions in nanocomposites with thicknesses and interparticle separations above and below the LSPR wavelength, λ_{LSPR}, could distinguish contributions to optical extinction arising from isolated AuNPs, interparticle interactions, and dielectric heterogeneity.

This chapter compares measured optical extinction spectra with theoretical predictions from Mie theory, CDA, and Maxwell Garnett EMT for AuNP-containing polydimethylsiloxane (PDMS) and polyvinylpyrrolidone (PVP) films. Optical response was studied across two AuNP sizes (negligible vs. highly scattering), two film thickness regimes (super- and sub-wavelength), and at order of magnitude differences in AuNP concentration (x 10^9 to 10^{15} NPs/cm^3). Most critically, resonant extinction per NP increased up to 1.5-fold as particle separation decreased below λ_{LSPR} in super-wavelength polydimethylsiloxane (PDMS) films after following Mie and EMT trends at particle separations greater than or equal to λ_{LSPR}. This optical extinction enhancement appeared attributable to diffraction-induced internal reflection. This comprehensive study of optical extinction in AuNP-polymer dispersions supports robust design of resonant plasmon optics in a variety of emerging flexible photonic devices.[42]

2.1 Interfacial reflection enhanced optical extinction in AuNP-PDMS films

In this section, AuNPs were dispersed in polydimethylsiloxane (PDMS) due to unique chemical, physical, and optical properties that support study of plasmonic optical activity and implementation into optoelectronic and biochemical applications.[43] For example, the optical transparency across visible wavelengths allows facile study of AuNP optical excitation and thermal dissipation.[44] PDMS crosslinks as it cures and silicon hydride groups in the crosslinking agent are available to reduce gold (III) chloride ($AuCl_3$) into AuNPs within the polymer matrix.[45,46] This *in situ* reduction has produced films with superior optothermal characteristics.[22] However, uncertainty in resulting AuNP sizes and concentrations inhibits fundamental characterization of plasmonic effects, thereby necessitating development and focused study of well-defined homogeneous dispersions of solution-synthesized AuNPs.

2.1.1 Initial evidence of extinction enhancements due to internal reflection

First-generation AuNP-PDMS films containing random dispersion of solution-synthesized AuNPs provided the first evidence of enhanced optical extinction as due to internal reflection. In the initial study, optically extinguished power, with possible contributions from scattering and diffraction, was distinguished from resonant power absorbed by comparing measured spectral extinction and independently obtained estimates of Mie absorption based on Beer-Lambert law. Internal reflection due to diffraction and/or scattering was distinguished from absorption and external reflection by geometric optical measures. AuNP-PDMS extinguished power based on measured spectral extinction (filled purple squares), ideal Beer-Lambert absorbable power based on AuNP concentration (red dashed line), and extinguished power after correction for internal reflection (hollow purple squares) are plotted in Figure 1a. All values are taken near resonance at

532 nm and are based on 100 mW of total power; these values represent the excitation wavelength and incident power used in subsequent thermal characterization discussed in Chapter 3. Mass-percent Au, taken as the mass of Au divided by total film mass, ranged from 0.002 to 0.005 mass-percent. Multiplying Au concentration of each film in nanomoles (nmol) by its measured thickness resulted in comparable planar Au densities in units of nmol Au per square centimeter: 5.31, 6.97, 10.2, and 13.4 nmol/cm^2. This was done to normalize extinguished power for films with variations in thickness. Equivalent AuNP concentrations ranged from 0.469 to 1. 17 x 10^{12} NPs/cm^3. Unmagnified images and measured UV-vis extinction spectra of each first-generation AuNP-PDMS film are shown in Figure 1a and 1b, respectively.
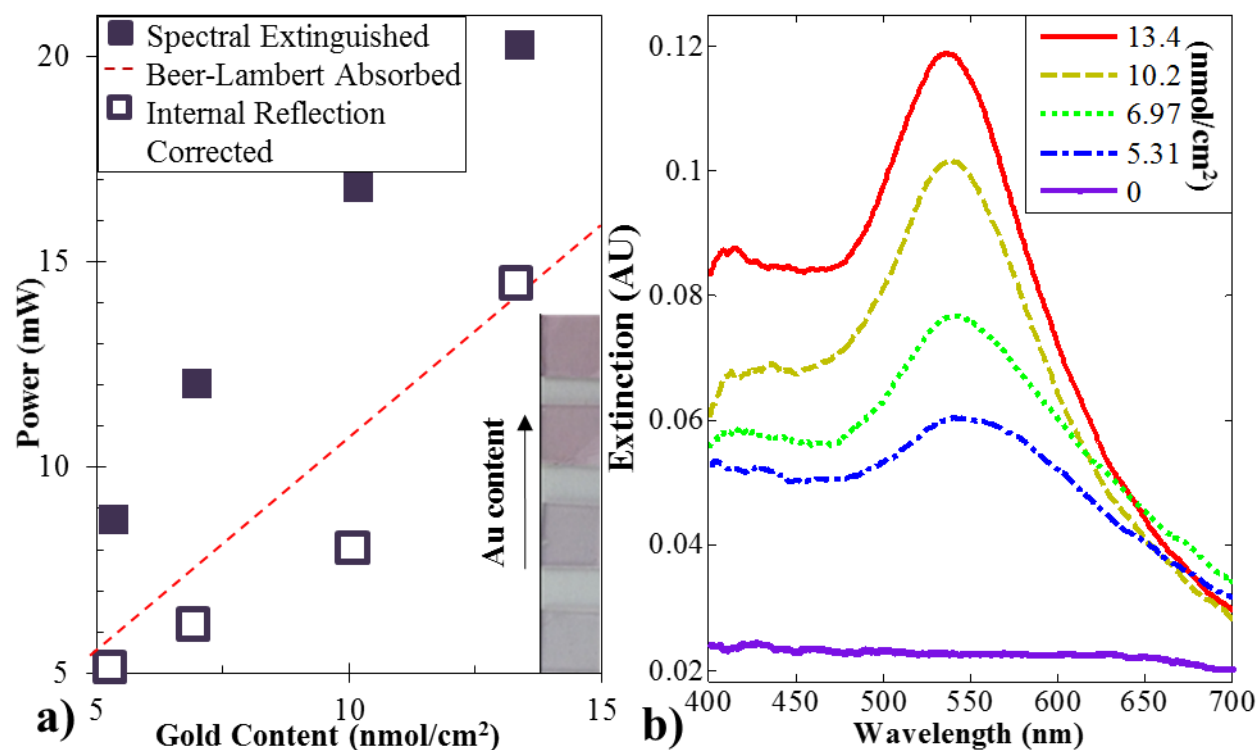
Figure 1: First-generation AuNP-PDMS film: a) total spectral extinguished power (filled), Beer-Lambert estimated absorbed power (dashed line), and extinguished power corrected for internal reflection (hollow), b) measured spectral extinction.

Refractive index (RI) matching experiments were performed to elucidate the source of enhanced spectral extinguished power. According to Snell's Law, light obliquely incident on an interface with a lower RI medium, i.e., PDMS to air, will be directed away from the normal.[38] This characteristic behavior remains valid for media containing nanoscale inclusions.[47] Transparent PDMS scatters little of normal incident irradiation, but dispersion of AuNPs in PDMS could result in obliquely trajected light. Without RI-matching between PDMS and the detector, this light is internally reflected. AuNP absorption, scattering, and diffraction are illustrated schematically in Figure 2a along with internal reflection and/or transmission of light at the PDMS-air interface. This internal reflectance would diminish transmitted power, thereby increasing measured spectral extinction. With an RI-matching fluid, this obliquely re-directed light may instead refract and be recorded as transmitted power since the glycerol-water solution reduces interfacial reflection between PDMS and the adjacent lens that focused light into the detector.
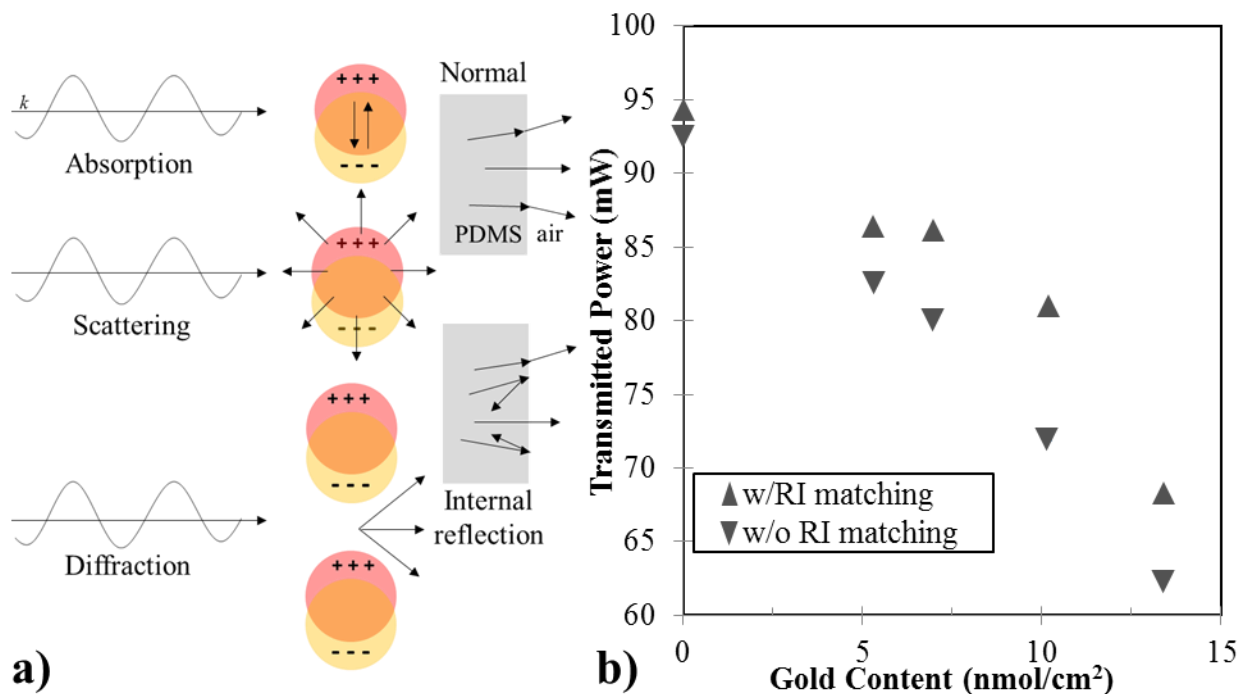
Figure 2: a) Schematic illustrating optical absorption, scattering, diffraction, and internal reflection, b) transmitted power with and without RI-matching fluid at PDMS-air interface.

The difference between transmitted power with and without the RI-matching fluid provides an estimate of the light internally reflected within the AuNP-PDMS. Figure 2b plots transmitted powers in PDMS films containing 0, 5.31, 6.97, 10.2, and 13.4 nmol/cm^2 AuNPs with RI-matching (upward triangles) and without RI-matching (downward triangles) based on 100 mW of incident 532 nm laser excitation. RI-matched transmitted power decreased with increasing AuNP concentration, from 94.3 mW in Au-free PDMS to 68.3 mW at 13.4 nmol/cm^2 AuNPs. Au-free PDMS transmitted only 1.4 mW more power with the RI-matching fluid. Upon inclusion of AuNPs, transmitted power increased by an average of 6.2 mW with the RI-matching fluid. This transmitted power difference increased with AuNP content up to a maximum of 9.1 mW at the second highest AuNP concentration, 10.2 nmol/cm^2. Actual power absorbed by the dispersed AuNPs was estimated by subtracting measured transmitted power with RI-matching from the total incident power (100 mW). The resulting AuNP-PDMS power absorbed corrected for internal reflection is represented in Figure 1a by hollow squares. This corrected maximum power absorbed is less than ideal absorbed power from Mie absorption and Beer-Lambert law for all but the highest AuNP concentration. This suggested AuNP optical absorption is predictable once this additional contribution from diffraction-induced internal reflection is considered.

2.1.2 Optical extinction enhancements as a function of interparticle separation

A subsequent study[30] developed a new generation of AuNP-PDMS films to distinguish relative contributions of optical absorption and internal reflection, arising from diffraction or Mie scattering, to measured optical extinction. Both 16 and 76 nm AuNPs were dispersed in PDMS films and fluid isopropanol (IPA) at identical concentrations ranging from 0.001 to 0.015 mass-percent; this represented a 3-fold increase in obtainable AuNP concentration via an optimized

fabrication protocol outlined in Section 2.4.1. PDMS films containing 16 nm AuNPs with negligible resonant Mie scattering cross-sections and Wigner-Seitz radii (r_{w-s}), an estimate of interparticle separation, of ca. 410-1000 nm were compared to films containing 76 nm AuNPs with large scattering cross-sections at much greater r_{w-s} of ca. 2-4 µm. This comparison allowed differences between diffraction in the former and scattering in the latter to be observed. Methods to differentiate light trapping from diffraction and scattering from simple plasmonic absorption could offer insights for design of flexible photonic devices with optothermal interactions.[42]

Optical extinction per NP was used as the primary metric for comparing measured and predicted optical extinction as a function of AuNP concentration. Measured extinction per NP was calculated as *A/cnl*, where *A* was extinction amplitude in absorbance units (AU), *c* was AuNP concentration in NP/cm^3, *n* was the spectrum-averaged RI of PDMS ($n = 1.42$), and *l* was film thickness (cm). EMT extinction per NP was calculated as *A/cnl* where $A=-log_{10}T$ and *T* is fractional transmission predicted by geometric optics at resonance (542 nm). For comparison with measured results, optical response of NP-containing media may be estimated by multiplying the number of particles by the single particle Mie extinction cross-section.[48] Mie-derived extinction was estimated as *A/cnl* using Beer-Lambert absorbance,[48] $A=c\sigma l(log_{10}e)$, yielding *extinction/NP=$\sigma(log_{10}e)/n$* where σ was the Mie theory extinction cross-section in cm^2 and $log_{10}e$ was a conversion factor between log-bases.

CDA-derived extinction per NP was calculated assuming a square lattice of AuNPs with a lattice spacing given as double the r_{w-s}. The r_{w-s}, based on the mean spherical volume of medium per particle, is used in condensed matter physics to define the density of a system,[49] and has been leveraged previously to estimate distance between NP in 3D dispersions.[50] As an example calculation, Wigner-Seitz radius is defined as $r_{w-s} = r_p(\rho_{Au}/x)^{1/3} = (3V/4\pi N)^{1/3}$, where r_p is the

10

particle radius, ρ_{Au} is the density of gold (19.3 g/cm^3), x is gold mass per cubic centimeter of

PDMS, V is the media volume, and N is the number of particles. For r_p = 8 nm, AuNP concentrated

to 2.34 x 10^{11} NPs/cm^3 (N/V) equivalent to x = 9.7 x 10^{-6} grams Au per cubic cm: 8 nm x (19.3

g/cm^3/9.7 x 10^{-6} g/cm^3)$^{1/3}$ = (3/(4π x 2.34x10^{11} NPs/cm^3))$^{1/3}$ = 1006 nm. Decreasing $r_{w\text{-}s}$ from 1006

nm to 408 nm, is shown on the upper axis in Figure 3b. CDA results yield extinction efficiency,

which was converted to optical extinction cross-section by multiplying it by NP geometric cross-

section, i.e. πr_p^2. Extinction values in Figure 3 were calculated by difference from extinction

measured off-resonance at 800 nm. More detailed explanation of measured spectral

characterization and theoretical descriptions are given in Section 2.4.
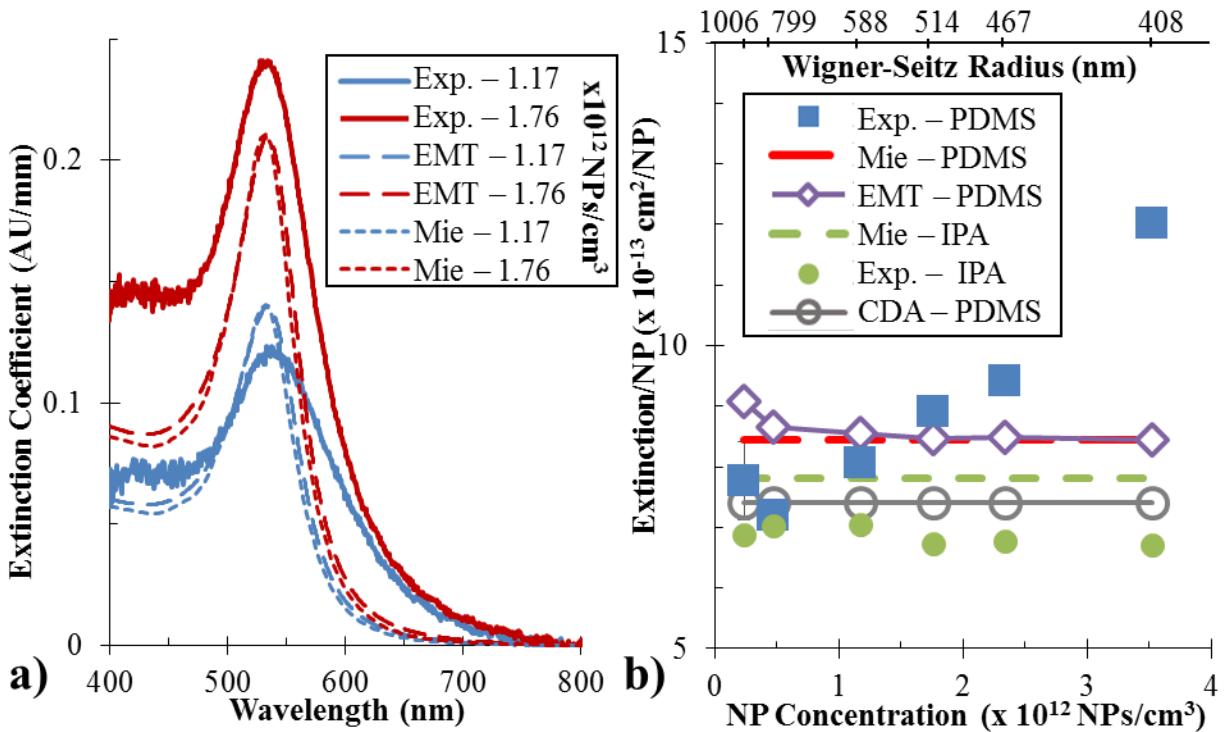
Figure 3: a) Measured and estimated extinction coefficient spectra for 1.17 and 1.76 x10^{12} NP/cm^3 films containing 16 nm AuNPs, b) measured, Mie, EMT, and CDA-derived resonant extinction per NP for each AuNP dispersion, Wigner-Seitz radii shown on upper axis.

Resonant extinction per NP in super-wavelength PDMS films containing 16 nm AuNPs was constant, consistent with theoretical predictions, at interparticle separations greater than the resonant wavelength, $r_{w-s}, > \lambda_{LSPR}$, but increased up to 1.5-fold at $r_{w-s} < \lambda_{LSPR}$. Figure 3a compares measured (solid), EMT (long dash) and Mie (short dash) spectra from 16 nm AuNP-PDMS films at concentrations with r_{w-s} just above (1.17×10^{12} NP/cm^3; 0.005 mass-percent AuNP; blue) and just below (1.76×10^{12} NP/cm^3; 0.0075 mass-percent AuNP; red) $\lambda_{LSPR} \sim 540$ nm. Spectra are represented as extinction coefficient (AU/mm) baseline corrected off-resonance (800 nm). At 1.17×10^{12} NP/cm^3 (blue), the maximum extinction per thickness in PDMS for measured, EMT, and Mie values were 0.121, 0.139, and 0.140, respectively. Above $r_{w-s} \sim \lambda_{LSPR}$ at 1.76×10^{12} NP/cm^3, the maximum measured extinction per thickness was $0.241 - 14\%$ above an estimate of 0.211 obtained from both Mie and EMT. This 2-fold increase in measured extinction per thickness upon a 1.5-fold increase in NP concentration was not explainable by descriptions of increasing complexity: Beer-Lambert law, Mie theory, CDA or EMT.

Measured extinction per NP remained near estimates from Mie, CDA, and EMT in $0.7 - 1.4$ mm thick AuNP-PDMS films at AuNP concentrations for which r_{w-s} was above $\lambda_{LSPR} \sim 540$ nm, but increased at higher concentrations. Figure 3b compares resonant measured extinction per NP for 16 nm AuNP dispersed in PDMS (blue squares) or isopropanol (green circles) with estimates using Mie theory in isopropanol (green dotted line) and PDMS (red dashed line), Maxwell Garnett EMT in PDMS (purple diamonds), and CDA in PDMS (gray hollow circles). Equivalent AuNP inclusion volume fractions used in EMT were 5.02×10^{-7}, 1.00×10^{-6}, 2.51×10^{-6}, 3.77×10^{-6}, 5.02×10^{-6}, and 7.53×10^{-6} at increasing AuNP concentration. Values were plotted as function of AuNP concentration, not area density as in Section 2.1.1, because it more clearly elucidated observed trends.

12

At the lowest AuNP content, 0.234×10^{12} NP/cm^3, measured resonant extinction per NP in PDMS, 7.77×10^{-13} cm^2/NP, was below estimates of 8.43 and 9.09×10^{-13} cm^2/NP from Mie and EMT, respectively. Results were similar at AuNP concentrations of 0.469 and 1.17×10^{12} NP/cm^3, where corresponding r_{w-s} of 1006, 799 and 588 nm remained above measured LSPR wavelengths between 542 and 537 nm. At 1.76×10^{12} NP/cm^3, where r_{w-s} (514 nm) $< \lambda_{LSPR}$, measured extinction per NP surpassed equivalent Mie and EMT estimates (8.91 vs. 8.45×10^{-13} cm^2/NP). As AuNP content increased, measured values diverged further from theoretical estimates, reaching values 1.5-fold above predictions at 3.52×10^{12} NP/cm^3. In contrast, measured extinction per NP for AuNPs suspended in IPA (green circles) was consistent with Mie estimates (green dotted line); it remained relatively flat across this range of AuNP concentrations. Mie estimates in Figure 3b are less for IPA relative to PDMS due to lower medium RI, 1.38 vs. 1.42 in PDMS. It is proposed that Brownian fluctuation of suspended AuNPs in fluid precludes cumulative optical interference.[50]

Increased extinction per NP in PDMS containing minimally scattering 16 nm AuNP at concentrations where $r_{w-s} < \lambda_{LSPR}$, differed from results estimated using Mie, CDA and EMT. This is likely because these descriptions do not account for geometric optical reflection at the PDMS/air interface or for optical interference, i.e. diffraction, of incident radiation accumulated from adjacent resonant plasmonic extinction cross-sections. Mie theory calculates optical absorption and scattering from only isolated particles. Mie theory has been expanded to incorporate particle-to-particle near-field interactions or for NPs dispersed in a highly absorbing dielectric medium, but comparatively low AuNP concentrations dispersed in PDMS herein preclude such effects.[29,51,52] CDA calculates particle polarizability by summing contributions from neighboring particles, but only in a two-dimensional lattice with angularly definable incident irradiation. EMT treatment of optical extinction is independent of separation-dependent interparticle interactions.

13

Multiple scattering extensions for Maxwell Garnett EMT and Mie theory have been developed to characterize optical responses of opaque media.[31] EMT has been expanded to include both effects of multiple scattering and anisotropy.[53,54] However, prediction of bulk geometric optics in these systems remains difficult.[55] Before attribution of increased optical extinction in AuNP-PDMS films, possible effects arising from scattering NPs,[31] particle-particle interactions,[38] or optical interference via dielectric heterogeneity[41] should be considered.

Increased measured extinction does not appear attributable to multiple scattering in super-AuNP-PDMS films for which r_{w-s} is below λ_{LSPR}. Multiple scattering is the phenomenon where photons are re-scattered by neighboring particles, with appreciable scattering cross-sections, numerous times as they propagate through the dielectric medium. Both the original and scattered wave must be considered in multiple scattering descriptions. Optical response of these systems are modeled most simply using diffusion or radiative transport theories, which are accurate at the limit that no light is transmitted ballistically.[32,56] In contrast, the AuNP-PDMS films in this work are largely transparent and contain 16 nm AuNPs with Mie scattering cross-sections only ca. 1% of total extinction. Furthermore, extinction per NP values in Figure 3b consistent with Mie and CDA estimates at $r_{w-s} > \lambda_{LSPR}$ indicate scattering effects are unlikely to play a large role in PDMS films containing 16 nm AuNPs. Control experiments using 76 nm AuNPs, discussed in Section 2.1.3, with large scattering cross-sections verified that divergence of optical rays by multiple scattering increased extinction per NP relative to Mie-calculated values for $r_{w-s} \gg \lambda_{LSPR}$.[30] However, in contrast to dispersions of 16 nm AuNPs in PDMS, extinction per NP in 76 nm AuNP-PDMS was higher than Mie estimates even at low concentrations. Thus, multiple scattering in 16 nm AuNP films for $r_{w-s} < \lambda_{LSPR}$ alone appears unlikely.

AuNP aggregation at elevated AuNP concentrations seems unlikely to result in observable enhancement in extinction per NP. A ca. 10 nm thick coating of polyvinylpyrrolidone (PVP) surrounding each AuNP diminishes the likelihood of aggregation. In fact, sub-wavelength PVP films containing AuNP at 10^3 higher content, discussed further in section 2.2, exhibited no evidence of aggregation upon examination using scanning electron microscopy (SEM). Moreover, random occurrence of aggregation would not be anticipated to produce the observed, reproducible divergence in extinction per NP. The off-resonance (800 nm) spectral baseline adjustment used to calculate measured extinction per NP would likely eliminate effects from non-resonant scattering centers within the AuNP-PDMS matrix. While AuNP aggregation would increase resonant scattering cross-sections, it would increase LSPR bandwidth, diminish LSPR peak intensity, and red-shift LSPR peaks. LSPR peaks in this study actually blue-shifted from 542 to 532 nm with increasing AuNP content. Absence of AuNPs with large scattering cross-sections or indications of anomalous scattering events suggests multiple scattering is unlikely to yield the noteworthy extinction increases observed at $r_{w-s} < \lambda_{LSPR}$ in AuNP-PDMS.

The difference between measured and predicted optical extinction at higher concentrations of AuNP-PDMS films is likely attributable to a geometric optical effect resulting from the dielectric interface between PDMS and air. It is possible that oblique reorientation of incident orthogonal irradiation via diffractive interference from neighboring resonant AuNP optical cross-sections becomes significant at $r_{w-s} < \lambda_{LSPR}$. This results in internal reflection at the air-polymer interface due to Snell's law, as discussed in Section 2.1.1, which remains valid for media containing sub-wavelength inclusions.[38] Investigations studying diffraction in liquids due to an applied electric field help illustrate contributions of diffractive interactions between particles. Enhanced light

trapping could benefit waveguides in organic photovoltaics,[57] absorption and fluorescence in quantum dots,[58] and development of polymeric ultra-high refractive index materials.[59]

2.1.3 Mie scattering enhanced extinction per nanoparticle

Highly scattering 76 nm AuNPs dispersed in PDMS enhanced extinction per NP up to 1.3-fold with increasing AuNP content. These films containing scattering AuNPs provided a positive control for effects of internal reflection on optical extinction at concentrations with r_{w-s} 4-fold larger than the LSPR wavelength. Mie scattering efficiency of 76 nm AuNPs is about 10,000 times greater than in 16 nm AuNPs, accounting for about half of resonant optical extinction. Figure 4 illustrates how resonant extinction per NP for 76 nm AuNPs dispersed in PDMS films (red diamonds) increased with AuNP content in comparison to fluid IPA suspensions (green circles). Resonant extinction per NP improved from 5.73×10^{-11} cm^2/NP at 4.37×10^9 NPs/cm^3 to 6.39×10^{-11} cm^2/NP at the second highest concentration of 21.9×10^9 NPs/cm^3, a 31% increase in extinction per NP. The inset of Figure 4 shows an enhanced dark-field image (scale = 10 µm) of the AuNP-PDMS film containing 21.9×10^9 NP/cm^3. The lower number of 76 nm AuNPs dispersed in PDMS, two orders-of-magnitude less than the 16 nm AuNPs in PDMS, likely precluded diffraction. The upper axis in Figure 4 gives r_{w-s} in these sample ranging from 1938 to 3793 nm. Peak LSPR wavelengths decreased from 569 to 563 nm as AuNP concentration increased.

Adding more scatters into PDMS increased probability incident light was re-directed obliquely thereby enhancing total optical extinction via internal reflection or multiple scattering. Extinction per NP of 76 nm AuNPs in PDMS was 5.73, 6.07, 6.31, 6.39, and 6.02×10^{-11} cm^2/NP as AuNP concentrations increased from 4.37 to 32.8×10^9 NPs/cm^3. A tangent baseline approximation was used for measured resonant extinction amplitudes, a technique commonly applied to spectra with

an unknown or shifting baseline.[60] The line was drawn tangent to the spectral feature on both left

(~450 nm) and right hand (~650 nm) sides of the LSPR (~565 nm), with extracted magnitudes

reported as the difference between LSPR and tangent baseline extinction value at the peak

wavelength. Multiple scattering likely contributes to enhanced optical extinction by providing a

larger effective optical path length. The optimal particle diameter to maximize multi-scattering

extinction was discovered to be smaller than that maximizing single-particle Mie extinction cross-

section.[61] Prior description of Mie scattering revealed that resonant extinction cross-sections are

enhanced when re-radiation prevails over dissipative losses.[62]
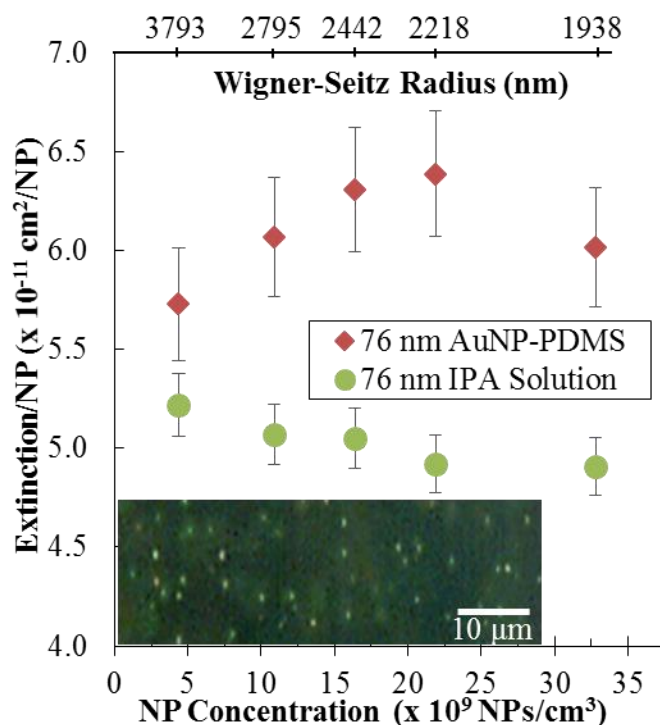
Figure 4: Resonant extinction per NP for 76 nm AuNP dispersions, inset dark-field image of 21.9 x10^9 NP/cm^3 film, Wigner-Seitz radii shown on upper axis.

Suppressed extinction per NP at the highest AuNP concentration could indicate increased

forward scattering at higher particle densities or enhanced broadband scattering. Either of these

phenomena could decrease extinction per NP relative to the tangent baseline approximation used

17

to calculate measured extinction per NP values. Blue-shifting of the LSPR peak from 569 to 562 nm with increasing AuNP concentration does not support likelihood of aggregation. Extinction per NP was not boosted by Mie scattering in fluid IPA dispersions of 76 nm AuNPs. Extinction per NP in IPA was 5.22, 5.07, 5.05, 4.92, and 4.91 x10 x10^{-11} cm^2/NP as AuNP concentration increased. Although strictly valid only for non-scattering media, these results did not deviate appreciably from Beer-Lambert law.[31] Diffusive theory and radiative transport are frequently employed to model highly scattering AuNPs in opaque nanocomposite materials where little or no light is transmitted ballistically.[32,56] The films analyzed in the current work fall between these two idealities, but an approach coupling radiative transport theory with conventional Fresnel optics is a subject of ongoing discussion.[32]

Hyperspectral analysis revealed a resonant scattering peak at about 580 nm for the second highest AuNP concentration, which agrees well with a prediction of 572 nm given by Mie theory. Enhanced dark-field images such as shown in Figure 4 inset further indicate aggregation is likely not prevalent at concentrations below the highest AuNP concentration. This work represents the first instance when individual AuNPs have been imaged *in situ* in PDMS without destructive transmission electron microscopy (TEM).[22] The highly insulating PDMS host does not permit SEM of dispersed AuNPs. The small size and accompanying lack of resonant scattering precluded similar hyperspectral dark-field analysis of 16 nm AuNPs in PDMS. However, any aggregate scattering in the 16 nm AuNP-PDMS films would have likely been visible, further evidence of a lack of AuNP aggregation.

2.2 Characterization of optical extinction in AuNP-PVP thin films

High concentration of AuNPs dispersed in ca. 70 nm thickness polyvinylpyrrolidone (PVP), on the order of 10^{15} NPs/cm^3, provided a scenario in which both film thickness and interparticle separation were extended to $\ll \lambda_{LSPR}$. Resonant extinction per NP in these AuNP-PVP films, the thinnest, most concentrated films analyzed to-date, was observed to trend downward as particle separation decreased, consistent with *a priori* estimates from EMT, Mie theory, and CDA.[63] Figure 5a shows measured UV-vis extinction spectra for the five fabricated AuNP-PVP films. AuNP concentration increased from 1.01 x10^{15} NP/cm^3 (green) to 5.06 x10^{15} NP/cm^3 (blue), while accompanying LSPR extinction magnitudes increased from 0.036 to 0.069 AU across this range. Extinction at 5.06 x10^{15} NP/cm^3, 0.069, is equivalent to approximately 80% transmission. Resonant extinction of 20% is noteworthy for films only ca. 70 nm thick. Figure 5a inset shows an atomic force microscopy (AFM) surface plot scanned over a scratch made in the 5.06 x10^{15} NP/cm^3 sample. Previously, optic extinction of 130 nm thick polymer dispersions, including PVP, containing reduced AuNPs were examined at concentrations also on the order of 10^{15} NP/cm^3, as estimated based on reported LSPR magnitudes.[64]

Measured extinction per NP (blue squares) decreased asymptotically from 1.01 to 5.06 x10^{15} NP/cm^3 as interparticle distance, i.e. double the Wigner-Seitz radius, decreased from 130 to 76 nm, as shown in Figure 5b. Extinction per NP were calculated in the same manner as outlined in section 2.1.2 for 16 nm AuNP-PDMS films. Measured values were ca. 3 to 5 x10^{-13} cm^2/NP below EMT estimates for AuNP-PVP films; however, the decrease in extinction per NP as AuNP concentration increased was similar in both. EMT has been used prior to accurately predict optical properties of composite media at NP fill fractions of more than 0.1,[65] more than 10 times greater than those depicted in Figure 5. Measured extinction per NP values dropped below Mie estimates

(red dashed line) at AuNP concentration greater than 1.69×10^{15} NP/cm³. Both the 10 nm PVP shell surrounding dispersed AuNPs and SEM images precluded aggregation as a likely culprit for the observed decrease in measured extinction per NP; Figure 5b inset shows a SEM image of the 3.37×10^{15} NPs/cm³.
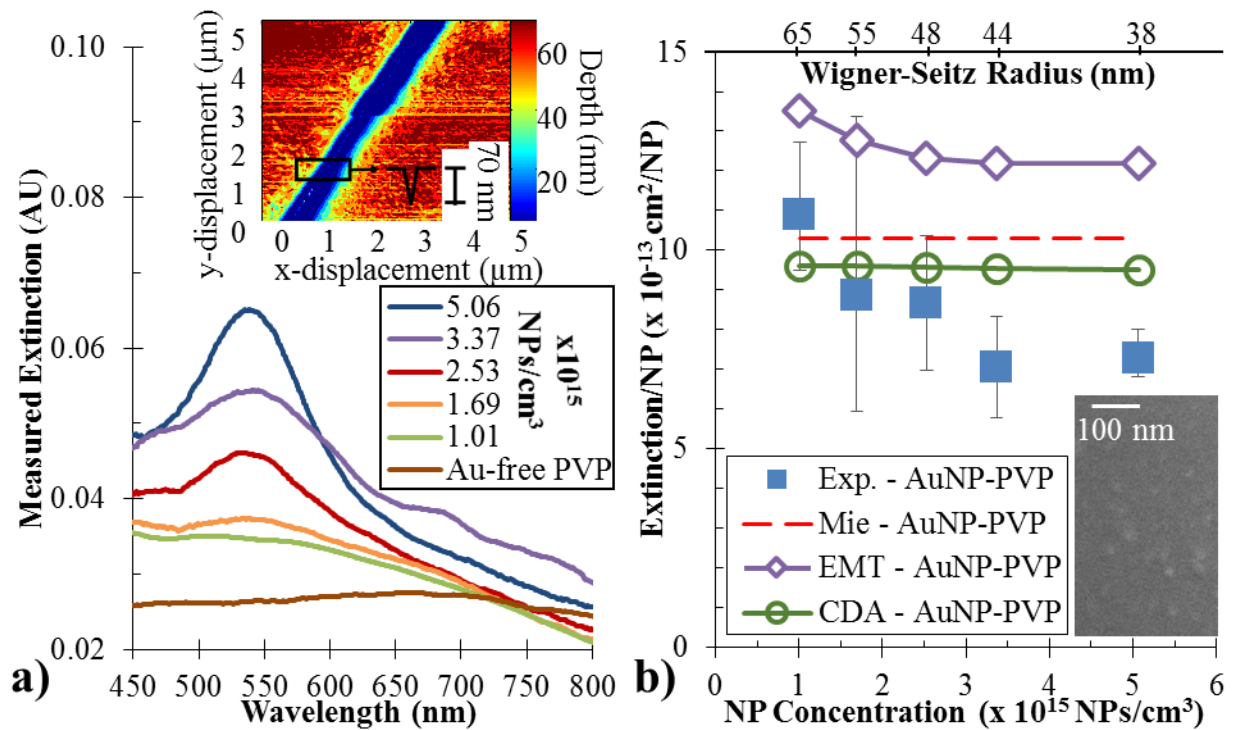
Figure 5: a) AuNP-PVP spectral extinction and AFM surface plot, b) extinction per NP from measurement, Mie theory, EMT and CDA, inset SEM image of AuNP-PVP film.

Comparable to EMT results but with smaller amplitudes, CDA-derived extinction per NP decreased from 9.62 to 9.51 cm²/NP as interparticle separation dropped from 130 to 76 nm. This decrease relative to constant Mie values apparently results from an increase in interparticle coupling that decreases resonant NP polarizability and resulting optical extinction. At lattice spacing equivalent to 2 x r_{w-s}, CDA-derived extinction per NP was suppressed relative to Mie values due to resonant coupling between the LSPR and far-field diffraction from the ordered

particle lattice. The CDA solves Maxwell's equations by treating each nanostructure within the lattice as a single, polarizable dipole.[36,37] Scattering contributions from adjacent nanostructures are incorporated into a retarded dipole sum. Far-field lattice diffraction dominates this retarded dipole sum when interparticle separation is on the order of incident wavelengths.[66] This occurs for ordered dipoles arranged in square, hexagonal, and other configurations.[26,66–68] Treating randomly dispersed AuNPs in PVP films as a two-dimensional ordered assembly in CDA could increase far-field optical extinction effects relative to measured values.

Lower measured extinction per NP values relative to theoretical predictions could be attributable to a lower effective RI of the interrogated medium or film thickness uncertainty. Measured and estimated LSPR energies indicated the effective RI of the AuNP-PVP film on a glass substrate was less than that of pure PVP and/or glass. Relative to λ_{LSPR} estimated by Mie (540 nm) or EMT (542 nm) for AuNPs in PVP ($n = 1.53$), average measured λ_{LSPR} for films deposited on glass was 538 nm. As AuNP content increased from 1.01 to 5.06 x10^{15} NP/cm^3, measured LSPR wavelength increased slightly for the five films: 535 nm, 537 nm, 538 nm, 541 nm, and 538 nm, respectively. Mie-estimated λ_{LSPR} decreased from 540 nm to 525 nm when using an effective RI of 1.3 for a 530 nm thick medium (e.g., one wavelength thick) consisting of 70 nm of PVP, 230 nm of air ($n = 1.00$), and 230 nm of glass ($n = 1.52$). Resonant Mie extinction per NP in this effective dielectric medium decreased from 10.3x10^{-13} cm^2/NP (as shown in Figure 5b) to 5.63x10^{-13} cm^2/NP, just below measured extinction per NP. This comparison shows the sensitivity of extinction estimates on dielectric environment. Alternatively, films thinner than measured (70 nm) would result in larger extinction per NP values, since it is calculated as absorbance divided by concentration, thickness, and RI. AFM measured thicknesses varied from 60 to 80 nm with a mean of 70 nm. Corresponding measurements via surface profilometry, which is less precise at

nanometer scales, were 40-80 nm. Thicknesses estimated from a Beer-Lambert law extinction coefficient derived from 16 nm AuNPs dispersed in fluid IPA were 10-90 nm.

Reversing AuNP-PVP film orientation relative to incident light, i.e., incident on the PVP layer first rather than glass, changed neither λ_{LSPR} nor amplitude. This is unsurprising since RI for PVP and glass are almost identical. Previously, measured λ_{LSPR} of AuNPs deposited on glass red-shifted when light was incident on the glass substrate as opposed to the AuNPs, which were effectively in air due to wavelength contraction.[69] Blue-shifted λ_{LSPR} relative to Mie predictions were observed previously in two-dimensional, square lattices of AuNPs exhibiting lattice resonance coupling between a broad plasmon mode and narrow diffractive mode.[28] Decreasing extinction per NP from EMT is partly the result of optical dispersion in PVP. Extinction in AU of Au-free PVP film decreases from ca. 0.04 at the LSPR (542 nm) to 0.038 at 800 nm. This minute difference increases extinction per NP at lower concentrations when calculated relative to extinction at 800 nm, but its effect diminishes with increasing concentration. Relative to Au-free PVP at the LSPR (542 nm), EMT-derived extinction per NP actually increased slightly because the nanocomposite n increased from 1.52 to 1.55 with increasing AuNP content.

Measured and predicted optical extinction in sub-wavelength AuNP-PVP films exhibited comparable trends and magnitudes despite limitations in the compact theoretical approaches used.[63] Mie extinction was based on a single AuNP cross-section, with cumulative response predicted via Beer-Lambert law, i.e. absorbance increases linearly with concentration. This approximation is valid only for non-scattering and non-interacting NPs.[33,50] Strong deviations are known to occur when interparticle decreases sufficiently to support particle-particle interactions, i.e., for r_{w-s}, ca. 38-65 nm.[51,52] An approach coupling Mie theory and EMT to predict multipole plasmon modes is not needed for dipolar 16 nm AuNPs, but could be useful for samples containing

more complex plasmonic nanostructures.[70] Furthermore, the validity of geometric optics relations for calculation of optical extinction in sub-wavelength films is somewhat limited.[71] However, CDA-estimates of interparticle effects on resonant extinction for random dispersions of AuNPs in polymer films does provide insight. Similarly, finite difference time domain (FDTD) simulations describe dependence of optical extinction on NP size, NP morphology, and incident light direction and polarization.[72] The ca. 70 nm thickness in AuNP-PVP films suggests the dispersed AuNPs approach a nearly two-dimensional distribution. This distribution, along with negligible scattering of the 16 nm AuNPs, prohibited multiple scattering effects on optical extinction, for which the EMT formulation has been extended.[54]

Overall, comparison between measured and estimated extinction per NP values in sub-wavelength AuNP-PVP films suggest minimal light trapping occurs across the high range of AuNP concentrations studied. Measured, EMT, and CDA results showed a decrease in extinction per NP of various magnitudes as AuNP concentration increased. This was in stark contrast to enhanced extinction in super-wavelength AuNP-PDMS films, discussed in Section 2.1, at AuNP concentrations 10^3 lower and accompanying r_{w-s} just below λ_{LSPR}. This divergence in measured optical extinction is likely attributable to geometric optical effects at dielectric interfaces between air, polymer, and glass[71] that disappears at film thickness $< \lambda_{LSPR}$.[38]

2.3 Geometric optics of multi-component AuNP-polymer thin film systems

Algebraic calculation of geometric optics, i.e. transmission and reflection, in AuNP-PDMS films systems provides a compact alternative to computational approaches, EMT, or simple fits to experimental results.[69] Numerical methods may probe optical properties of complex NP configurations, but requires precise characterization of NP arrangement and are difficult to

implement at system boundaries.[73] Effective medium approaches could be useful for asymmetric, polydisperse dispersions of quasistatic reduced AuNPs (rAuNPs), but accurate description of rAuNP fill fraction remains difficult.[74] Purely experimental approaches afford some insights, but extrapolation beyond measured ranges remains difficult.

This section studies geometric optical transmission (T), reflection (R), and resulting attenuation (A), i.e. extinction, in PDMS films containing both asymmetric and uniform distributions of rAuNPs along with uniform distributions of 5 and 20 nm solution-synthesized AuNPs.[75] Optical attenuation (A) is given as one minus the sum of fractional measured transmission and reflection, i.e. $A = 1 - (T + R)$. Attenuation in polydisperse rAuNP-PDMS films increased with order-of-magnitude increases in Au content, while monodisperse AuNP-PDMS attenuation was proportional to Au content. Asymmetric distribution of rAuNPs attenuated light more efficiently than uniform distributions. Linear algebraic estimation of both uniform and polydisperse AuNP-PDMS films with an adjacent back-reflector, along with AuNP-PDMS film pairs, were within 0.04 units of measured attenuation on average. Facile estimation of optical attenuation in multi-component nanocomposites could support light trapping in photovoltaics and membrane separations using AuNP-PDMS and an adjacent mechanical support like the stainless steel mesh used herein.[22,76]

The ternary diagram in Figure 6 shows fractional values of R, T, and A for individual AuNP-PDMS films (solid circles). External reflection was measured by attaching each sample to the exterior of an integrating sphere and irradiating it from the opposite side with the 532 nm laser. Dense distribution of rAuNPs attenuated light most efficiently, scaling AuNP area density, rather than total Au content. For example, the 0.6 mass-percent film (darkest blue; 130 μm thick) has 2.5-fold more Au than the 1.2 mass-percent laminar film (yellow; 25 μm Au-containing layer, 65 μm

24

thick), but almost identical optical attenuation. Attenuation from monodisperse 5 nm AuNP-PDMS films was higher than uniform rAuNP-PDMS films of equivalent thickness, as the 0.1 mass-percent oAuNP film attenuated 0.36 fractional units compared to 0.14 for the analogous rAuNP-PDMS film. Heterogeneity of *in situ* reduced AuNPs results in broadened optical extinction spectra, thereby suppressing attenuation at the single probe wavelength (532 nm).[77]
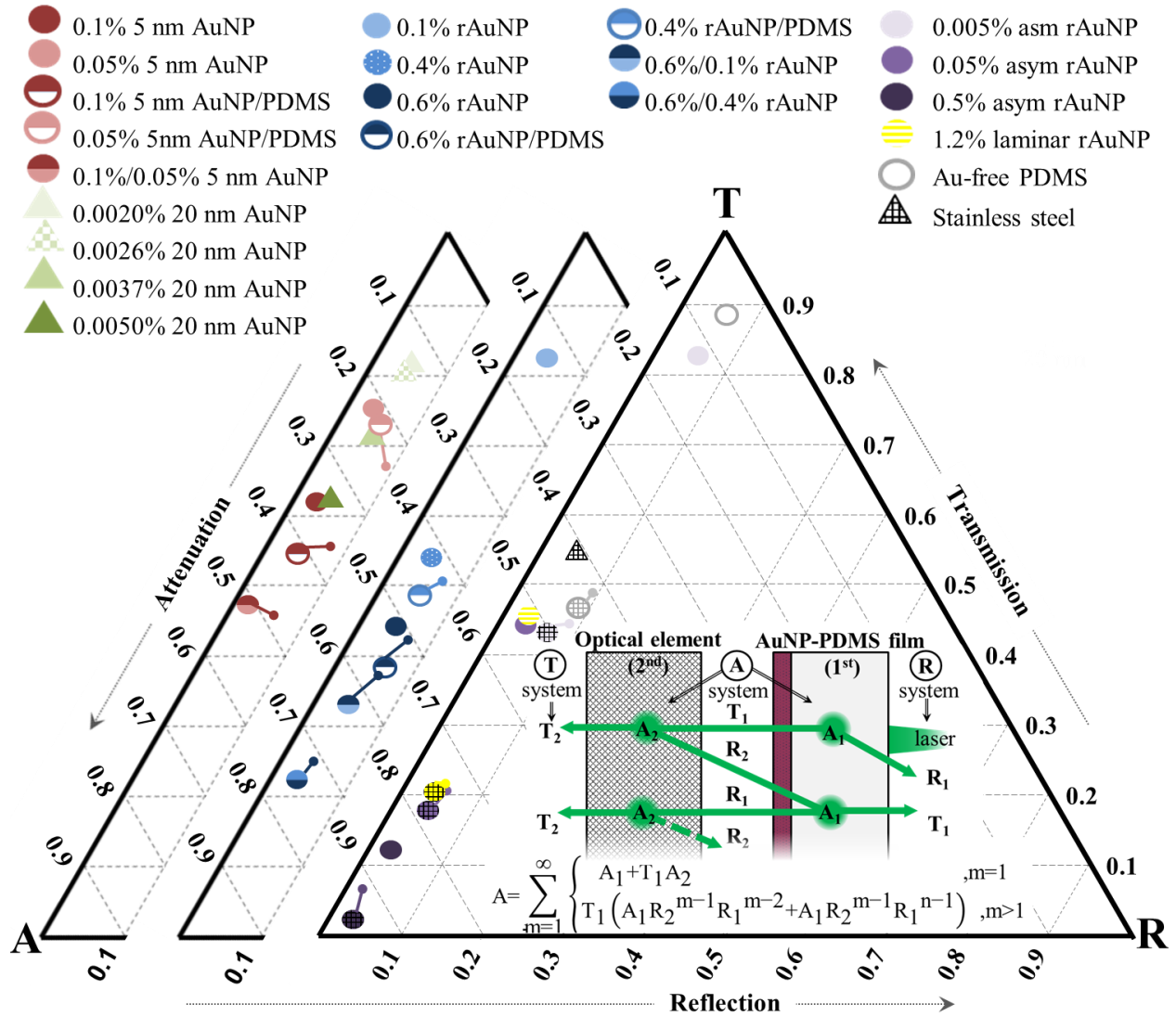
Figure 6: Measured and predicted geometric optical transmission (T), reflection (R), and resulting attenuation (A) for various AuNP-PDMS systems distinguishable by color, shape, and hatching, inset illustrates linear algebraic description of optical attenuation.

First-generation AuNP-PDMS containing 20 nm AuNPs were more efficient light attenuators due to cumulative scattering and/or diffractive effects. Enhanced reflection in these 20 nm AuNP-PDMS compared with 5 nm AuNP-PDMS lacking apparent internal reflection-enhanced optical extinction could result from internal reflection escaping from the opposite film-air interface. It is believed that very small resonant extinction cross-sections of 5 nm AuNPs dispersed in PDMS precluded enhanced optical extinction relative to fluid dispersions that would arise from cumulative scattering and/or diffraction. Uncertainty in AuNP size and distribution in rAuNP-PDMS precluded accurate description of optical attenuation relative to fluid analogues.

Linear superposition of geometric optics, considering multiple light passes, allowed prediction of cumulative transmission and reflection using linearly compounding fractions of each individual component's measured optical response.[75] Inserting a second optical component to each irradiated system induced multiple light passes (m) within the system, thereby enhancing attenuation in two-component systems. Figure 6 inset shows optical attenuation resulting from multiple light passes as a function of constituent optical properties of each component.[69] For example, additional attenuation results from light reflected by the second component, either a stainless steel mesh used for mechanically support of AuNP-PDMS films under vacuum in pervaporation[14] or a second AuNP-PDMS film analogous to multi-layer photovoltaic applications.

The linear algebraic geometric optical description permits calculation of the summative optical responses of an assembly without requiring individual components to be physically distinct. The algebraic sums predicted T, R, and A values of both asymmetric AuNP-PDMS thin film-back reflector pairs and pairs of uniform AuNP and rAuNP-PDMS films.[69] Algebraic estimates (small dots) for each two-component system are connected to corresponding measured values. Estimated and measured attenuation for AuNP-PDMS film-back reflector pairs were within 0.04 absolute

26

units on average. Measured attenuation exceeded predictions for asymmetric film-back reflector pairs, consistent with a previous study of uniform rAuNP dispersions with a range of back-reflector.[69] Superimposable geometric optics of adjacent plasmon resonant and standard optical components was reported for silver NPs deposited on silicon nanopillar arrays.[78]

Measured AuNP-PDMS film pair attenuation was higher than algebraic estimates, suggesting the film-film interface may further enhance light trapping. This is counterintuitive since the film-film interface would be expected to dampen internal reflection as geometric reflection and transmission values for individual films were measured in air. However, agreement between measured and predicted magnitudes are within 0.04 units, indicating this approach remains a valid first approximation of cumulative optical attenuation. Alternatively, attenuation of asymmetric AuNP-containing layers was estimated via re-arrangement of the $m = 1$ term in the linear algebraic sum. Predicted attenuation values were 0.90, 0.53, and 0.089 for the 0.5, 0.05, and 0.005 mass-percent asymmetric films, respectively. Estimated attenuation for the 1.2 mass-percent laminar film was 0.52. Low values of reflection in AuNP-PDMS justified use of the single light pass, as effects from multiple light passes are likely negligible.

2.4 Experimental & theoretical approaches

2.4.1 Uniform AuNP-PDMS film fabrication

Dispersion of readily definable solution-synthesized AuNPs into PDMS supports study of underlying optothermal phenomenon, but careful consideration of solubility parameters and AuNP surface functionalization is critical for maximizing AuNP concentration and minimizing aggregation.[30] First-generation uniform AuNP-PDMS dispersions were fabricated as follows.[29,77]

PDMS (Sylgard® 184 silicone elastomer kit #4019862, Dow Corning, Midland, MI, USA) was prepared with a 10:1 monomer-to-crosslinker ratio, then degassed. AuNPs were suspended in ethanol with a stock solution concentration of 10^{13} NPs/ml. Appropriate volumes of this stock solution were mixed with PDMS, yielding concentrations ranging from 0.0020 to 0.0050 mass-percent. AuNP mass-percent was considered the total AuNP divided by the mass of the entire AuNP-PDMS film. After mixing the AuNP solutions into PDMS, the uncured mixture was placed on a ceramic curing surface. Films were cured for 10 minutes at 150 °C then cut into 5 mm x 5 mm samples.

Second-generation AuNP-PDMS with higher AuNP content and improved dispersion were fabricated as follows.[30] PDMS was prepared with a 10:1 monomer-to-crosslinker ratio, then degassed for two hours. Polyvinylpyrrolidone (PVP)-coated, dried AuNPs (Nanocomposix, San Diego, CA, USA) were dispersed at a concentration of 1 mg/ml AuNPs (5.06 x 10^{15} NPs/cm^3) in isopropanol (IPA). Commercially available AuNPs larger than 5 nm in diameter are usually capped with polar compounds like PVP, which severely inhibits mixing into nonpolar PDMS. IPA was chosen as it balanced AuNP-PVP solubility in the solvent with solvent solubility in PDMS better than water, ethanol, or acetone. Allotted volumes of the 1 mg/ml PVP-coated AuNP solution were then mixed into PDMS. Resulting concentrations in PDMS ranged from 0.001 to 0.015 mass-percent and 0.002 to 0.015 mass-percent for 16 nm AuNPs and 76 nm AuNPs, respectively. These AuNP-PDMS mixtures were degassed again for 24 hours, after which 1.5 g was poured into a 25 mm x 25 mm x 1 mm in polystyrene sample box. The samples boxes were then wrapped in foil to protect from photo-induced effects and cured in an oven for 24 hours at 60 °C. Longer curing times at lower temperatures helped outgas evaporating solvent with minimal formation of observable air bubbles or defects.

2.4.2 Asymmetric AuNP-PDMS film fabrication

This work also developed a method to facilitate rapid reduction of gold(III) chloride (HAuCl$_4$; TCA) into partially-cured PDMS.[22] Diffusion times and pre-curing was optimized over three order-of-magnitude of TCA concentration. PDMS crosslinking is facilitated chemically by reaction between the monomer vinyl groups and silicon hydride groups in the curing agent. Residual silicon hydride is thought responsible for TCA reduction into AuNPs.[79] Utilization of a partial cure prior to TCA introduction left more crosslinker available for Au reduction. A multitude of TCA dilution concentrations, curing conditions, monomer-to-crosslinker ratios, and diffusion times assessed led to less optimal outcomes.[22] Prior work within the group suggested that concentrations beyond 0.75 mass-percent TCA prevented curing of PDMS. In this work, fully crosslinked Au-free PDMS gave physical support to higher concentrations with somewhat tacky surfaces at maximum Au concentration.

TCA obtained from the manufacturer (Sigma Aldrich, St. Louis, MO, USA) was dispersed in distilled, deionized (DD) water at 25 mass-percent TCA, calculated as the mass of pure TCA divided by the mass of the dilution. This aqueous solution was diluted further to reach the TCA concentrations used. Au-free PDMS, with a 10:1 monomer-to-cross-linker ratio, was spincoated on a 1 in x 1 in x 0.04 inch glass substrate at 1000 RPM for 90 seconds. Each film was cured at 24 hours, and weighed approximately 30 mg. This partially-cured PDMS was then exposed to TCA solutions ranging from 0.005 mass-percent (0.00015 M) to 0.5 mass-percent (0.15 M) for 24 hours in a sample box (25 mm x 25 mm x 1 mm) wrapped in parafilm to mitigate evaporation. 2 ml of the dilute TCA solutions were used to ensure the PDMS surface was completely submerged. Following exposure, the film was rinsed, then fully cured on a hot plate for 15 minutes at 180 °C. Au-free PDMS controls were fabricated using distilled, deionized water in lieu of aqueous TCA.

2.4.3 AuNP-PVP thin film fabrication

Isopropanol (IPA) dispersions containing AuNP and polyvinylpyrrolidone (PVP) were spincoated to create sub-wavelength AuNP-PVP thin films on ultra-smooth BK-7 glass.[63] PVP-coated, dried AuNPs (Nanocomposix, San Diego, CA, USA) were dispersed at a concentration of 1 mg/ml AuNPs in IPA; this solution also contained 5.67 mg/ml of PVP. Following solvent evaporation, the ratio of 1 mg AuNPs per 5.67 mg PVP corresponded to the highest AuNP concentration in residual PVP of 5.06×10^{15} NP/cm^3. This stock solution was diluted further with 5.67 mg/ml PVP in IPA matching the molecular weight of the initial PVP (40 kDa). Polished BK-7 glass was pretreated in Piranha solution (3:1 concentrated sulfuric acid to hydrogen peroxide) to facilitate removal of organic impurities and hydroxylate the surface for improved solvent wettability. Approximately 40 µL of each AuNP-PVP solution was dropped on ca. 10 x 10 x 0.5 mm Piranha-treated BK-7 glass pieces and spincoated at 4000 rpm for 30 seconds. These ultra-thin AuNP-PVP films remained on the transparent substrate for all subsequent optical analyses.

2.4.4 Optical and physical characterization

Spectral extinction of both AuNP-PDMS and AuNP-PVP films were measured with an integrated light microscope (Eclipse LV100, Nikon Instruments, Melville, NY, USA) and spectrometer (Shamrock 303, Andor Technology, Belfast, UK). Maximum magnification for the light microscope's objective is 100x. The spectrometer's slit size is 200 µm. Calculated spectral extinguished power for AuNP-PDMS films was given by $I (1-10^{-A})$, where I is the incident laser power, (100 mW) and A is the measured spectral extinction in absorbance units.

Geometric optics (i.e., transmission and reflection) of first-generation AuNP-PDMS films were independently measured at 532 nm using an integrating sphere apparatus described

previously.[69] External reflection could be measured by affixing each sample to the exterior of an integrating sphere (IS200-4, Thorlabs, Newton, NJ, USA) and irradiating it from the opposite side of the sphere with a 532 nm diode laser (MXL-H-532, CNI, Changchun, China). For transmission, the films were next to a lens focusing transmitted light into the detector. A small gap between the sample and lens was occupied by air for normal transmission measurement (without RI-matching) and water-glycerol for RI matching with PDMS (RI = 1.42). Transmission, i.e., forward scattering, was captured using a power meter (PM100D, Thorlabs, Newton, NJ, USA), while a spectrometer (AvaSpec-2048, Avantes, Broomfield, CO, USA) captured external reflection, i.e. backscattering, coupled by the integrating sphere. Internally reflected power is given as the change in transmission in presence and absence of the RI-matching fluid.

Both surface and cross-sectional images of asymmetric AuNP-PDMS were taken using a digital camera (Infinity 1-5, Lumenera Corporation, Ottawa, CN) integrated with the light microscope in bright-field reflection mode. Cross-sectional images were obtained by cutting of small sections of the AuNP-PDMS film, and sandwiching it between a pair of glass slides. Thin film dimensions were characterized using image analysis software (Infinity Analyze, Lumenera Corporation, Ottawa, CN) which was calibrated using TEM grids with known grid spacings.

2.4.5 Maxwell Garnett effective medium theory

Prediction of bulk optical properties of dielectric media containing nanoscale inclusions supports design and implementation of these systems.[69,74,80] Maxwell Garnett EMT is applied broadly to describe optical response of inclusions within a homogeneous dielectric material. EMT's primary output is an effective bulk dielectric function of the composite media.[81] EMT is particularly beneficial for estimation of composite dielectric functions at inclusion fill fractions of

up to 30%, where inclusion fraction is large enough that a Beer-Lambert treatment is insufficient to accurately describe the optical properties of the system.[81,82] By definition, the optical extinction of a distinct unit cell is identical to a material with the effective medium's dielectric permittivity. EMT calculates the electrostatic field induced within the host media by an individual spherical inclusion and approximates its distortion due to interaction between inclusions.[82]

If the scattering amplitude of inclusions in the direction of incident irradiation is zero, use of Fresnel equations (geometric transmission and reflection) to predict optical response is permitted.[82] In this "small sphere" limit, description of inclusions with large scattering amplitudes, e.g., AuNP greater than 50 nm in diameter, and subsequent use of Fresnel relations would be inaccurate.[82] Conversely, the point at which an inclusion-containing medium can no longer be described by its bulk dielectric function (approximately 5 nm for AuNP) sets the lower bound for inclusion size.[83] More rigorous applications of EMT has been developed to characterize multiple scattering events,[54] anisotropic inclusions,[53] and finite-sized conglomerates.[65] EMT has even been used to calculate effective thermal conductivities in composite solids with strong interfacial thermal resistances – a method generalized to any fundamental transport property describable via Laplace's equation.[84]

The following procedure outlines the calculation of geometric optical properties of AuNP-PVP and AuNP-PDMS films using EMT. The Clausius–Mossotti relation correlates the number of inclusions per unit volume, N_j, in material j, each of which have a uniform, electric polarizability α_j, to a complex dielectric function ε_{eff} of an isotropic, microscopic effective medium[85]

$$\frac{\varepsilon_{eff} - 1}{\varepsilon_{eff} + 2} = \frac{4\pi}{3} \sum_j N_j \alpha_j \qquad (2.1)$$

where $\varepsilon_{eff} = \varepsilon_{1,eff} + i\varepsilon_{2,eff}$. The electric polarizability, or tendency of a materials conduction electrons to be perturbed by an external electric field, of a spherical inclusion i of radius r may be defined classically in terms of its material-specific complex dielectric function, ε_i, as[86]

$$\alpha = \left(\frac{\varepsilon_i - 1}{\varepsilon_i + 2} \right) r^3 \tag{2.2}$$

For an individual material comprised of uniform spherical inclusions, substitution of Equation 2.2 into Equation 2.1 and introduction of a spherical inclusion volume fraction, $\delta_i = N_i \frac{4}{3}\pi r^3$, yields

$$\frac{\varepsilon_{eff} - 1}{\varepsilon_{eff} + 2} = \delta_i \left(\frac{\varepsilon_i - 1}{\varepsilon_i + 2} \right) \tag{2.3}$$

Accounting for the complex dielectric constant of the host material, ε_m, reforms Equation 2.3 to[85]

$$\frac{\varepsilon_{eff} - \varepsilon_m}{\varepsilon_{eff} + 2\varepsilon_m} = \delta_i \left(\frac{\varepsilon_i - \varepsilon_m}{\varepsilon_i + 2\varepsilon_m} \right) \tag{2.4}$$

Considering only spherical inclusions in vacuum, $\varepsilon_m = 1$, Equation 4 simplifies to Equation 3. Solving Equation 2.4 for ε_{eff} yields the familiar Maxwell Garnett effective dielectric constant equation[82]

$$\varepsilon_{eff} = \varepsilon_m \left(\frac{2\delta_i(\varepsilon_i - \varepsilon_m) + \varepsilon_i + 2\varepsilon_m}{2\varepsilon_m + \varepsilon_i + \delta_i(\varepsilon_m - \varepsilon_{i)}} \right) \tag{2.5}$$

Taking the real ε_1 and imaginary ε_2 components of Equation 2.5, the real part of the refractive index, n_{eff}, and the absorption coefficient, k_{eff}, may be calculated as[87]

$$n_{eff} = \frac{1}{\sqrt{2}} \left(\varepsilon_{1,eff} + \left(\varepsilon_{1,eff}^2 + \varepsilon_{2,eff}^2 \right)^{1/2} \right)^{1/2} \tag{2.6a}$$

$$k_{eff} = \frac{1}{\sqrt{2}} \left(-\varepsilon_{1,eff} + \left(\varepsilon_{1,eff}^2 + \varepsilon_{2,eff}^2 \right)^{1/2} \right)^{1/2} \tag{2.6b}$$

33

From this complex refractive index (RI), geometric optical transmission, T, and reflection, R, may be calculated for effective mediums of finite thickness, l, on which light of vacuum wavelength λ is incident using Equation 2.6[87]

$$R = \frac{(n_{eff} - 1)^2 + k_{eff}^2}{(n_{eff} + 1)^2 + k_{eff}^2} \qquad (2.7)$$

$$T = \frac{(1 - R)^2 e^{-4\pi k l/\lambda}}{1 - (R^2 e^{-8\pi k l/\lambda})} \qquad (2.8)$$

Via Equation 2.8, optical extinction in absorbance units is calculated as $A = -log_{10}T$. Complex dielectric functions for Au[88] and PVP[89] used in Equation 2.5, were $-4.856+2.123i$ and $2.342+0.007i$ at 542 nm, respectively. PDMS refractive index was given as 1.42.[90]

2.4.6 Mie theory

The Mie solution to Maxwell's equations, often referred to as Mie theory, describes the scattering and absorption of an electromagnetic plane wave by a single spherical sub-wavelength structures.[47] Mie solutions give scattering and absorption cross-sections, efficiencies, and intensity distributions. Variation in particle geometry, composition, and dielectric environment determine resulting optical response. For comparison with measured results, optical response of bulk nanoparticle-containing media may be estimated by multiplying the number of particles by the single particle Mie extinction cross-section.[48] This is approach is useful in systems where Beer-Lambert law is valid, i.e., optical absorbance is linearly proportional to concentration.[33,50] Like Maxwell Garnett EMT, this simplification is inaccurate for systems with highly scattering particles, since measured optical response is dominated by multiple scattering events. Deviations from ideal Beer-Lambert law behavior have been observed when interparticle separation decreased

sufficiently to support particle-to-particle interactions or when particles were dispersed in a highly absorbing, non-transparent media.[52] Extinction per NP for both AuNP-PDMS and AuNP-PVP films were estimated from Mie theory as *AU/cnl* using Beer-Lambert absorbance, *A=cσl(log₁₀e)*,[48] yielding *extinction/NP=σ(log₁₀e)/n* where σ is Mie theory extinction cross-section in cm^2 and *log₁₀e* is a log-base conversion factor. From this calculation it is apparent that Mie-estimated extinction per NP from Mie theory is independent of AuNP concentration.

2.4.7 Coupled Dipole Approximation

The coupled dipole approximation, CDA, is an extension of Mie theory that includes the effect of interaction with adjacent particles on particle polarizability. In the CDA,[22,23] each NP in an array[52,53] is defined as a single point dipole with electric polarization (P) proportional to local electromagnetic field, E_{inc},[6]

$$P = \frac{\alpha E_{inc}}{1 - \alpha S} \qquad (2.9)$$

where α is the frequency-dependent particle polarizability constant and S is the retarded dipole sum that accounts for far- and near-field dipole radiation from adjacent nanostructures encompassing the lattice.[66] Particle polarizabilities are definable using analytic descriptions,[68] but approximations for higher order modes[26] and more complex nanostructures require numerical methods.[6,92] At lattice spacing comparable to excitation wavelength, far-field lattice diffraction dominates S. Optical extinction from orthogonal incidence wavevector, k, arises from the extent polarization of the lattice is out of phase with the incident field (i.e., P/E_o) and is expressed by

$$\sigma_{ext} = 4\pi k \, Im \left(\frac{1}{1/\alpha - S} \right) \qquad (2.10)$$

where σ_{ext} is extinction cross-section and *Im* represents the imaginary component of the quantity. The CDA uses matrix inversion to solve Maxwell's equations at NP in a user-specified array.[66,93] For a given number of dipoles, the polarization vector at each dipole is calculated using superposition, with various angles of incident radiation able to be analyzed.[58] Simulations in this work studied 16 nm diameter spheres in PDMS ($n = 1.42$) or PVP ($n = 1.53$) RIs. A square 150 x 150 NP lattice grid was used (90,601 dipoles) at a lattice constant equal to double the Wigner-Seitz radius, $r_{w-s} = r_p(\rho_{Au}/x)^{1/3} = (3V/4\pi N)^{1/3}$, where r_p is the particle radius, ρ_{Au} is the density of gold (19.3 g/cm^3), x is gold mass per cubic centimeter of PDMS, V is the media volume, and N is the number of particles.

3. THERMAL DISSIPATION IN GOLD NANOPARTICLE-POLYMER FILMS

Thermal dissipation of plasmon energy from gold nanoparticles (AuNPs) dispersed in dense, transparent polymers has extensive value in biotherapeutics,[95,96] photovoltaics,[19,97] optical interconnects,[20,98] sensors,[23,24] and chemical separations.[22] Surface plasmon energy decays into phonons, which results in an intense thermal response dictated by NP composition and morphology, incident intensity, and host media.[99–102] To-date, assessment of interconnected optical and thermal effects in plasmon-active nanocomposites has relied heavily on interpretation of experimental results and continuum analytic description based on direct photon-plasmon-phonon processes. This chapter comprehensively characterizes thermal dissipation following optical absorption in 3D polymer dispersions. Description of interrelated optical absorption and thermal dissipation was extended beyond conventional optical and one-dimensional heat transfer descriptions to include both finite-element analysis (FEA) and the coupled dipole approximation (CDA). Determination of new plasmon decay pathways and heat dissipated per unit optical extinguished power using compact, multi-scale descriptions of these systems can advance understanding and design of flexible plasmon-active devices.

While direct determination of heat dissipated per unit optical extinction is rare, heating by absorptive nanoparticles has been widely studied. Optical and thermal properties of AuNPs dispersed in liquids or deposited on ceramic substrates have been examined under both pulsed and continuous laser irradiation. Dissipated power from isolated AuNPs is modest, but simultaneous AuNP ensemble irradiation generates local temperatures sufficient to reshape NPs[103] or bulk heating effects able to melt (evaporate) surrounding solids (liquids).[104–106] A one-dimensional analytical optoplasmonic heating description was validated for resonantly irradiated AuNPs

suspended in liquid or deposited on ceramic substrates.[50,101,107] Extension of this analytic description accurately defined evaporation from silica cells and capillaries coated with AuNPs filled with air, water, and butanol.[108,109] These compact analytic descriptions are valuable to intuit thermal dissipation and dynamics using geometric and thermodynamic parameters for effectively one-dimensional dissipation.[110] However, numerical methods remain essential for systems with multidimensional optical absorption and subsequent thermal dissipation.

The work developed herein correlates resonant absorption estimates from measurement, single-particle Mie theory, and multi-particle CDA to measured and FEA-estimated heat dissipation in AuNP-polydimethylsiloxane (PDMS) and AuNP-polyvinylpyrrolidone (PVP) films. First-generation AuNP-PDMS films with uniform dispersion of solution-synthesized AuNPs exhibited measured heat dissipation values 1.4-fold higher than theoretical estimates, potentially attributable to observed diffraction and/or scattering-induced internal reflection. Second-generation AuNP-PDMS films exhibited improved overall agreement with theoretical FEA prediction. These results suggested some, but not all of diffractive-enhanced optical extinction was dissipated as heat as interparticle separation dropped below resonant wavelengths. Asymmetric AuNP-PDMS films containing *in situ* reduced AuNPs exhibited impressive thermal response, but uncertainty in AuNP distribution limited utility of theoretical descriptions employed. Finally, thermal dissipation from sub-wavelength AuNP-PVP films followed measured and theoretical trends in optical extinction per NP, but overall magnitudes appeared suppressed based on FEA characterization. Comparison of measured results with the compact FEA description of plasmonic heat dissipation developed herein represents an important advance in the understanding of photon-to-heat conversion in emerging polymer nanocomposite films.

3.1 AuNP-PDMS thermal dissipation

3.1.1 Measured thermal dissipation exceeds estimates due to internal reflection

An initial investigation compared independent spectroscopic and thermal measures of first-generation AuNP-PDMS films with theoretical estimates of plasmonic heating.[29] Equilibrium thermal dissipation from AuNP-PDMS was computed using FEA by incorporating Mie absorption and traditional convective, conduction, and radiative heat transfer relations. As discussed in Section 2.1, measured spectral extinction from AuNP-PDMS films exceeded estimates from plasmonic absorption alone, attributable to diffraction and/or scattering-induced internal reflection. Effects of this internal reflection, quantified using RI-matching to distinguish it from external reflection and Mie absorption, on AuNP-PDMS thermal dissipation is of significant interest for a multitude of applications.

Measured thermal dissipation from first-generation AuNP-PDMS films exceeded computed estimates that neglected thermoplasmonic contributions from internal reflection. Measured power emitted from single AuNP-PDMS film surfaces, estimated from equilibrium infrared camera images, ranged from 0.64 to 1.23 W, or about 40% greater than maximum absorbable power estimated from fluid dispersions for the $5.31–10.2$ nmol/cm^2 Au first-generation films. Figure 7a shows the power radiated and convected for each AuNP-PDMS film based on both measured (red diamonds) and FEA model estimated (blue squares) film temperatures using spectral extinguished power corrected for internal reflection as the FEA heat source. Thermal emission based on measured temperatures from a single surface of the 5.31, 6.97, 10.2, and 13.4 nmol/cm^2 films was calculated as 2.50, 2.83, 4.03, and 4.27 mW, respectively.
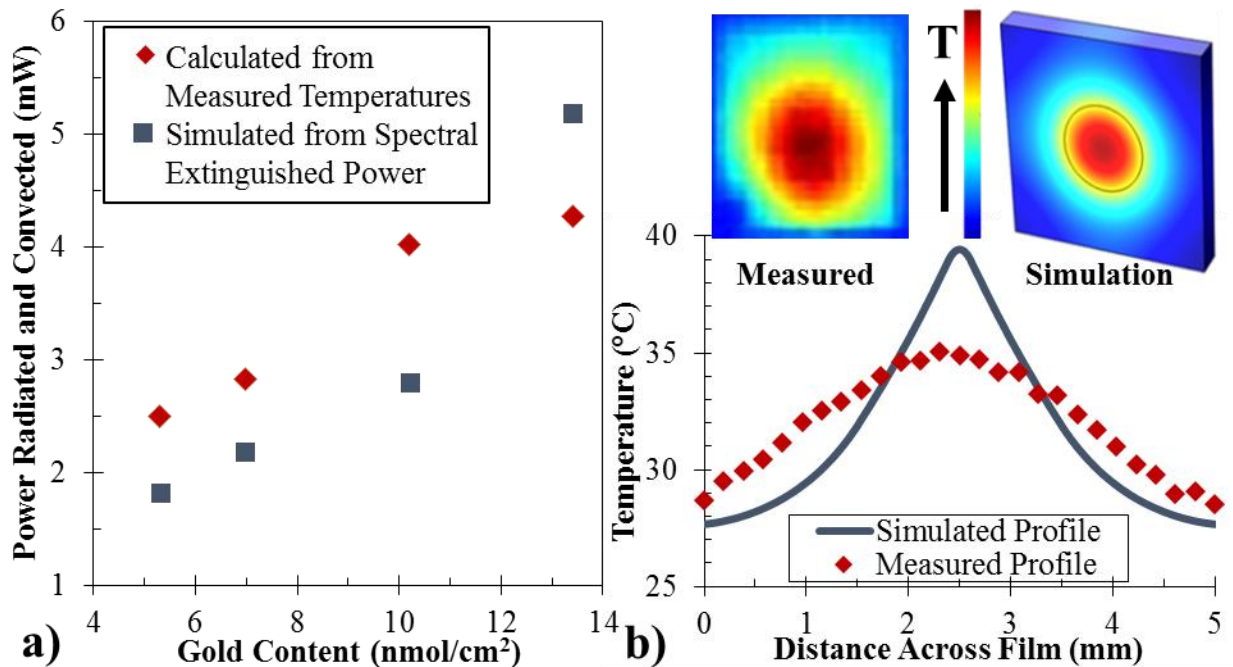
Figure 7: a) Steady-state power radiated and convected and b) radial temperature profiles from first-generation AuNP-PDMS based on measured and FEA simulation results.

Measured estimates of convective and radiated power emitted from the film surface were calculated at each individual pixel's temperature value and summed across the film. Common relationships used to estimate radiation and convection are discussed in more detail in section 3.3.2. Approximately two-thirds of emitted power results from natural convection. For example, the 6.97 nmol/cm^2 AuNP-PDMS film had emitted powers of 1.96 mW from convection versus 0.87 mW due to radiation. Emitted powers based on spectral extinguished power corrected for internal reflection were 1.83, 2.19, 2.80, and 5.18 mW, respectively, for the 5.31, 6.97, 10.2, and 13.4 nmol/cm^2 films. Enhanced measured emitted power could suggest a source of power beyond typical Mie absorption of resonant irradiation, such as diffraction and/or scattering-induced internal reflection not accounted for in the FEA approach. The increase in measured surface power emitted from both faces, estimated by doubling the power from the measured face, for three

40

samples with increasing AuNP content was equivalent to 40%, 20%, and 27%, respectively, of this internally reflected power for the 5.31, 6.97, and 10.2 nmol/cm^2 films.

Enhanced thermoplasmonic dissipation, attributed at least in part to internal reflection, resulted in thermal profiles inconsistent with theoretical prediction. Measured (red diamonds) and simulated (blue line) radial temperature distribution through an axial slice of the 6.97 nmol/cm^2 film are shown in Figure 7b. The incident resonant irradiation source, a 532 nm diode laser, was determined experimentally to have a radially decaying power profile. This profile was approximated in the FEA model by even distribution of absorbable power between a 0.25 mm radius cylinder and seven concentric rings with thicknesses of 0.25 mm radiating outward from the center cylinder. Broadening of this incident profile could result from an outward net radial flux of light obliquely re-directed by the AuNPs and internally reflected at the dielectric interface that improves radial heat dissipation. However, more rigorous characterization of incident beam power distribution and mechanism of thermal imaging is needed to attribute this apparent broadening to any anomalous optical effects.

PDMS thermal conductivity enhancement from dispersed AuNPs is not expected to contribute to this broadened thermal profile. Inserting mass-averaged AuNP-PDMS thermal conductivities into the finite element model, which are considered an upper limit for composite conductivities, did little to broaden simulated profiles relative to measured ones. Mass-averages are considered an upper-limit thermal conductivity estimate as they implicitly assume perfect contact between adjacent dopants throughout the material.[111] In fact, thermal conductivities approaching 0.8 W/mK, 5-fold higher than Au-free PDMS, were needed to match measured profiles. Prior work suggested thermal transport in nanocomposites are consistent with the bulk polymer when conductive inclusions are well dispersed and at relatively low concentrations.[111] Significantly

enhanced thermal conductivity has been demonstrated most often at high fill fractions of long particle chains or nanotubes that allow for unperturbed electron transport through the conducting inclusions.[49] The effects of inclusion concentration, aggregation, and interfacial thermal resistances on colloidal nanofluid and nanocomposite thermal conductivity has been examined.[112]

Edge effects confound precise description of thermoplasmonic effects. The convective heat transfer coefficients used may be inaccurate for prediction of heat transfer from the film's narrow vertical surfaces (~5 mm x ~1 mm) at relatively low Rayleigh (Ra) numbers. This results from unaccounted for inward fluid flow near the plate edge that has been shown to increase heat transfer rates up to double for similar narrow, vertical surfaces.[113] As a result, measured and simulated temperature values diverged at film edges. Ra (~70-200) and plate height-to-width ratio (0.14) herein were not within the validated range of this empirical relation, but do suggest edge effects become increasingly influential with decreasing Ra and plate height-to-width ratio.

Thermal dynamic response of first-generation AuNP-PDMS films was similarly enhanced relative to a simple analytic description developed within the group.[110] Thermal dissipation dynamics in plasmonic materials may be described using a simple analytic heuristic combining micro-scale internal and macro-scale external dissipation rates. This approach accurately characterized dynamic thermal response and overall dissipations rates of conductive and insulating materials resonantly heated by plasmonic AuNPs. Dynamic thermal response is calculable using independent thermodynamic and geometric metrics for particular material systems. External dissipation varies with sample composition and geometry as well as environment. Internal dissipation is determined by material composition and geometry. Overall correspondence between *a priori* estimates and measured total dissipation was good across a broad ranges of sample dimensions, morphologies, and thermal diffusivities. However, measured values for total

dissipation rate for first-generation AuNP-PDMS were, on average, 19% larger than estimates. The difference in measured dissipation rate relative to estimated rate was comparable in magnitude with corresponding differences in measured surface power emission relative to estimated emission as discussed earlier in this section.[50]

3.1.2 Heat dissipation as interparticle separation approaches resonant wavelength

Thermoplasmonic dissipation in second-generation AuNP-PDMS films was also assessed using the FEA approach that analyzed relations for plasmonic Mie absorption, heat conduction, natural convection, and radiation.[114] Agreement of thermal dissipation estimates with measured thermal profiles was improved by introducing an initial Gaussian spatial power density for the volumetric heat source approximating plasmonic heating. This heat source power and Gaussian profile, mimicking resonant absorbed power, was varied until resulting steady-state temperatures inside the laser spot matched minimum and maximum measured temperatures within 0.1 °C inside the 1.5 mm diameter laser spot. The matching heat source power required for each AuNP concentration ranged from 0.9 to 11.5 mW as shown on the x-axis of Figure 8. Measured and CDA-predicted optically extinguished powers (E, y-axis) were calculated as $E = I(1-10^{-A})$ where A is spectral extinction at 532 nm in absorbance units and I was incident power of 532 nm irradiation (19-24 mW) for each AuNP-PDMS film. Resonant spectral extinction was estimated from the CDA extinction efficiency using Beer-Lambert law[48] as reported in section 2.1.2.

FEA-fitted heat dissipated power matching measured thermal response corresponded well with CDA-predicted optically extinguished power for second-generation AuNP-PDMS films. Figure 8 plots optically extinguished power (y-axis) vs. FEA-derived thermal power dissipated (x-axis) based on both *a priori* CDA predictions (hollow green triangles) and measured optically

extinguished power (filled blue circles). The dashed red line designates one-to-one correspondence between both axes. Agreement between CDA- and FEA-derived powers at Wigner-Seitz radius is less than resonant wavelength ($r_{w-s} > \lambda_{LSPR}$), i.e., $\leq 1.17 \times 10^{12}$ NP/cm^3, was consistent with ~98% agreement between CDA and measured optical extinction per NP in Figure 3b. Single-particle Mie theory results were excluded from Figure 8 since consideration of particle-particle interactions via CDA improved agreement with measured optical responses as discussed in Section 2.1.2.
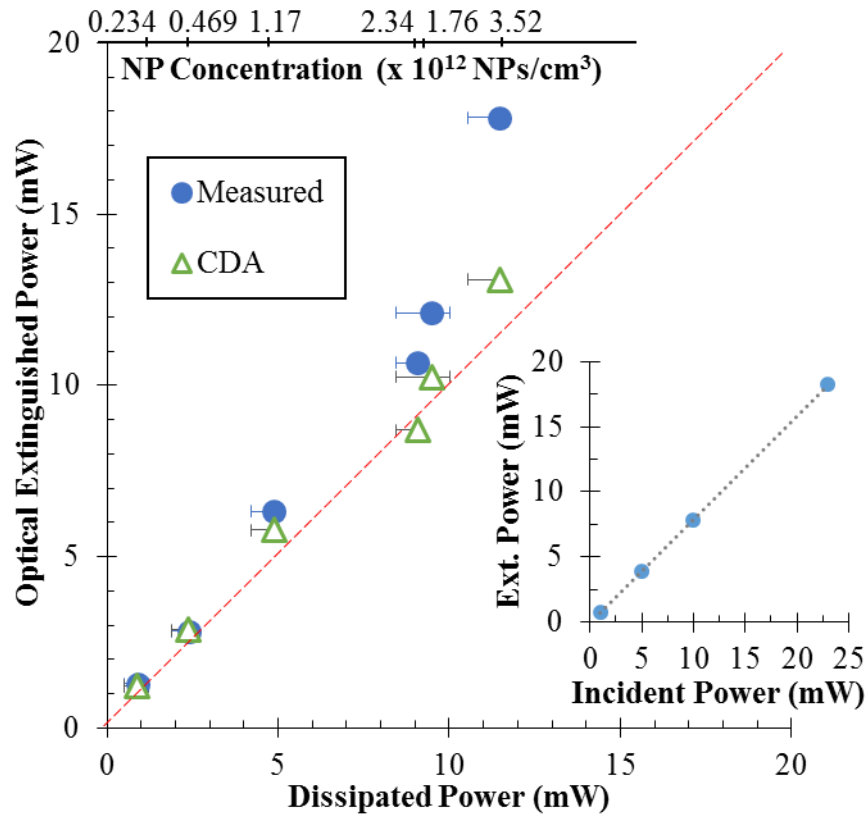
Figure 8: Measured and CDA optical extinguished powers and FEA-fitted thermal dissipated power from second-generation AuNP-PDMS, inset plots extinguished versus incident power.

For AuNP-PDMS films for which $r_{w-s} < \lambda_{LSPR}$, FEA-derived heat dissipated power trails measured optical extinguished power. In other words, thermal dissipated powers do not increase monotonically with enhanced measured optical extinction at these particle separations.

44

Meanwhile, optically extinguished power increased linearly with increasing incident power up to 25 mW for the 3.52 x10^{12} NPs/cm^3 AuNP-PDMS film, as shown in the Figure 8 inset. This suggested that temperature-dependent effects on the AuNPs or host PDMS do not alter measured optical extinction relative to values obtained spectroscopically at low powers across the range of power and resulting temperatures examined. It was important to exclude these possible temperature-dependent effects on observed trends.

The ratio of FEA-fitted heat dissipated power to CDA-predicted optically extinguished power appears enhanced as r_{w-s} drops below λ_{LSPR}. Figure 9 illustrates FEA-fitted heat dissipated per unit CDA extinguished power for each AuNP-PDMS film. This ratio is given as the x-axis divided by the y-axis for the CDA-derived data (hollow green triangles). This ratio increased from 0.71 at 0.234 x10^{12} NPs/cm^3 to 1.05 at 2.34 x10^{12} NPs/cm^3, as r_{w-s} (upper axis Figure 8) dropped from 799 to 467 nm. This apparent increase represents a 1.5-fold improvement in heat dissipated per unit CDA extinguished power as r_{w-s} approached resonant wavelengths. Heat dissipated per unit Mie extinguished power for all but the lowest AuNP concentration surpassed reported photothermal efficiencies of 0.73-0.78 for aqueous dispersion of ca. 15-20 nm AuNPs irradiated at 532 nm.[115] Increased heat dissipated per unit CDA extinguished power suggests an additional mechanism of plasmonic absorption-induced heat dissipation not accounted for in the CDA.

Diffraction-enhanced optical extinction could account for enhanced heat dissipated per unit CDA-predicted extinguished power as r_{w-s} approaches λ_{LSPR} in AuNP-PDMS. The 1.5-fold improvement in heat dissipated per unit Mie extinguished power suggests that some portion of internally reflected light is transduced into heat in diffractive AuNP-PDMS films. This likely occurs since internally reflected has a high probability of being subsequently absorbed by AuNPs. If this were not the case, then the ratio of heat dissipated to Mie extinguished power would be

constant since neither value is affected by this diffractive-enhanced extinction. However, FEA-derived heat dissipated powers lagging measured optical extinguished power, as shown in Figure 8, indicate that a significant portion of this diffraction-enhanced optically extinguished power is not dissipated thermally.
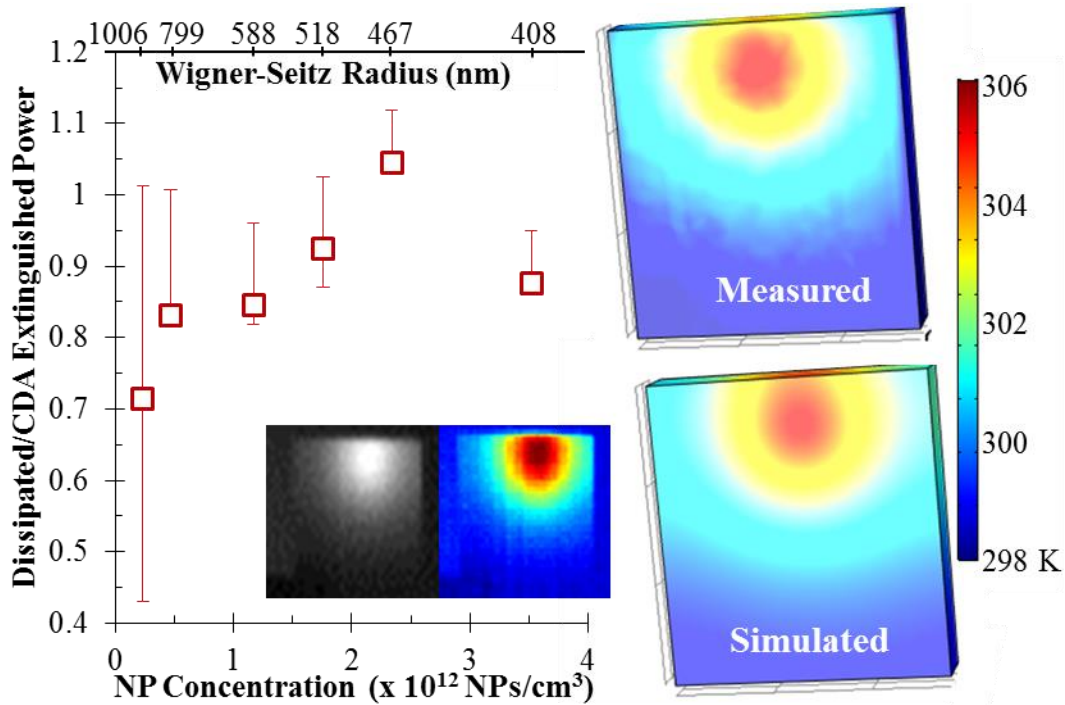
Figure 9: Ratio of FEA-fitted thermal dissipated to CDA optical extinguished power, inset shows raw images and agreement between measured and simulated temperature profiles.

Accurate characterization of heat dissipation relative to optically extinguished power at $r_{w-s} < \lambda_{LSPR}$ was obscured by several effects. Samples in which incident irradiation was closer to the edge could have been subject to geometric optical reflection and refraction not accounted for in the FEA approach. These edge effects on geometric optics near film edges may have contributed to less power absorbed than accounted for in measured extinction. The heat transfer coefficients employed under predicted heat transfer from the film's narrow vertical surfaces as discussed in

46

section 3.1, resulting in divergence between modeled and measured temperature values near film edges. Furthermore, decreased heat dissipated per unit CDA extinguished power at the highest AuNP concentration, 3.52×10^{12} NPs/cm^3, may have resulted from aggregation. The fabrication protocol discussed in Section 2.4.1 optimized choice of polar AuNP capping agent and solvent to ease mixing into non-polar PDMS at AuNP concentrations higher than ever.[30] However, it is possible aggregation had begun to affect power dissipation at this upper limit. AuNP aggregation would dampen absorption and broaden spectral extinction from increased scattering. This would be expected to decrease absorbed power and thermal dissipation relative to Mie-predicted values, but could increase overall extinction magnitude from multiple scattering.[30]

Derived estimates of FEA-fitted heat dissipated power, shown in Figure 8 and 9, were also sensitive to selection of ambient temperature. Ambient temperatures used for derived FEA-fitted dissipated powers were calculated from a ten point average of edge film temperature recorded during the final 10 seconds of the three minute cooling period following laser shutoff. These values are believed to best represent the ambient environment during steady-state heating based on both prior experience and agreement between measured and simulated edge temperatures. Figure 9 inset shows a raw thermal image, a processed image, and a comparison between measured and simulated thermal profile for the 1.17×10^{12} NPs/cm^3 film. Error bars in Figure 8 and 9 result from values derived using upper and lower limit ambient temperature values. These alternative ambient temperatures were acquired at 98% of the final steady-state ambient temperature during cooling and a 10 point average of edge film temperature preceding the heating period, respectively. Heat dissipated per unit of extinguished power decreases as ambient temperature rises since less heat source power in the FEA model is required to obtain equivalent thermal profiles. Variance based on ambient temperature is considerably larger at lower concentrations due to the much lower

47

change in overall temperature. For example, the FEA fitted heat dissipation value dropped by more than a factor of 2 for the 0.234 x10^{12} NPs/cm^3 film when the ambient temperature increased from 296.7 to 298.0 K. Alternatively, the FEA fitted heat dissipation value decreased by less than 10% for the highest concentration AuNP-PDMS film, 3.52 x10^{12} NPs/cm^3, when ambient temperature increased to 298.1 from 297.4 K.

Measured thermal profiles were not broadened relative to FEA estimates for AuNP-PDMS films for which $r_{w-s} < \lambda_{LSPR}$. In other words, the Gaussian distribution of incident power used fit measured profiles well regardless of AuNP concentration. The Gaussian distribution used was broader than the experimentally determined profile used for results on first-generation AuNP-PDMS. Therefore, it is possible the Gaussian profile accounted for apparent broadening observed in Section 3.1.1. Any thermal profile broadening would have been expected only for AuNP-PDMS for which $r_{w-s} < \lambda_{LSPR}$. New data for both sample sets using a consistent experimental setup with a centered laser beam and rigorous beam profiling of the incident laser power distribution could address these uncertainties, but is beyond the scope of this work.

Varying the FEA heat source radial profile used to approximate plasmonic absorption had negligible effect on fitted heat source powers, but resulted in thermal profiles inconsistent with measured results. Heat dissipated powers within 10% of results from the appropriate Gaussian profile were obtained when using uniform, radial distributions of 0.5 and 1.5 mm. For these results, heat dissipated powers were estimated by obtaining an average temperature within the laser spot size in the FEA model that matched measured results within 0.1°C. This average was necessary since the narrow 0.5 mm radius source resulted in over-predicted maximum temperatures at the spot center and under predicted minimum temperature at the periphery. Alternatively, uniform distribution of power over the full 1.5 mm radius heat sources gave broadened temperature profile

with minimum and maximum above and below the measured temperatures, respectively. These results provide insight into the sensitivity of dissipated power to radial incident power distributions; however, they were not used in error analysis since they represent conceptual bounds, rather than actual experimental conditions.

Subsequent work studied geometry- and composition-dependent thermal dynamics of resonantly irradiated second-generation AuNP-PDMS films. Measured dynamics were compared with estimates from the analytic heuristic described in Section 3.1. Measured time-dependent temperature profiles were parsed to calculate local values of the total thermal dissipation pixel-by-pixel using the method introduced previously.[110] Generated temperature maps from both measured and FEA results revealed spatially-dependent thermal dynamics during both heating and cooling. Estimated and measured thermal dissipation rates were within 34% across a broad range of AuNP concentrations, sample thicknesses from 0.7 to 1.5 mm, and surface areas from 28 to 35 mm^2. Dynamic thermal responses were up to 2.5- and 21-fold greater than first-generation AuNP-PDMS and AuNP-silica composites, respectively.

3.1.3 Asymmetric membrane thermal dissipation

Novel asymmetric AuNP-PDMS films developed that contain high concentration of reduced (r)AuNPs at a single interface exhibited a higher temperature change per incident watt (°C/W) than all other nanocomposite media tested previously within the group.[22] Thermal response in the asymmetric, diffusion-reduced 0.05 mass-percent AuNP-PDMS film, 3000 °C/W, was 3-fold higher than prior samples where AuNPs were distributed uniformly, 11-fold higher than AuNPs thermally annealed on glass, and 230-fold higher than aqueous AuNP dispersions. Figure 10 shows measured average temperature within the laser spot increased in linear proportion to optical

49

attenuation both with and without an adjacent stainless steel support mesh used in the plasmonic pervaporation system. Optical attenuation is equivalent to one minus the sum of measured external reflection and transmission. Figure 10 inset shows film surface, film cross-section, and transmission electron microscopy (TEM) image of *in situ* rAuNPs in the 0.5 mass-percent asymmetric rAuNP-PDMS film, allowing rare visualization of reduced AuNP morphology and the asymmetric Au-containing layer.
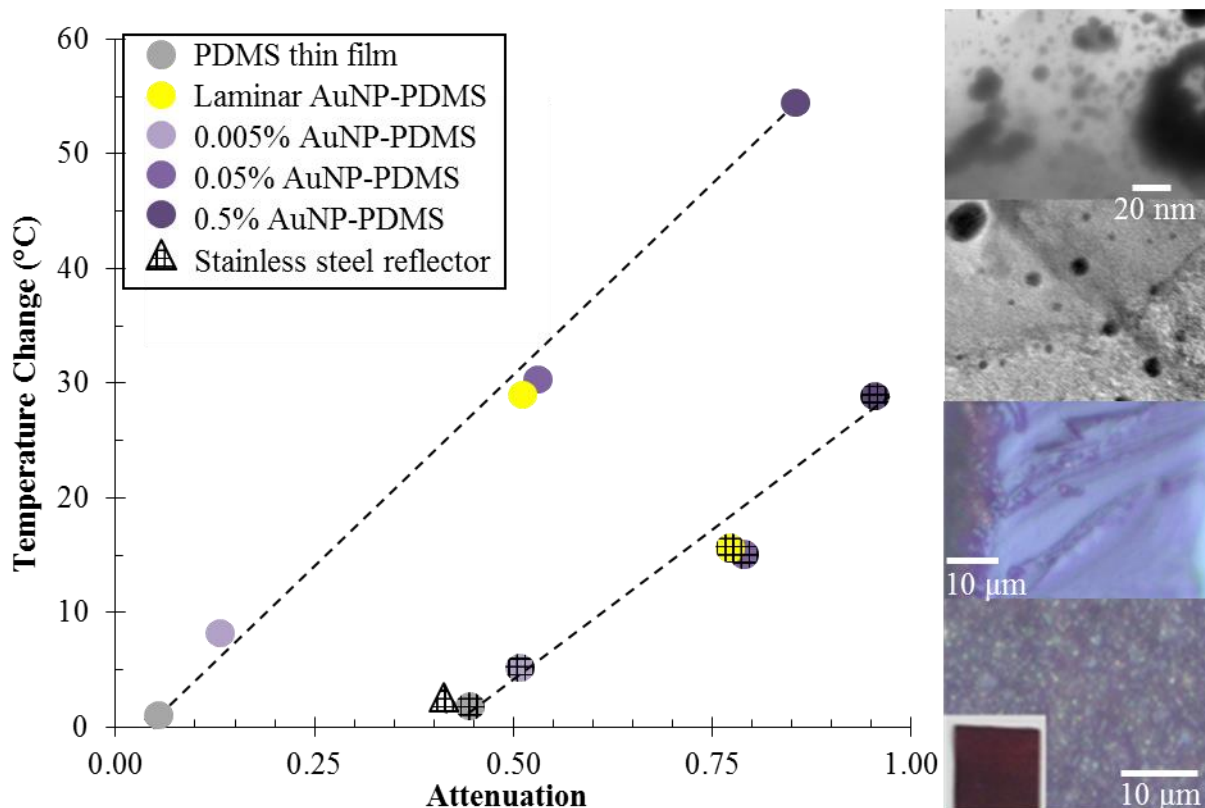
Figure 10: Temperature change versus optical attenuation for asymmetric AuNP-PDMS with and without a stainless steel back-reflector, inset microscopy film images.

The 0.5 mass-percent rAuNP-PDMS film reached 54.5°C above ambient (23 °C), while the 0.05 mass-percent, 0.005 mass-percent, and rAu-free PDMS films achieved 29.9 °C, 8.2 °C, and 0.7 °C above ambient conditions, respectively. Parallel increases in attenuation and temperature

increase suggest photon-to-heat conversion remained constant in asymmetric rAuNP-PDMS films as Au content increased. Enhanced thermal response relative to prior aqueous, silica, and PDMS samples likely results from increased NP density, insulation of the heated layer by adjacent PDMS, and reduced radiative heat transfer relative to planar samples. Preliminary results from the finite element model suggest thickness reduction and adjacent insulating Au-free PDMS contribute to performance enhancements over uniform dispersions.[77]

Addition of a stainless steel support mesh, used in the novel lab-scale pervaporation system, reduced overall temperature increase in asymmetric rAuNP-PDMS by about half. Figure 10 shows each film at increasing Au content reached values of 28.9°C, 14.9°C and 5.0 °C above ambient, on average, within the laser spot. Irradiation of the support mesh alone and coupled with Au-free PDMS resulted in temperature increases of 2.1 and 1.9 °C, respectively. It appears that the support mesh acts as a heat sink, conducting heat from the AuNP-PDMS and transferring it to the surrounding environment. Subsequent designs for the improved plasmonic pervaporation utilized transparent ethylene tetrafluoroethylene (ETFE, Ted Pella, Inc., Redding, CA, USA) mesh to minimize this effect.

3.2 AuNP-PVP thermal dissipation

Thermal dissipation of plasmonic absorption in ultra-thin AuNP-PVP films was studied by comparing measured thermal response with measured and theoretical estimates of optical extinction using the developed FEA model. Measured temperature increase per NP decreased with concentration, matching trends in measured, Maxwell Garnett, and CDA-derived optical extinction per NP results as shown in Figure 11a. Temperature change per NP was calculated as $\Delta T/NmC_p$ where ΔT is the change in temperature within the laser spot diameter (~1 mm) for each

AuNP-PVP film subtracted by Au-free PVP $\mathit{\Delta T}$, N is the number of NPs irradiated NPs and mC_p is the thermal mass of each sample. The number of irradiated NPs was determined by multiplying the cylindrical volume of the 70 nm thick PVP film irradiated by the 1 mm diameter beam by NP concentration in NPs/cm^3. Change in temperature per NP was divided by thermal mass, mCp, to correct for mass variations between samples. Resulting temperature per NP values decreased from 4.29 x 10^{-7} °C per NP at 1.01 x 10^{15} NP/cm^3 to 3.37 x 10^{-7} °C per NP at 3.37 x 10^{15} NP/cm^3. This influences design of photothermal devices: a sublinear increase in heat relative AuNP concentration provides a decreasing return.

Temperature increase per incident resonant power corrected for sample mass in grams (°Cg/W), including the glass substrate, from resonant absorption in sub-wavelength AuNP-PVP was comparable to prior work. The maximum °Cg/W observed in this work, 3.2 for the 5.06 x 10^{15} NP/cm^3 AuNP-PVP film, was comparable to values of ca. 3 for both AuNPs annealed on glass and fluid-filled capillaries.[101,108,109] This °Cg/W was greater than an AuNP colloid solution,[50,101] but less than AuNP-PDMS films described in Section 3.1 that exhibited a °Cg/W of up to 19.[114] It should be noted that this comparison does not take into account respective thermal masses or thermal dynamics of these samples. Layer-by-layer fabrication with control of spatial dimension and concentration could be implemented to enhance overall thermal response of PVP thin films containing Au nanostructures.[99,116]

Despite sub-wavelength optical confinement and high concentration dispersed AuNPs, overall measured thermal characteristics conformed to linear microscopic description. Magnitude of temperature increase in AuNP-PVP films irradiated at 532 nm laser scaled with AuNP concentration in general. Dynamic thermal response followed typical heating and cooling curves. Temperature increased logarithmically during laser excitation, approaching steady-state at the end

of the 90 second heating period. The subsequent cooling curve when irradiation ceases exhibited

an expected exponential decay. These curves were used to estimate heating time constants, an

important metric for characterizing dynamic thermal response as well as photon-to-heat

conversion.[50] Absolute change in temperature dropped in two samples relative to films with lower

AuNP content, attributable to laser-induced damage. Visible in SEM images, shown in Figure 11,

are ca. 100 nm craters within the laser-irradiated area of the 3.37×10^{15} NP/cm^3 film that are absent

outside the laser-irradiated area; these films were thus excluded from subsequent analysis.
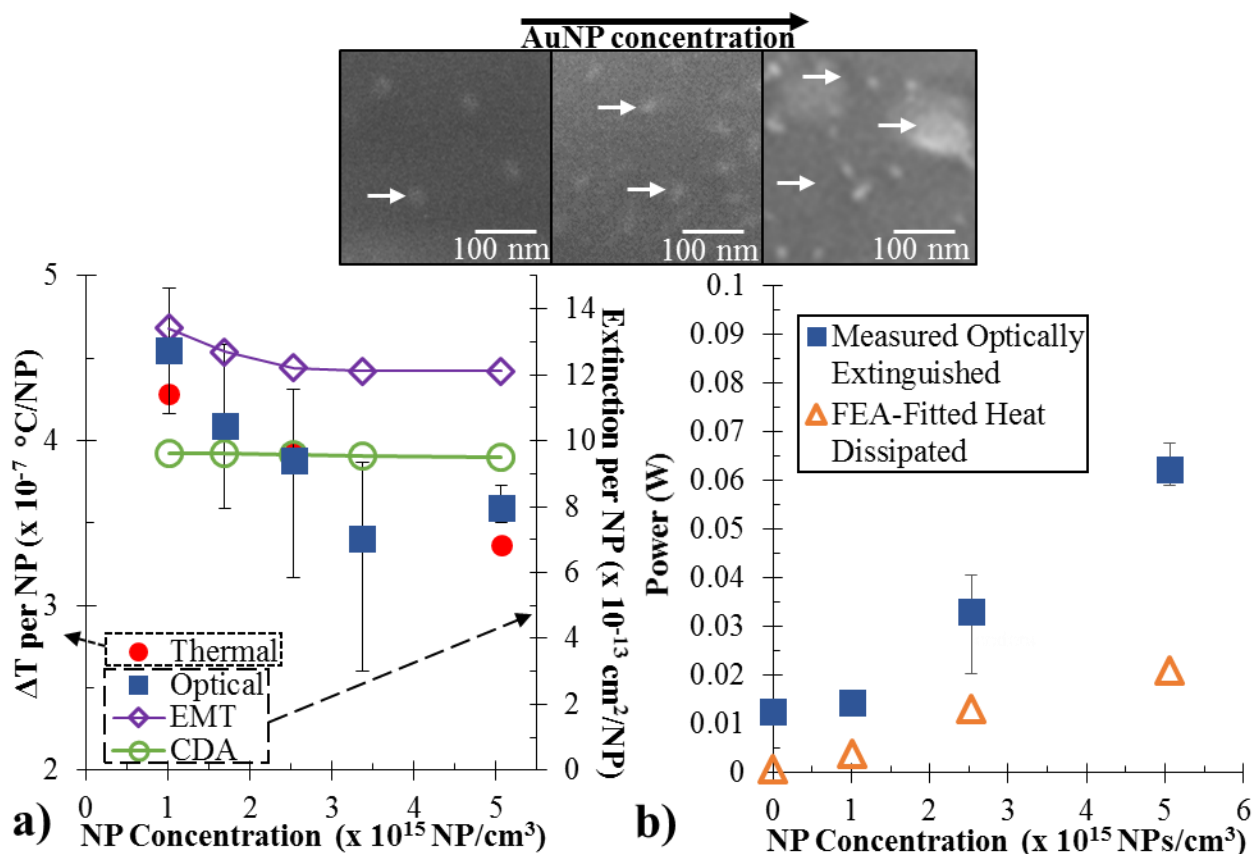
Figure 11: a) Temperature change and optical extinction per NP, b) optical extinguished power, FEA-fitted heat dissipated power, and inset SEM images for sub-wavelength AuNP-PVP films.

Macroscopic measures of overall heat transfer and temperature profiles in concentrated, sub-

wavelength PVP films trended with microscopic description of heat transfer quantified using FEA

53

characterization. Measured power, heat flux, temperature distribution and dynamics in sub-wavelength AuNP-PVP films demonstrated broad agreement with numeric FEA results using rigorous expressions for convection, conduction, and radiation. This method allowed estimation of both (i) expected thermal profiles in AuNP-PVP films based on measured optically extinguished power and (ii) actual absorbed power needed to match measured thermal profiles. As shown in Figure 11b, FEA-derived heat dissipated powers (blue) were ca. 3-fold less than measured extinguished power values (green) for each AuNP-PVP film, suggesting a significant portion of optical attenuation is not readily transduced into heat.

Fitting of the FEA description to heuristically represent experimental temperature profiles was performed by matching the average temperature of the 1.2 mm region of interest (ROI) centered on the laser spot within 0.1 °C of the measured value. Resulting fitted incident heat sources, representing plasmonic absorbed power, ranged from 0.0062 to 0.028 W. Alternatively, use of the experimentally measured optically extinguished powers resulted in over-predicted thermal responses, with estimated average ΔT reaching nearly 45 °C at 5.06 x10^{15} NP/cm^3 in the FEA model. To test the sensitivity of this fitting procedure, FEA-fitted powers were estimated by matching the entire film temperature within 0.1 °C of the measured value and by fitting power emitted, via radiation and convection, from the AuNP-PVP film face to values derived from the measured thermal profile. Heat source power values derived from the latter two methods varied by ~5%, within the size of symbol in Figure 11b, from fits based on average ROI temperature.

While power dissipated increased with AuNP concentration and optical extinguished power, the precision of simulated FEA-fitted heat dissipation was confounded by multiple effects. Most notably, measured thermal profiles are broadened relative to theoretical results. This suggested total heat dissipated in measured results is higher than predicted. The first possible culprit of this

54

disparity was use of the Au-free PVP thermal conductivity, k. However, a sensitivity analysis performed using k values varying from 0.27 W/mK, i.e. PVP, to 3.2 W/mK, a mass-average between Au and PVP at 5.06 x10^{15} NP/cm^3 showed negligible change in thermal profile. It appears that overall thermal dissipation within the model was dominated by the much thicker glass support layer, not the 70 nm thick Au-PVP layer containing the volumetric heat source approximating plasmonic absorption. In addition, suppressed heat dissipation compared to optically extinguished power could be attributable to saturation, edge effects, and laser-induced damage. Incident laser powers used in this work, ca. 800 mW, have been shown previously to exhibit saturable absorption effects.[50] Furthermore, the heat transfer coefficients used herein likely under predicted heat transfer from the film's narrow vertical surfaces as discussed in Section 3.1. As a result, measured and modeled temperature values diverged near film edges. Finally, evidence of laser induced damage, visible in the SEM images in Figure 11 may have suppressed magnitude of measured thermal response. While precise characterization of heat dissipation per unit optically extinguished power is confounded by the aforementioned effects, these results provide an important first approximation in sub-wavelength AuNP-PVP films.

3.3 Experimental & theoretical approaches

3.3.1 Measured thermal characterization

Each AuNP-PDMS and AuNP-PVP nanocomposite film was resonantly irradiated with a fiber-coupled 532 nm diode laser (MXL-FN-532, CNI, Changchung, CN) and its temperature profile was recorded with an infrared thermal camera (ICI 7320, P-Series, Beaumont, TX, USA). Infrared imaging captured thermal profiles of ca 5 mm x 5 mm AuNP-PDMS films suspended vertically

within the laser spot (ca. 1.0-2.5 mm diameter). Films were held in place at a single edge during experiments by tweezers. For AuNP-PDMS, the infrared camera was focused on the film face opposite incident laser irradiation to collect thermal data. Laser power was adjusted using a neutral density filter. During data collection, the experimental apparatus was covered to minimize forced convective effects.

Thermal images were recorded at 0.1-1 Hz during a 2-3 minute heating period under laser excitation and subsequent 2-3 minute cooling periods following laser shutoff for AuNP-PDMS. Power of the laser was recorded before and after each trial to ensure power did not fluctuate beyond a 5% threshold during data capture. Data was saved as TIFF images where temperature values at each image pixel (320 x 240 pixels per image) are recorded. The images were analyzed using MATLAB (Mathworks, Natick, MA, USA) to produce time-dependent temperature maps of both the entire film and the laser spot using rectangular and circular ROIs, respectively. Because conduction by the tweezers distorted the temperature distribution for first-generation AuNP-PDMS, only half of each film's thermal profile was used for calculations.

The thermal data capture setup was improved for AuNP-PVP films. Laser intensity was 100 W/cm^2, as measured from ca. 800 mW focused to a ca. 1 mm spot size. Light from the fiber-coupled laser was focused by a lens, passed through a 10° ground glass diffuser to give a uniform Gaussian output profile, and then focused finally onto the samples by a series lenses. Each sample was mounted with the PVP film facing the thermal camera. Thermal images were captured at 10 Hz over a 180 seconds with 90 seconds of heating (including 3 seconds of ambient) with the laser on and 90 seconds of cooling with the laser off. Thermal images were analyzed via MATLAB program using the circular ROI encompassing only the laser spot for each sample. Temperature

values at each pixel, with a resolution of 240 µm, within the ROI were averaged together to give average temperature values used for analysis.

3.3.2 Prediction of thermal response using Finite Element Analysis

The Heat Transfer in Solids module in COMSOL Multiphysics (COMSOL, Stockholm, Sweden) was used to calculate thermal profiles in AuNP-polymer films using an applied heat source, simulating thermalization following optical absorption of resonant irradiation. Radiative and convective cooling boundary conditions determine the rate of heat transfer to the ambient environment (air), while incident spatial power distribution and thermal diffusivity of the host polymer govern developed temperature gradients. AuNP-PDMS and AUNP-PVP films were given physical dimensions corresponding to measured length, width, and thicknesses. Density and specific heat capacity of AuNP-polymer films were estimated based on Au mass fraction and resulting weighted averages of Au and bulk polymer values. Au-free thermal conductivity was assigned to AuNP-PDMS and AuNP-PVP, since nanoscale dispersions not in physical contact typically have little effect on nanocomposite thermal conductivity.[111] Values of density, heat capacity, and thermal conductivity values for PDMS used were 970 kg/m^3, 1460 J/kgK, and 0.16 W/mK, respectively.[117] Values used for PVP were 1300 kg/m^3, 1380 J/kgK, and 0.27 W/mK and values for bulk Au were 19,300 kg/m^3, 128 J/kgK, and 318 W/mK, respectively.[118]

For first-generation AuNP-PDMS films, plasmonic heating from laser irradiation was approximated by using a volumetric heat source within the AuNP-PDMS films. The laser power distribution was approximated by evenly distributing the power between a center cylinder with a radius of 0.25 mm and seven concentric rings radiating outward with thicknesses of 0.25 mm each. This distribution was consistent with independent characterization using an adjustable aperture

and power meter and manufacturer information. For these films, FEA model heat source power was represented as measured spectral extinguished power, corrected for internal reflection, multiplied by incident laser power of 100 mW.

Results for second-generation AuNP-PDMS films used a Gaussian volumetric heat source centered at the measured laser spot center to represent laser irradiation. This Gaussian heat source produced better agreement between measured and simulated temperature profiles. A Gaussian pulse with a standard deviation of $r/2$, where r is the laser spot radius 1.5 mm, appeared to accurately represent the laser power distribution. Based on raw incident laser intensity (25 mW) and this Gaussian function, the actual irradiated laser power (I) was estimated, resulting in slightly suppressed powers ranging from 19-24 mW. Spectral extinguished powers (E) were attained from $E = I(1-10^{-A})$ where A is spectral extinction in absorbance units. Values of heat dissipated from the FEA model were determined via trial and error by adjusting heat source power until steady-state minimum and maximum temperatures within the laser spot were within 0.1°C of measured values. Measured two-dimensional thermal profiles from second-generation AuNP-PDMS at the first instant of cooling were projected into three-dimensional geometries compatible with COMSOL, enabling direct comparison.

Key concepts and approximations used in the FEA modeling approach are outlined below. In problems where thermal effects dominate mechanical considerations, the following approximation for the conservation of energy is appropriate at steady-state[119]

$$\rho C_p u \cdot \nabla + \nabla \cdot q = Q \qquad (3.1)$$

where ρ is density, C_p is heat capacity, u is the velocity vector, ∇ is the Del operator, T is absolute temperature, q is heat flux, and Q is the sum of external heat sources (or sinks). Heat flux in a solid is evaluated using Fourier's law, $q = -k\nabla T$, where k is thermal conductivity.

FEA is capable of solving this equation with a coupled heat transfer in non-isothermal laminar flow description of natural convection. However, in order to reduce computational expenditure, convective heat transfer coefficients were used to estimate boundary conditions for determination of AuNP-PDMS heat dissipation. Steady-state film temperatures using heat transfer coefficients were within ca. 2% of those determined from the 2D coupled model including non-isothermal laminar flow across a range of input heat source powers that resulted in film temperatures from 27 to 185 °C. Computational expense was reduced approximately 10^5 upon utilization of the heat transfer coefficients and made extension into a fully 3D description more practical. Validation and agreement between 2D models using either the coupled approach or convective heat transfer coefficients are discussed in more detail in Section 3.3.3.

In the latter approach used herein, heat flux at the solid-fluid interface is assumed to be proportional to a temperature difference across an imaginary thermal boundary layer. This is written mathematically as[119]

$$-n \cdot q_c = h(T_{inf} - T) \tag{3.2}$$

where n is normal vector to the film surface, q_c is convective heat flux, h is a heat transfer coefficient, and T_{inf} is the external temperature of the fluid far from the solid-fluid boundary. Textbook, empirically-derived heat transfer coefficients for natural convection from both horizontal and vertical plates were used in this work. Relations for a vertical (a) and horizontal (b) plate, respectively, are:[119]

$$h = \frac{k}{L}\left(0.68 + \frac{0.67\mathrm{Ra}_L^{1/4}}{\left(1 + \left(\frac{0.492}{\mathrm{Pr}}\right)^{9/16}\right)^{4/9}}\right) \qquad , \mathrm{Ra}_L \leq 10^9 \qquad (3.3a)$$

$$h = \frac{k}{L}0.54\mathrm{Ra}_L^{1/4} \qquad , \mathrm{Ra}_L \leq 10^7 \qquad (3.3b)$$

Where L is plate height and Pr is the Prandtl number, given as $\mathrm{Pr} = v/\alpha$, where v is kinematic viscosity and α is thermal diffusivity. The Rayleigh number, Ra_L, is a dimensionless ratio of buoyancy driven to conductive heat flux, given as:

$$\mathrm{Ra}_L = \frac{g\beta(T - T_{\mathrm{inf}})L^3}{v\alpha} \qquad (3.4)$$

Where g is the acceleration due to gravity and β is the coefficient of thermal expansion. For horizontal plates, L is typically given as plate area divided by perimeter.

In addition to natural convective flux, surface-to-ambient radiative flux was considered as an additional boundary condition. Mathematically, this is given as:

$$-n \cdot q_r = \varepsilon\sigma(T_{\mathrm{inf}}^4 - T^4) \qquad (3.5)$$

Where q_r is radiative heat flux, ε is emissivity, estimated as 0.85 for transparent PDMS and PVP, and σ is the Stefan-Boltzmann constant.

3.3.3 Validation of Finite Element approach

An initial FEA modeling approach used a 2D conjugate model to solve for the temperature profiles in a solid film while considering buoyancy-driven convection velocity profiles of the surrounding air. The results of this approach were validated with a pre-built model available from COMSOL previously shown to have excellent agreement with measured results.[120] The results of

the validated 2D coupled model were then compared to a subsequent model using heat transfer coefficients at the solid-fluid boundaries. This approach provided excellent agreement with significantly reduced computational expense necessary for development of the fully 3D model.

For the coupled model, the solid film is heated above the temperature of the surrounding air. The heated plate therefore warms the air near its surface, resulting in buoyancy-driven flow. Fluid flow of the air adjacent to the film may be described by the Navier-Stokes equations for non-isothermal flow. At the bottom and left system boundaries, the model assumes the temperature is equal to ambient conditions, i.e., $T = T_{inf}$. This is valid as long as the model boundaries are sufficiently large. Air rises upward and flows out through the top domain boundary. The no-slip boundary condition is applied the plate wall. All remaining boundaries are open, meaning that no forces act on the fluid; this is essentially the equivalent to extending the computation domains to infinity.

The available COMSOL model[120] calculates the temperature and velocity fields resulting from natural convection from this heated vertical plate. Surface temperature was varied in increments of 10 °C between 10 and 100 °C above ambient conditions (20 °C). The results of the simulation were validated by comparison with experimental results. Study of AuNP-PDMS films requires description of heat conduction within the solid film in addition to convective heat transfer rates. As is, the original model was not sufficient for this purpose since the surface was heated only at the domain boundary. An almost identical FEA model was created where the AuNP-PDMS solid film was given a height (5 mm) and thickness of 0.34 mm (half the film thickness; axial symmetry). The resulting temperature and fluid velocity profiles at 50 °C (ΔT = 30°C) were within 1% and 4%, respectively, of the model excluding the solid film from the domain.

The final step was introduction of a volumetric heat sources (W/m^3) needed for the subsequent 3D model employed in Section 3.1 and 3.2. The entire heated solid was placed in a 2D domain sufficiently large for proper implementation of the outlined boundary conditions. Results with the abridged model showed excellent agreement with results considering non-isothermal fluid flow; a maximum percent difference of 2.3% in steady-state film temperature was obtained across three orders-of-magnitude in applied heat source power. Resulting steady-state film temperatures were within 0.5 °C across the range of heat source powers used in actual AuNP-polymer simulations. Accurate description of heat transfer in 3D AuNP-PDMS films with the compact FEA approach developed herein is an important advancement in characterization of plasmonic heat dissipation in hybrid nanomaterials.

4. *GOLD NANOPARTICLE-DECORATION OF TUNGSTEN DISULFIDE*

Layered materials represent a diverse, emerging source of two-dimensional (2D) nanostructures with exotic optoelectronic properties and high surface area-to-volume ratios. While graphene is the most ubiquitous of these materials, emerging direct bandgap semiconducting 2D transition metal dichalcogenides (TMDs) have broad application in optoelectronics,[121,122] sensing,[123,124] photodetection,[125] and solar fuel production.[126] These materials consist of a transition metal, such as molybdenum or tungsten, sandwiched between chalcogenide atoms, e.g. sulfur or selenide. Strong covalent bonds bind this molecular structure; however, adjacent sheets are held together with relatively weak van der Waals forces to form bulk three-dimensional crystals. TMDs have been studied for decades, but interest in their layer-dependent properties and role as atomically thin semiconducting materials is recent. For example, TMDs such as tungsten disulfide (WS_2) and molybdenum disulfide (MoS_2) have a transformation from an in-direct to direct bandgap due to quantum confinement altered band structures.[121] Direct bandgap optical excitation enhances optical extinction and permits efficient photoluminescence (PL) from single layer MoS_2 and WS_2.

Lack of scalable, reproducible fabrication techniques limits implementation of these emerging 2D TMDs. 2D TMDs have traditionally been produced by mechanical exfoliation,[127] bottom-up chemical vapor deposition (CVD),[128] or chemical exfoliation.[129] Monolayer TMD fabrication has been limited either by difficulty, scalability, or cost.[130] Both CVD and mechanical exfoliation can provide high quality, large area monolayers, but cost for the former and scalability for the latter limit their utility. Liquid phase exfoliation (LPE), which uses sonication or shearing of bulk crystals, represents a potentially scalable method of producing few layer TMD nanosheets.[131–133]

63

LPE has been exploited to produce a wide range of 2D materials such as graphene, boron nitride, TMDs, oxides, and black phosphorus.[131,133–137] However, broad lateral size and thickness distributions of exfoliated nanosheets remain problematic. Metal decoration of scalable LPE WS_2 nanosheets could permit facile reduction of TMD size distribution by facilitating removal of undesirable multi-layer flakes, while also exerting a measure of control over optoelectronic properties.

Utility of TMDs has also been limited in part by difficulty tuning the intrinsic optoelectronic excitation and damping mechanisms.[130] For example, monolayer tungsten disulfide (WS_2) absorbs less than 2% of broadband UV-vis radiation, cannot interact with light above ~620 nm in wavelength, and exhibits a characteristic photoluminescence (PL) response depending only on number of layers.[121,138] Addition of AuNPs could address each of these issues by enhancing intrinsic WS_2 absorption, modulating PL response, and serving as an independent source of charge carriers. Plasmon-induced local electric fields increased WS_2 PL 11-fold upon maximization of plasmon-exciton coupling,[139] while PL quenching attributed to p-doping of molybdenum disulfide (MoS_2) from adjacent AuNPs has been reported.[140] Damping of plasmon energy into hot electrons in AuNPs may be transfered to adjacent 2D semiconducting TMDs.[141–145] Improvement in photocatalytic hydrogen production,[146,147] organic photovoltaics,[148] and photodectors[18,149,150] have been attributed to this hot electron transfer (HET). This plasmon damping mechanism is distinct from conventional radiative and nonradiative mechanisms and is unique to interfacing non-insultive media, like TMDs, with NPs.[151]

The work herein demonstrated enhancement of WS_2 monolayer content and optical absorption and emission by utilizing *in situ* AuNP reduction to facilitate removal of undesirable multi-layer nanosheets. $AuCl_3$ preferentially reduced on multi-layer WS_2, resulting in large Au aggregates

64

easily separated from the colloidal dispersion. State-of-the-art PL/Raman ratios, an important metric for quality of semiconducting TMDs, were enhanced from 4 up to 16, while mean layer number was reduced from 2 to 1.1.[138,152,153] Optoelectronic characteristics of mostly monolayer Au-WS$_2$ were improved both from enrichment in WS$_2$ monolayers and the LSPR. Enhanced broadband optical extinction from plasmon-exciton interactions was observable in both measured and discrete dipole approximation (DDA) results. Plasmonic HET across a physiochemical metal-TMD bond was measured and simulated for the first time using electron energy loss spectroscopy (EELS) and DDA. Taken together, these improvements in fabrication techniques and optoelectronic tunability represent an important advance in the study of TMD materials for use in optoelectronic and photocatalytic applications.

4.1 Spontaneous AuNP edge decoration of WS$_2$ nanosheets

Metal decoration of 2D TMDs modifies the optoelectronic properties, allowing their properties to be tuned for use in surface-enhanced Raman spectroscopy (SERS),[154] rechargeable batteries,[155] biosensing,[156–158] and optoelectronic devices.[18,148–150] Decoration of metal NPs, particularly Au, have been performed on both chemically-exfoliated and CVD grown MoS$_2$.[159,160] Reduction of metal salt occurs spontaneously without the need for reducing agents. No evidence of covalent bonding has been reported in these previous studies; it is suggested that excess electrons on CE nanosheets act as the AuCl$_3$ reducing agent, resulting in AuNPs physisorbed to TMD nanosheets. Reduced NPs are located primarily at exposed sulfur (S) atoms, which occur primarily at edge and defect sites. Size and morphology of reduced NPs can be controlled by reaction conditions and metal salt concentration.[159,161] However, use of *in situ* reduction, resulting in covalent Au-S bonding, to allow facile removal of undesirable multi-layer nanosheets has not been reported.

4.1.1 Developed protocol for fabrication of Au-WS$_2$ nanosheets

Initial experiments reducing AuNPs onto WS$_2$ showed key changes in both physical and optoelectronic properties. This section outlines procedure and spectral metrics used for fabrication of Au-WS$_2$ nanostructures. Stock dispersion of WS$_2$ used were dispersed at a concentration of 0.5 mg/ml in 3 mg/ml aqueous sodium cholate (SC). Optical extinction at 235 nm (I_{235}) may be used to determine nanosheet concentration from an empirically-derived Beer-Lambert extinction coefficient.[138,153] Size-dependent edge contributions affect nanosheet spectral profile; however, previous work found edge and basal contributions to optical response cancel at 235 nm in WS$_2$. In addition to edge effects, excitonic transition spectral location shifts with nanosheet thickness from confinement and dielectric screening effects. With these considerations, mean flake layer number, N, may be calculated from the A exciton wavelength, λ_A,[138,153] via $N= 6.35\times10^{-32}e^{\lambda_A/8.51}$.[138,153] Mean sheet length, L, was calculated from the ratio in absorbance at two particular wavelengths capturing size-dependent scattering behavior[60,133] arising from edge confinement via[138,153]

$$L = \frac{2.3 - \frac{I_{235}}{I_{290}}}{0.02\frac{I_{235}}{I_{290}} - 0.0185} \qquad (4.1)$$

where I_{290} is spectral extinction at 290 nm.[138,153] N and L error estimated with these metrics was found to be less than 10%.[138] Nanosheet dimensions vary between batches, but generally large nanosheets (l-WS$_2$) are on the order of 90-160 nm in length and 3-8 layers thick, while medium flakes (m-WS$_2$) are about 40-75 nm with 2-5 layers on average.

These stock 0.5 mg/ml (2 mM) WS$_2$ dispersions were mixed 1:1 by volume with aqueous AuCl$_3$ at concentrations double the desired final Au concentrations of 0.5, 1, 2, 5, 7.5, and 10 mM. Stoichiometric ratio of Au to WS$_2$, 0.25 to 5 in this initial sample set, was used to compare sample

results across different samples batches. Following mixing of $AuCl_3$ and WS_2, samples sat undisturbed for 4-16 hours covered in foil, mitigating any light-induced effects. Successive purification steps were then performed to remove unreacted $AuCl_3$ and any large Au aggregates formed. After the reaction period, the aqueous Au-WS_2 solution was centrifuged at 15000 rpm (22000g) for 90 minutes. Normally stable colloidal dispersions crashed after ca. 30 min for $AuCl_3$ concentration above 2 mM in the mixture, attributable to decreased pH following addition of $AuCl_3$.

The supernatant, including very small WS_2, surfactant, and unreduced $AuCl_3$, was collected for further analysis. No $AuCl_3$ was detected in the supernatant at Au:WS_2 stoichiometric ratio = 1. However, unreacted $AuCl_3$ was found in samples with the higher initial ratio $AuCl_3$:WS_2 = 5. A precise quantification of the $AuCl_3$ concentration was not possible due to changes in the spectral shape likely attributable to differences in pH and ionic strength versus the $AuCl_3$ reference. The sediment containing the Au-decorated WS_2 was re-dispersed in 3 mg/ml aqueous SC at the same volume as the initial WS_2 dispersion. This dispersion was then centrifuged at 500 rpm (30g) to remove large aggregates visibly formed at higher Au concentrations. Figure 12f schematically describes this Au-decoration procedure. Subsequent purification steps ranging from 1000 rpm (110g) to 2000 rpm (420g) could then be implemented to help separate nanosheets by size and AuNP content.

A second set of Au-decorated WS_2 samples were fabricated to facilitate transmission electron microscopy (TEM) imaging and characterization of NP size and density as a function of Au-WS_2 molar ratio. WS_2 nanosheets with an average length of 60 nm and 2 mean average layer number, based on the UV-vis metrics,[138] were used in this analysis. These nanosheets are ideal since they have a much higher monolayer content than larger nanosheets, but are dispersed at much higher

concentration than smaller nanosheets trapped at higher centrifugation speeds. Stock WS_2

concentration was lowered to 0.1 mg/ml (0.4 mM) to reduce WS_2 aggregation that may occur

during the reaction and subsequent workup. Upon mixing $AuCl_3$ 1:1 by volume with the stock

WS_2, resulting Au:WS_2 ratios were 0.2, 0.4, 0.8, and 1.7. Ratios used were lower in this sample

set as the large number of Au aggregates formed at molar ratios above 2 made optical and

microscopy characterization more difficult. Figure 12a-f shows TEM (Titan 80-300; FEI,

Hillsboro, OR USA) images of several representative Au-decorated nanosheets at an Au:WS_2

stoichiometric ratio of 0.8. Figure 12a-c show an example of predominately edge decorated

nanosheets found throughout the sample at increasing magnification. High-resolution TEM

(Figure 12c) show individual atoms, boundaries between Au and WS_2, and crystal grain boundaries

within single AuNPs. Merging of distinct AuNP nucleations, evident by their substantial degree

of polycrystallinity, and heavier basal plane decoration of multi-layer nanosheets are evident in

Figure 12d-f.
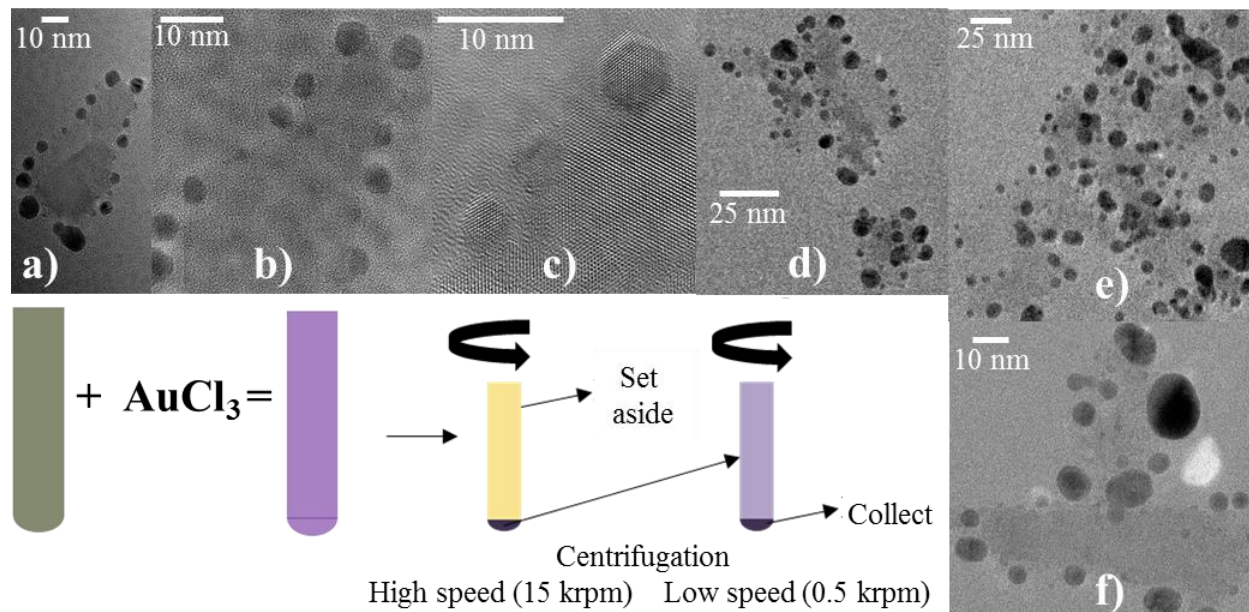
Figure 12: a-f) Au-decorated WS_2 TEM images and g) Au-decoration fabrication protocol.

TEM-based estimation of NP size and coverage on a sample of 5-8 nanosheets for Au-WS$_2$ ratios of 0.4, 0.8, and 1.7 was performed using a MATLAB script previously developed within the group.[162] Total number of NPs per square micron (NPs/μm^2) of WS$_2$ was 11000, 7500, and 8500 for the 0.4, 0.8, and 1.7 Au-WS$_2$ ratios samples, respectively. Using a NP diameter cut-off excluding AuNPs below 5 nm, NPs/μm^2 was 2000, 4000, and 3000 for the 0.4, 0.8, and 1.7 Au-WS$_2$ ratios samples, respectively. The cut-off was used to exclude the small Au nucleation sites that occur regularly around the WS$_2$ edges. Concomitantly, average NP diameter using the 5 nm cut-off increased slightly from 7 to 8 nm with increasing Au-WS$_2$ ratio, but showed no clear trend when including all AuNPs counted. This analysis provides the first step towards microscopically characterizing these samples, but more finely tuned fabrication and purification steps were needed to give a broader range of AuNP sizes and decoration density.

Subsequent collaborative efforts refined fabrication and separation cascades to better control resulting NP size and coverage.[152] SC concentration (C_{SC}) was varied between 0.1 mg/ml and 40 mg/ml to test impact on resulting Au reduction. Mean nanosheet length and monolayer volume fraction increased with increasing C_{SC}, suggesting SC participates in the reaction. Au content relative to WS$_2$ was estimated using a 560/410 nm optical extinction ratio. Au content derived from extinction spectra was significantly reduced after centrifugation at C_{SC} = 1 mg/ml across the AuCl$_3$:WS$_2$ stoichiometric ratio range tested; differences before and after centrifugation were less pronounced for C_{SC} =10 mg/ml. A concentration of C_{SC} = 0.5 mg/ml was therefore used for the final fabricated samples to maximize monolayer enrichment.

Cascade centrifugation[153] was utilized to purify the Au-WS$_2$ stock dispersion by decreasing mean layer number and removing larger Au nanostructures. The final protocols created a broad range of Au-WS$_2$ dispersions with controllable AuNP decoration and improved final monolayer

content; each centrifugation sub-protocol varied based on initial nanosheet dimensions and AuCl$_3$:WS$_2$ stoichiometry.[152] A combination of conventional UV-vis and PL spectroscopies suggested enrichment in monolayers following the optimized purification steps. No changes in PL peak shape or position were discerned from the resulting liquid dispersions, suggesting AuNPs had minimal effect on the TMD optical properties. PL was widely retained in deposited Au-WS$_2$ films, suggesting WS$_2$ restacking was mitigated by the presence of AuNPs. Finally, AFM measurements corroborated monolayer enrichment and indicated monolayer enriched nanosheets are significantly larger than in previously reported procedures.[153]

4.1.2 Evidence and proposed mechanism of in situ AuNP reduction on WS$_2$

X-ray photoelectron spectroscopy (XPS), a technique to probe elemental composition and electrochemical states, performed by collaborators confirmed Au-S bonding in fabricated samples. XPS was measured on thin films deposited from aqueous WS$_2$ dispersions before and after reaction with AuCl$_3$. In contrast to the WS$_2$ reference, a clear Au^0 signature was detected in the Au-WS$_2$ sample. Two additional peaks shifted by ~1 eV to lower binding energies suggested presence of partially-reduced S species and covalent Au-S bonding. WS$_2$ core level spectra remained virtually unchanged, suggesting no damage to the WS$_2$ nanosheets resulted from the reaction.

Variation in initial C$_{SC}$ suggested that SC participates in the Au reduction. High C$_{SC}$ (>10 mg/ml) facilitated growth of large Au-WS$_2$ nanostructures, and monolayer enrichment occurred even at low AuCl$_3$:WS$_2$ stoichiometry ratio. The amount of stably dispersed AuNPs decreased, as these large nanostructures readily precipitate. However, no covalent Au-S bonds would form if SC was the only reducing agent. Furthermore, no change in the AuCl$_3$ spectrum was observed in SC

dispersions absent WS_2. Taken together this suggested that while SC does impact growth of larger Au structures, WS_2 is crucial for initial Au nucleation.

The proposed reaction mechanism for Au-decoration of WS_2 is as follows. $AuCl_3$ first reacts with easily accessible edge and defect S in WS_2. These locations serve as nucleation sites for initial growth of small AuNPs as evident by covalent Au-S bonding. Reduction of unreacted $AuCl_3$ by SC adsorbed on the WS_2 surface supplies additional Au^0 for nanostructure growth. These nanostructures grow together and eventually precipitate from the dispersion. This preferentially occurs at edge terraces of incompletely exfoliated, few-layer nanosheets, where AuNP seeds are already covalently bound to WS_2. This occurs because of a higher relative SC concentration on the basal plane in comparison to edges. This preferential growth of larger Au structures on these few-layer nanosheets leads to an enrichment in WS_2 monolayers following their removal. SC may be oxidized during this reaction, but could be replaced by an adsorption/desorption process when excess SC is present in solution; this results in the more efficient monolayer enrichment at higher surfactant concentrations.

4.2 Optical characterization of AuNP-decorated WS_2

Both measured spectroscopic and theoretical description are important for analyzing physical, optical, and electronic properties of Au-decorated TMDs. Conventional far-field UV-vis transmission spectroscopy yields wavelength-specific optical extinction; relative extinction peak heights facilitate accurate estimate of nanosheet size and thicknesses without the need for extensive microscopic characterization.[153] Photoluminescence (PL) emission spectroscopy can similarly be used to estimate both relative monolayer content[138] of exfoliated nanosheets and elucidate signatures of plasmon-exciton coupling in Au-decorated TMDs.[149] Numerical methods like DDA

can characterize excitation and dissipation pathways of plasmon-excitonic modes in both the near- and far-field,[163] providing key insight and validation of experimental measures.

4.2.1 Measured optical spectroscopic characterization of Au-WS$_2$

Au-decoration modified far-field spectral extinction of WS$_2$ nanosheets. Figure 13 shows spectral intensity of the initial mWS$_2$ batch mixed with AuCl$_3$ content at molar Au-WS$_2$ ratios ranging from 0.25 to 5. Au-free WS$_2$ spectra indicates characteristic peaks associated with excitonic transitions visible at ca. 400, 515, and 620 nm refered to as the A-, B-, and C-exciton, respectively. Negible optical extinction past 650 nm is attributable to the semiconducting behavior of monolayer WS$_2$; light at longer wavelengths has insufficient energy to excite valence electrons into the conduction band of WS$_2$. As Au:WS$_2$ stoichiometric ratio increases, optical extinction generally increases from 500-650 nm. At Au:WS$_2$ ratios of 2.5 to 5, the separate spectral features at ca. 520 nm, from the B-exciton and LSPR, and 620 nm, the A-exciton, overlap to form a large extinction peak at ~545 nm.

Time lapse optical spectra of a Au:WS$_2$ = 1 sample indicates the Au-reduction has largely concluded within 15 minutes. As shown in Figure 13b, a clear transient behavior in measured optical extinction is observed at time intervals up to 15 minutes. Following this transient period, measured optical extinction remains relatively constant before dropping at 180 minutes. This drop is attributable to either a shifting baseline inherent in the experimental setup over extended intervals or from precipitation of Au aggregates formed during the reaction. While these results indicate the rate of the initial reduction step, resolution was not sufficient to elucidate any secondary reactions involving the re-orientation or distribution of reduced Au atoms.
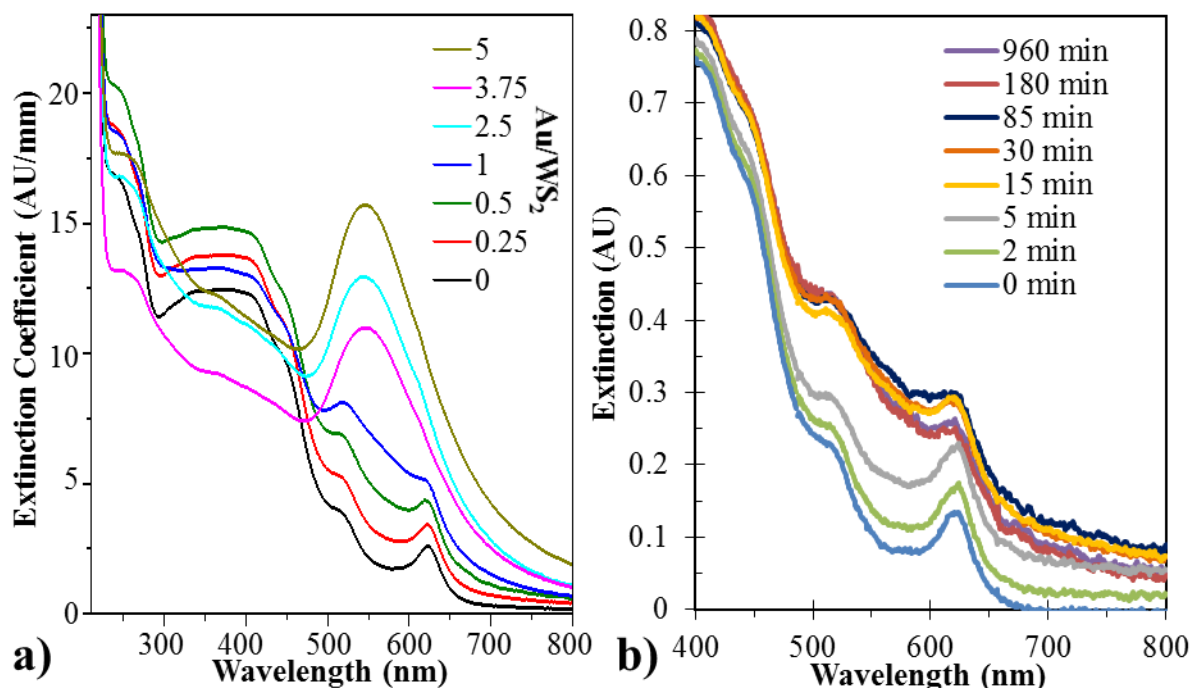
Figure 13: a) Measured optical extinction for Au-decorated WS_2, b) time lapse optical extinction during reaction at $Au:WS_2$ ratio $= 1$.

More finely tuned purification via centrifugation allowed separation of Au-WS_2 by degree of Au-decoration. Figure 14a illustrates change in supernatant optical extinction spectra following sequential centrifugation steps from 500 to 2000 rpm for an Au:$WS_2 = 1$ sample. Spectra were normalized at 295 nm to account for loss of sample at each step. As centrifugation force increases, highly Au-decorated nanosheets and free AuNPs are removed. For the 500 rpm supernatant, the spectral features at ca. 510 and 620 nm are broadened into a single peak due to the large amount of AuNPs present. However, as centrifugation force increases, the distinct spectral features consistent with Au-decorated WS_2 at the lower stoichometric ratios, as shown in Figure 14a, become visible. This purification of the colloidally dispersed Au-W_{S2} fraction by additional centrifugation steps was an important component of a subsequent collaborative study.[152]
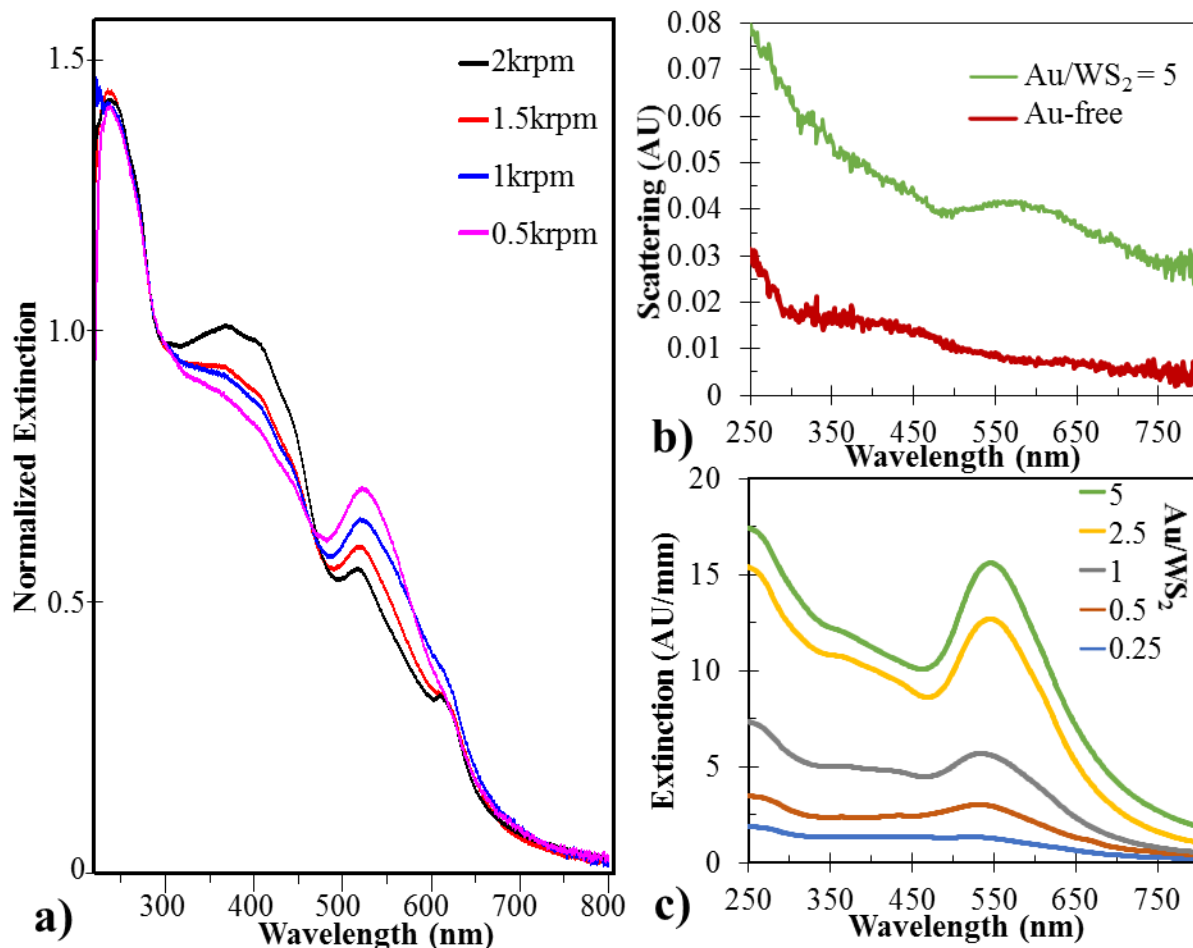
Figure 14: a) Spectral extinction for supernatant following each purification step, b) scattering spectra for Au-free and Au-decorated WS$_2$, c) spectral-subtracted AuNP spectra.

Transmission and reflection data measured using an integrating sphere setup helped distinguish optical extinction contributions from scattering and absorption. In this setup, both transmitted light and scattered light exiting the cuvette obliquely are collected by an integrating sphere (discussed in more detail section 4.4.3). WS$_2$ nanosheets absent AuNPs scatter little light, as illustrate in Figure 14b. However, broadband scattering relative to Au-free WS$_2$ was increased approximately 5-fold in the Au:WS$_2$ = 5 sample. The scattering peak at approximately 570 nm is characteristic of the presence of larger AuNPs in the 40-60 nm diameter range. The overall magnitude of scattering

is still rather low, since the predominance of small AuNPs less than 20 nm would not be expected to exhibit a large scattering signal, as discussed in Chapter 2.

Characterization of reduced AuNP (rAuNP) optical extinction can provide additional insight into AuNP size and concentration. Overlap between the B-exciton and AuNP plasmon resonance required spectral substraction to accurately characterize spectral contribution of rAuNPs. Taking the second derivative of the composite spectra helped resolve the A-exciton peak. The height of the A-exciton peak relative to the reference WS_2 spectra quantified the amount of WS_2 remaining in the dispersed fraction. This Beer-Lambert law approximation assumes the nanosheet dimensions are not appreciably different for the Au-decorated WS_2 and Au-free WS_2 reference spectra. The reference spectra at reduced magnitude, i.e. the estimated amount of WS_2 remaining, was then substracted from the composite spectra to yield AuNP spectra; these spectra, shown in Figure 14c, are analogous to aqueous AuNP dispersions. LSPR peaks evolved from 540 to 550 nm as Au:WS_2 ratio increased. While the effective dielectric environment of these AuNPs is likely increased from adjacent WS_2, this 10 nm LSPR red-shift would represent an increase in AuNP diameter from ca. 60 to 75 nm in a purely aqueous environment ($n = 1.33$).

Analysis of A-exciton energy and location showed no clear impact from Au-decoration. This suggested nanosheet optical response is not dramatically altered by the presence of edge-decorated AuNPs. WS_2 nanosheet size and thickness were estimated from these subtracted spectra using emperical metrics that input peak locations and relative extinction magnitudes across the UV-vis spectrum, as discussed in Section 4.1.1.[153] Figure 15 plots spectral-derived WS_2 concentration and mean number of layers for both medium (m-WS_2) and large (l-WS_2) nanosheets following purification steps to remove free AuNPs and aggregates. The metrics suggest a significant amount of WS_2 was lost during the purification steps as evidence by a ca. 50- and 200-fold drop in WS_2

concentration for m-WS$_2$ and l-WS$_2$ nanosheets at increasing stoichiometric ratio, as shown in Figure 15a. Significantly, much of the lost WS$_2$ appears to be undesired multi-layer flakes, as evidence by the up to 5-fold reduction in mean number of layers in Figure 15b. These results suggest AuCl$_3$ preferentially reduced on multi-layer nanosheets, resulting in large Au aggregates at increasing AuCl$_3$ concentrations. Since these aggregates were easily removed during centrifugation purification steps, only moderately-decorated, monolayer WS$_2$ flakes remained.
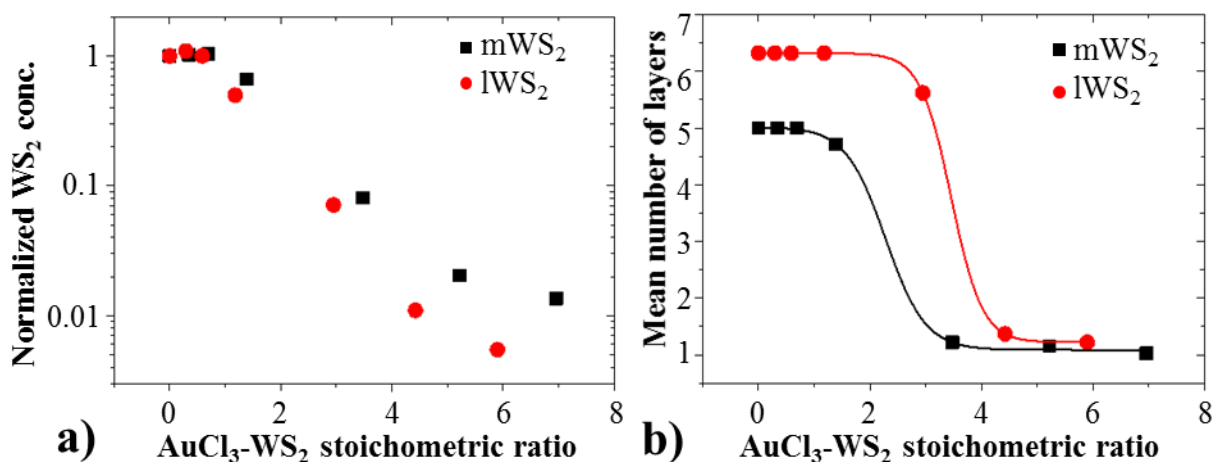
Figure 15: Spectral metric-derived estimate of a) remaining WS$_2$ concentration and b) mean number of TMD layers following Au-decoration.

PL spectroscopy provided another metric for evaluating resulting TMD monolayer content, as well as possible plasmon-exciton coupling effects on light emission. For PL measurements, light excitation supplied by a 532 nm laser was incident on small droplets of aqueously dispersed Au-WS$_2$. The experimental apparatus is described in more detail in section 4.4.3. Light emission intensity was normalized using the intrinsic Raman peak at ca. 400 cm^{-1} associated with lattice vibrations in WS$_2$, whose intensity depends only on total WS$_2$ content. This peak is used to normalize PL signal since actual concentration of interrogated WS$_2$ during the measurement is not precisely known. The characteristic PL peak associated with the A-exciton/band gap emission is

visible at ca. 2500 cm^{-1}, as shown in Figure 16a. Normalized PL emission is enhanced more than

an order of magnitude as Au:WS$_2$ ratio increases to 5. Enhanced PL from TMDs is of immense

interest for emerging optoelectronic devices.[149,164] The characteristic Raman peak for water, visible

at ca. 3400 cm^{-1}, increases in the normalized spectra with increasing Au:WS$_2$ ratio since the

effective WS$_2$ concentration is decreasing.
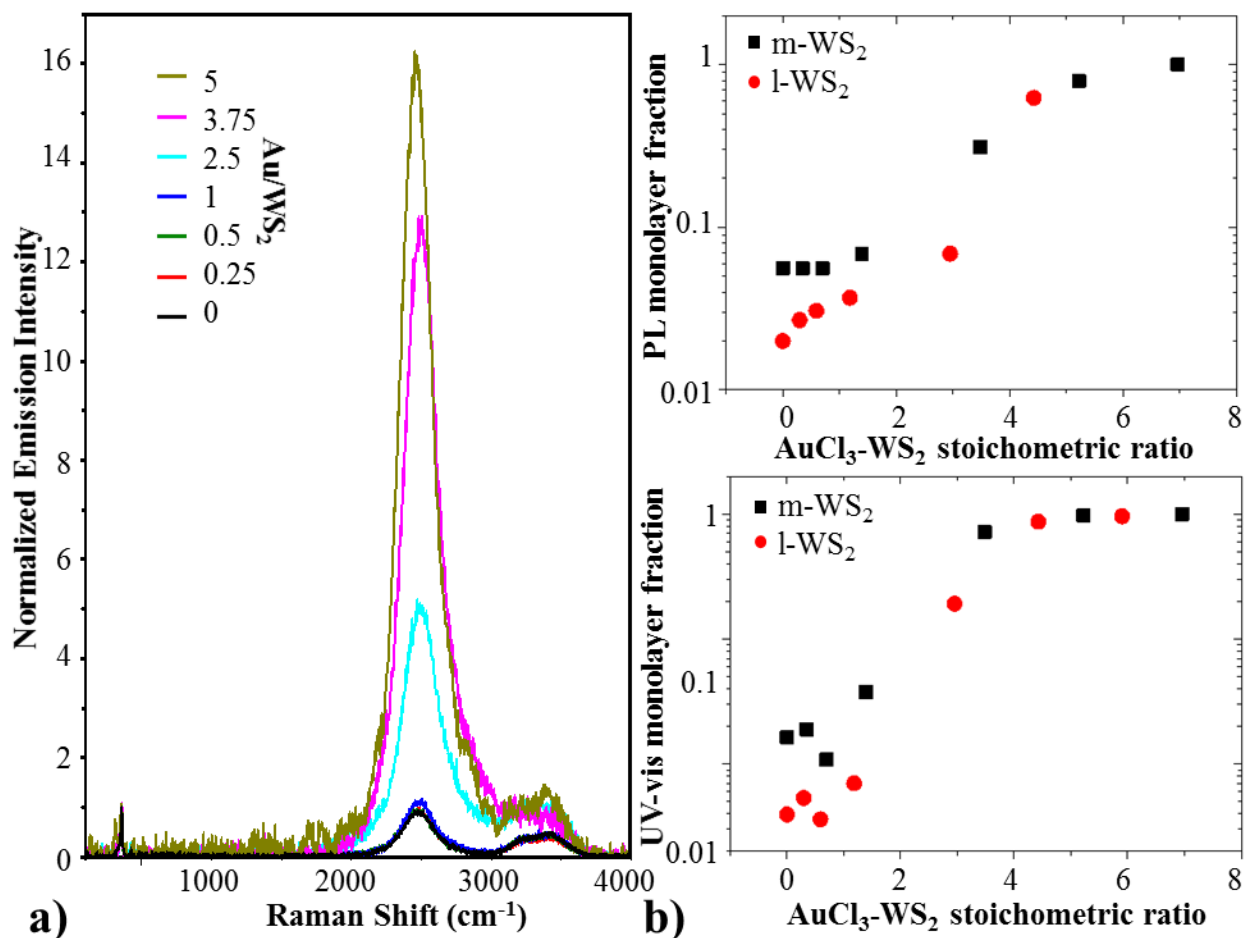
Figure 16: a) PL from Au-WS$_2$ samples normalized to WS$_2$ Raman signal, b) WS$_2$ monolayer fraction estimated from both PL and UV-vis spectra.

Based on the results in Figure 16 and that of the subsequent collaborative study,[152] AuNP

reduction on WS$_2$ appears to have minimal impact on PL emission beyond monolayer enrichment.

PL from undoped TMDs depends almost exclusively on number of layers.[165] Figure 16b shows

excellent agreement between PL and UV-vis spectroscopic estimates of WS_2 monolayer content based on location and bandwidth analysis of the A-exciton;[153] each predict a nearly two-order of magnitude enhancement in final monolayer content. This could be due in part because PL emission is typically most intense on the basal plane of WS_2 nanosheets,[166] whereas the majority of reduced AuNPs appear on edge sites. Maintaining PL emission was a promising result, since PL quenching was reported prior when AuNPs were in physical contact with adjacent MoS_2.[140]

4.2.2 Discrete dipole approximation of Au-WS$_2$ optical response

Nano architectures with plasmonic NPs supporting localized electromagnetic fields can affect optical excitation and carrier dynamics in adjacent 2D TMD semiconductors. Theoretical description of these systems guides intuition and validates measured results. Accurate description of inhomogeneous NP-2D TMD heterostructures are important for understanding samples produced within current fabrication capabilities. The discrete dipole approximation (DDA) to Maxwell's equations used herein allowed characterization of optoelectronic excitation and dissipation pathways in Au-WS$_2$ structures. Far-field UV-vis transmission spectra showing LSPR and excitonic transition features of Au-WS$_2$ heterostructures were modeled using DDA package DDSCAT v7.3.[37,73,91] Simulated far-field transmission spectra may be compared directly with measured results, while local electric near-field maps offer important insight into local plasmon field enhancements into adjacent TMDs. DDA is ideally suited to study a wide range of arbitrary nanoparticle-dielectric systems due to its relatively low computational expenditure and volumetric treatment of target geometries. Recently, DDA was used to model plasmon excitation and damping of AuNPs and Ag nanoprisms dropcast onto MoS_2.[163]

78

DDA results indicated that edge decoration of AuNPs on WS_2 provides higher optical extinction efficiency than basal plane decoration. Figure 17 shows simulated response in a media RI = 1.33, i.e. water, for an Au-free WS_2 monolayer measuring 75 x 50 nm, a 20 nm AuNP, WS_2 with the AuNP centered on the basal plane, and WS_2 with the AuNP centered on the 75 nm nanosheet edge. Polarization was averaged in the x- and y-directions and the plane wave k-vector was normal to the target (z-direction). Generally, AuNP-decoration enhanced broadband extinction across the wavelength range examined. Enhanced extinction, particularly at the A-exciton (~620 nm), is noteworthy since the AuNP is off-resonance at this energy; this suggests even larger enhancements could be observed when tuning the LSPR wavelength to specific excitonic transitions.[163] For example, overlap between the comparatively weak B-excitonic feature and the LSPR at ca. 520 nm resulted in a more than 2-fold increase in optical extinction.

Plasmonic energy dissipation from the AuNP to the WS_2 were probed near the LSPR/B-exciton peak (520 nm) and the A-exciton peak (620 nm) for side-decorated Au-WS_2 as shown on the right side in Figure 17. Near-field plots for y-polarization at both 520 and 620 nm indicate the intense local field-enhancements at the AuNP-TMD interface. Plasmon excitation results in a dipolar LSPR on the AuNP and lateral energy transfer into the WS_2 monolayer at the axial contact point. Differences are observed for each plot. At 520 nm, the AuNP LSPR field enhancement near the particle is stronger than off-resonance (620 nm). The local field enhancement at the edge of the nanosheet, reaching up to ca. 4, is stronger at the A-exciton (620 nm) due to stronger optical absorption relative to the B-exciton (520 nm). Radiative recombination, e.g. PL, could result from enhanced field intensity at WS_2 edges, but DDA cannot attribute far-field scattering to a specific point of origin. DDA likewise cannot represent particular edge states or changing spatial electron density as in density functional theory (DFT).

79
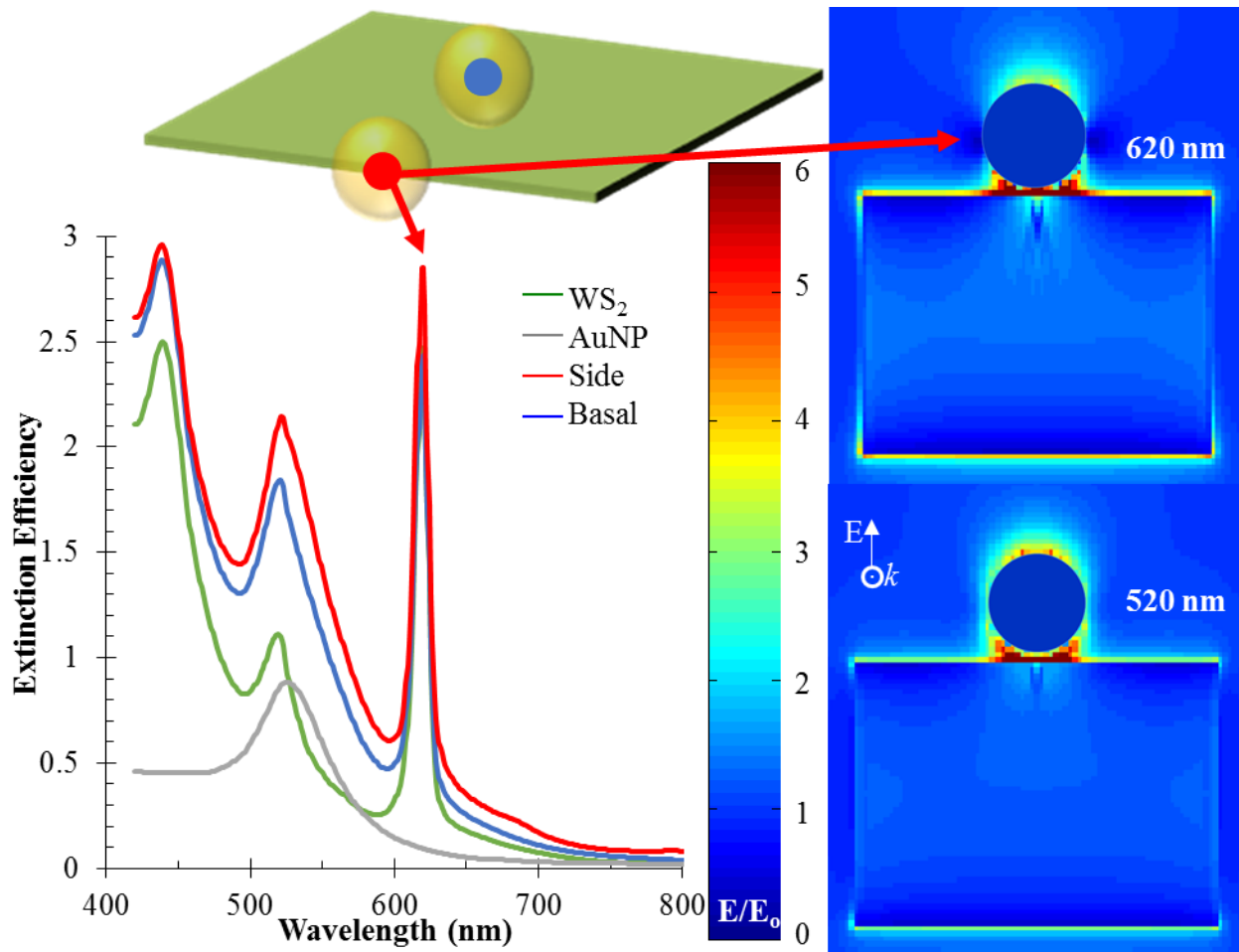
Figure 17: DDA optical extinction of Au-free WS$_2$, 20 nm AuNP, and 20 nm AuNP on nanosheet edge and basal plane with simulated near-field plots (right) at 520 and 620 nm.

Conversion of a TEM image of an actual Au-decorated WS$_2$ nanosheet to a DDA target allowed optical characterization of a much less idealized geometry for comparison with both measured and simulated results. Figure 18 plots DDA extinction efficiency of this generated target for polarization averaged in the x- and y-direction. Extinction enhancements over the entire visible spectrum were comparable to the rectangular WS$_2$ nanosheet with side-decorated 20 nm AuNP shown in Figure 17. Optical extinction was enhanced up to 1.8-fold at ca. 520 nm where the B-exciton overlaps the coupled AuNP LSPR. Extinction efficiency may be converted to optical

extinction in AU by the method described in Chapter 2 for CDA, but is beyond the scope of this work. The inset shows the local field enhancements of ca. 5 at 520 nm along the Au-decorated WS$_2$ nanosheet edge. Deconvolution of the simulated spectra and local near-field enhancements in Figures 17 and 18 are the subject of ongoing work. However, these results appear to validate DDA as a useful tool to guide design of plasmon-exciton interactions in NP-decorated TMDs such as WS$_2$ that have published dielectric data.[167]
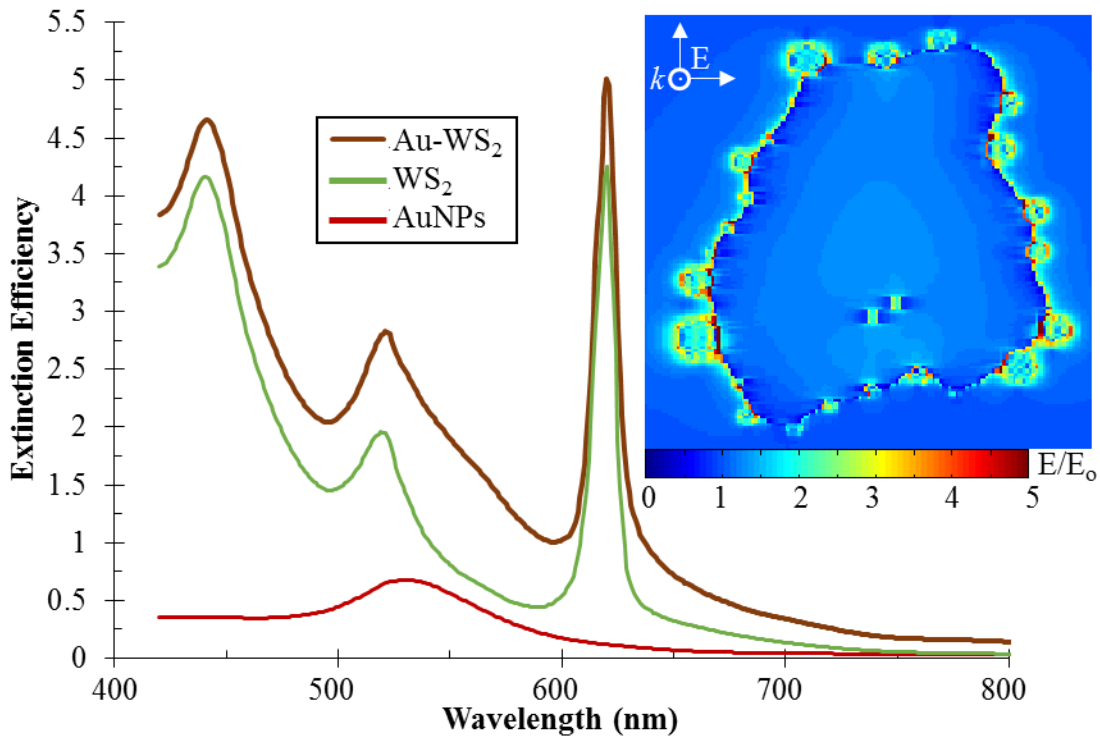
Figure 18: DDA extinction of custom Au-WS$_2$ target replicated from actual TEM image, inset simulated near-field plot at 520 nm.

4.3 Plasmonic hot electron transfer in Au-WS$_2$

Hot electron damping of plasmon energy transfered to adjacent 2D semiconducting TMDs has been implicated in enhancement of various emerging applications.[141–145] Hot electron transfer (HET) may occur on a femtosecond scale after plasmons decay into an electron-hole pair.[16] If the

energy of the "hot" electron is greater than the Schottky barrier (~0.6 eV for Au/WS$_2$) the electron may be injected into the conduction band of the adjacent semiconductor.[168] Characterizing and controlling HET in NP-2D TMD heterostructures is important for understanding fundamental interactions and optimizing application-specific plasmonic enhancements. HET dampens the plasmon resonance, but may be utilized to generate charge carriers at sub-bandgap energies in semiconductor optoelectronic devices.[141] In particular, HET may provide an additional source of energetic carriers to facilitate catalytic reactions.[17] In contrast, systems hoping to leverage local field enhancements, such as nonlinear harmonic generation, should seek to minimize this energetic damping mechanism.

HET from AuNPs into TMDs has been examined using both femtosecond scale pump-probe transient absorption spectroscopy[169] and electron energy loss spectroscopy (EELS).[170] EELS performed in a scanning TEM (STEM) was used herein to help characterize energy losses and plasmon decay pathways in hybrid NP-TMD systems.[171] Energy loss of incident electrons to a nanostructure provides insight into plasmon modes on metal NPs and TMD semiconductor excitonic transitions. Bandwidth of plasmon modes in EELS may be used to quantitate non-radiative plasmon decay pathways such as carrier-phonon and carrier-carrier scattering.[172] Advantages of EELS include avoidance of diffraction-limited excitation of multiple AuNPs and direct carrier excitation in the TMD.

Prior to this work, HET studies for AuNP-TMD interfaces has been limited to samples with physical contact, not those chemically bonded.[170,173] Measured EELS bandwidth decomposition from 80 nm Au nanospheres dropcast on exfoliated MoS$_2$ yielded a 6% quantum efficiency (η) for hot electron transfer, where η is the ratio of plasmonic hot electrons transferred to total hot electrons generated.[170] The remaining 94% decayed through scattering or thermalization. The same

approach estimated hot electron transfer from Au nanoellipses to graphene at η = 20%.[174] However, these studies and related work utilizing pump-probe spectroscopic methods[18,175] examined only NPs deposited onto the 2D material basal plane. Physiochemical contact with WS_2 at edge locations presents a new scenario where energy damping occurs at or near catalytically active edge sites.[176]

Measured EELS was supplemented with eDDA v1.2,[177] an electron excitation DDA package, to model various metal NP structures on 2D TMDs.[171] Both light and electron excitation implementations of the discrete dipole approximation (DDA) were used to differentiate radiative and non-radiative damping contributions to the LSPR. For eDDA simulations, a single 20 nm AuNP was placed adjacent to a 2D 45 x 90 nm WS_2 sheet generated with the method outlined in Section 4.4.2. These simplified dimensions were based on averages obtained from TEM images during EELS measurements on *in situ* reduced Au-WS_2 samples. Approximating reduced AuNPs as perfect 20 nm diameter spheres is not anticipated to appreciably affect results since this size AuNP is well within the quasistatic regime.

HET η from both measured EELS and simulated eDDA spectra were estimated at 14% over 6 fs based on a 0.23 eV LSPR bandwidth expansion.[171] Excellent agreement with eDDA was obtained under the assumption that accrued LSPR bandwidth increases resulted only from energy transfer between Au and WS_2. HET for chemically reduced AuNPs exceeded that for those deposited onto the TMD basal plane.[170] HET enhancement is likely attributable to direct physicochemical contact of AuNP on WS_2, edge AuNP locations, and lower NP-TMD Schottky barrier. More efficient HET from *in situ* reduced AuNPs on WS_2, promising for photocatalysis, is reasonable based on other related works. Enhanced HET could be anticipated from resonant AuNP excitation near WS_2 edge sites due to their intrinsically enhanced optical activity.[138] Inserting

dielectric layers between the NP and TMD was found to lower η of carrier injection by increasing ohmic resistance.[170]

4.4 Experimental & theoretical approaches

4.4.1 Liquid-phase exfoliation of 2D TMDs

Liquid-phase exfoliation (LPE) provides a low-cost, potentially scalable method of producing few layer TMDs.[131,133] Several distinct liquid exfoliation techniques are available, with the simplest being liquid-phase exfoliation (LPE), the method used herein. In a typical LPE process, layered crystals are sonicated in a stabilizing solution. Sonication breaks weak van der Waals bonds between layers, while interactions with surrounding liquid stabilize nanosheets against aggregation. Liquids used include solvents[178] and aqueous surfactant solutions,[179] with non-toxic surfactant-stabilized dispersions being particularly helpful to minimize aggregation in solution and following film deposition. Following sonication, a series of centrifugation protocols are utilized to separate nanosheets by size and thicknesses.[153] The resulting dispersions can be easily processed into films or inkjet printed onto substrates.[131] Continued development of lower cost, scalable techniques that engineer thinner or heterogeneous interfaces are important for implementation.

Liquid-exfoliated WS_2 was prepared as illustrated in Figure 19. Bulk WS_2 (Sigma Aldrich, St. Louis, MO, USA) powder was dispersed at a concentration of 25 mg/ml in aqueous sodium cholate surfactant solution (6 mg/ml). The mixture was sonicated in an ice-water bath at 360 W (60% amplitude) in a stainless steel beaker using a probe sonicator with a flat-head tip. Sonication was performed for 80 minutes with a 6 second on, 2 second off cycle. Following this initial sonication, the dispersion was centrifuged (Hettich Mikro 220R centrifuge, Tuttlingen, GER) for 1.5 hours at

4000 rpm (1700 g). The supernatant was removed, then discarded. The sediment was re-dispersed in 75 ml of fresh aqueous surfactant solution at a concentration of 3 mg/ml. This step is important to clean the bulk TMD powders, removing contaminants.
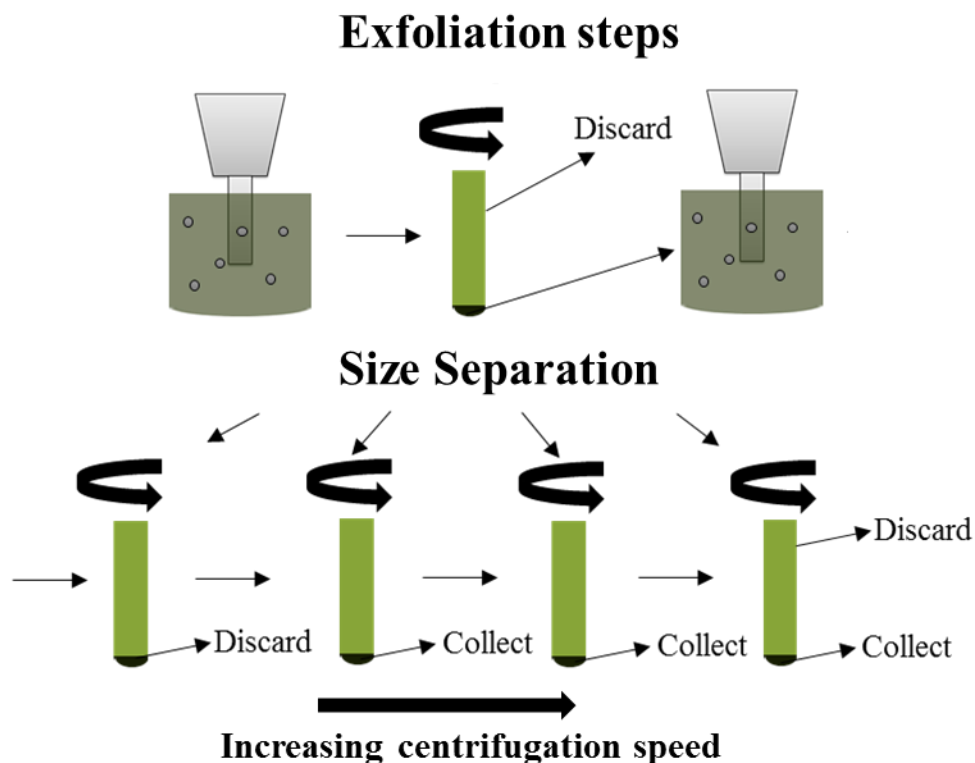
Figure 19: Schematic illustrating liquid-phase exfoliation of TMDs via sonication and subsequent size-selection of TMDs.

After the initial cleaning step, the TMD dispersions were sonicated for 8-12 hours at 360 W (60% amplitude) in a metal beaker using the same flat-head tip probe sonicator with a 6 second on/2 second off cycle. This long-term sonication breaks van der Waals forces in bulk crystals, producing significant quantities of mono and few layer TMDs. Longer sonication times yield more exfoliated nanosheets, but care must be taken to insure aggregation-inducing heat is mitigated with the ice-water bath. Following sonication, nanosheets are separated by size via centrifugation. This size separation was performed as reported previously via centrifugation at 15 °C with sequentially

increasing rotor speeds.[138,153] For speeds $\leq$ 6000 rpm (3500 g) a fixed angle rotor 1016 was used (ca. 10 mL volume, 28 mL vials). As an example of a centrifugation cascade, unexfoliated TMDs are removed at 1500 rpm (240 g) as sediment. Next, the 1500 rpm supernatant is centrifuged at 3000 rpm (960 g) and the sediment was discarded. Next, the procedure is followed at 4000 rpm. This time, the sediment is re-dispersed at reduced volume (ca. 5 ml) in fresh surfactant solution, as sample trapped at these speeds are largely comprised of relatively large, few layer l-WS$_2$ nanosheets. This procedure is repeated with increasing centrifuge speed until 10000 rpm (9700 g), where the supernatant is discarded. Nanosheets comprising this supernatant are mostly monolayer, but typically have such small lateral dimensions that they lose their characteristic optoelectronic properties. In general, flakes trapped at higher speeds are thinner and have smaller lateral dimensions.[138] The more intermediate cascade steps, the finer the subsequent size distributions. Production of highly monolayer enriched dispersions using a more stringent liquid cascade, yielding finer control over final nanosheet dimensions, was recently published.[153]

4.4.2 Discrete Dipole Approximation

This section outlines a key resource, the discrete dipole approximation (DDA), for studying the underlying electrodynamic interactions in NP-2D TMD nanostructures. Each nanostructure is treated as a collection of dipoles in DDA. The physical target dimensions are discretized with dipoles placed in a cubic lattice encompassing the nanostructure shape. Polarizability, α_i for each dipole comprising the target is calculated by the Lattice Dispersion Relation.[180] Polarization magnitude for each target sub-volume, P_i, in response to the local electric field, $E_{o,i}$, is given as

$$P_i = \alpha_i \left(E_{o,i} - \sum_{j \neq i}^{N} A_{ij} P_j \right) \qquad (4.2)$$

where $\sum_{j \neq i}^{N} A_{ij} P_j$ sums interaction between dipoles and A_{ij} is a more rigorous dipole-dipole interaction matrix analogous to the S matrix in CDA. Extinction cross-sections are then computed from total calculated P_i across all dipoles by

$$\sigma_{ext} = \frac{4\pi k}{|E_o|^2} \sum_{j=1}^{N} Im\left(E_{o,j} \cdot P_j \right) \qquad (4.3)$$

where k is the orthogonal incident wavevector and *Im* represents the imaginary component of the quantity. This DDA approach was implemented to calculate electromagnetic interactions for complex targets where an analytical α_i does not exist, such as Au-decorated WS_2 nanosheets. Greater accuracy is achieved with more dipoles (i.e., finer discretization), but computational requirements increase substantially. A combination of DDA and the coupled dipole approximation (CDA), which treats each NP as a single polarizable point dipole, is capable of reducing computational time 40,000-fold over full volume DDA models.[5,6] For example, interaction between dielectric substrates and transparent conductive oxides were studied recently using an extension of this multi-scale approach.[92]

DDSCAT, an open-source DDA software developed was used in this work.[37,73,91,181] Both near- and far-field optical response of arbitrary targets of a given shape and material are uniquely described with DDA. Local field enhancement factors are calculated using the Clausius-Mossotti relation.[91] Electron excitation induces resonances not observable with light excitation.[182] Recent extension of the DDA algorithm allowing electron excitation, eDDA, was developed.[177] These "dark" modes along with conventional bright modes are probed by selecting simulated electron

beam impact points analogous to those measured in EELS, which were at the edge of a 20 nm AuNP. DDA simulations from 420 nm to 820 nm wavelengths with 1 nm resolution were performed on a 16-core supercomputer node with 32 GB memory. WS_2 nanosheets and AuNPs were discretized in Cartesian coordinates. AuNP dielectric functions were Johnson and Christy,[183] while monolayer WS_2 was given from dielectric data obtained from CVD-grown WS_2.[167] A medium refractive index ($n = 1.33$) was used for comparison with those measured from aqueous dispersions.

Custom DDA target generation permitted creation of both idealized Au-WS_2 targets and more complex target geometries based on TEM images of fabricated samples. The desired heterostructure geometrical shapes were made in Blender (Blender Foundation, Amsterdam, NLD), a 3D graphics software. This target was then uploaded into the NanoHub tool DDSCAT Convert v. 2.0,[184] which takes various user inputs to develop a dipole discretized version of the desired shape. Idealized shape geometries, i.e. a thin rectangular WS_2 nanosheet and single spherical AuNP, were easily created and manipulated in Blender. A similar approach within the group probed the effect of substrate choice and NP shape on plasmonic and coupled resonant modes.[92] However, this approach did not allow for placement of AuNPs on WS_2 edge sites, which appears to be the location of a majority of the *in situ* reduced AuNPs. Beyond implementation of the dielectric function for monolayer WS_2 in the simulation,[167] the dipole-discretization treatment in DDA did not explicitly provide for a finite thickness for WS_2.

An extension of this approach allowed a realistic DDA target to be created based on real TEM images. Figure 20 shows the progression from a TEM image (Figure 20a) of an Au-decorated WS_2 nanosheet, to a discretized dipole target (Figure 20c). First, the image contrast is adjusted to maximize difference between WS_2 and the AuNPs. The outline of the visible WS_2 sheet is first

extracted. Then, a 2D projection of the AuNPs was placed over this nanosheet. At each AuNP location, a sphere matching the dimensions of that 2D projection are placed manually at each location (Figure 20b). The template is removed, leaving only the 2D sheet and 3D spheres representing AuNPs. This OBJECT (.obj) file is then converted into a DDA target, as shown in the right-hand image of Figure 20 using DDSCAT Convert v. 2.0.[184] This generalized approach to creating DDA targets could have important implications for more exotic shapes reduced on TMD, e.g. silver nanoprisms.[185]
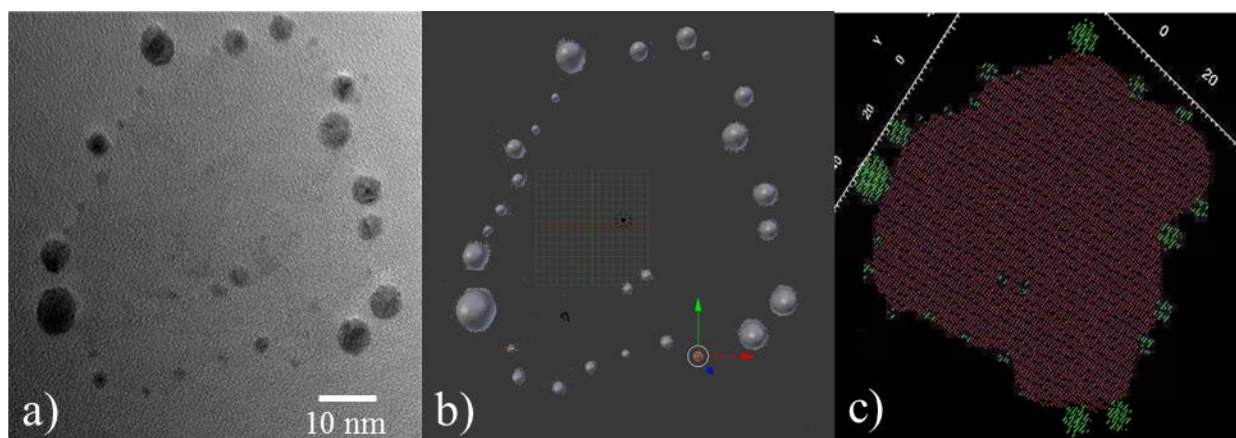
Figure 20: Progression from (a) TEM image to (b) AuNPs projected into 3D spheres to (c) dipole discretized DDA target containing WS_2 (red) and AuNPs (green).

4.4.3 Spectroscopic characterization techniques

UV-vis optical spectroscopy of aqueous dispersions of Au-WS$_2$ was performed with several different experimental setups. Spectrometers with UV capabilities, a Cary 5000 (Varian, Palo Alto, CA, USA) or a UV-1800 (Shimadzu, Kyoto, JPN) were needed for UV-vis size metrics evaluated at 235 nm.[153] Transmission and reflection spectra measured in an integrating sphere apparatus helped distinguish contributions from scattering and absorption to extinction. Aqueous dispersion of Au-WS$_2$ were placed in a home-built cuvette holder that centered the sample inside the

89

integrating sphere in a Lambda 650 (PerkinElmer, Waltham, MA, USA) spectrometer to estimate light absorption. Both transmitted light and scattered light exiting the cuvette obliquely are collected by the integrating sphere detector. Subsequently, conventional transmission spectra, giving total extinction, was performed outside the sphere apparatus. The difference between the extinction and absorption spectrum is the scattering spectrum. Time lapse extinction spectra as a function of time were performed using a home-built fiber coupled spectroscopic apparatus utilizing an AvaLight-DH-S-BAL white light source (Avantes Inc., CO, USA) and AvaSpec-2048 spectrometer (Avantes Inc., CO, USA).

PL and Raman spectroscopy were performed on Au-WS$_2$ aqueous dispersions with a LabRAM HR800 confocal microscope (Horiba, Kyoto, JPN) using 532 nm excitation laser (ca. 2 mW) in ambient conditions. The advantage of PL measurement in a Raman spectrometer is two-fold; it is convenient for study of both fluid and dried samples and the PL/Raman ratio gives insight into sample quality. PL/Raman emission was collected by a 100x objective lens (NA = 0.8). Sample focusing during acquisition is crucial to avoid error in extracted PL/Raman ratio used to normalize PL enhancements across samples. Evidence of out-of-plane measurements include a tilted emission baseline and apparent laser spot change in recorded optical images. For measurements, ~40 μL of dispersions were dropped on glass slides. A 10x objective was broadly focused on the drop, then the 100x objective was used to on the drop surface Focusing inside the drop can result in reabsorption of WS$_2$ PL, thereby lowering detected intensity. An average of 3-5 measurements per sample are plotted in section 4.2.1.

5. PROSPECTIVE APPLICATIONS

The two material platforms developed in this work, featuring highly absorptive plasmonic gold nanoparticles (AuNPs), could facilitate photon conversion into thermal or electronic energy for the benefit of multiple applications. Efficient, highly localized plasmonic thermal damping could offer new paradigms for adaptive control of thermoplasmonics for use in biotherapeutics, drug delivery, tumor ablation, and nanofluids for heat rejection.[186,187] Hot electron transfer (HET) from metal nanoparticles to adjacent 2D semiconductors[16] shows promise as a source of carriers in photocatalytic devices[17] and field-effect transistors.[18] Specifically, these emerging plasmon-mediated hybrid nanomaterials could permit exchange of optical, thermal, and electronic energy precisely where they are needed, e.g. at a chemical vaporization interface or catalytic active site. Development of new materials herein that exhibit emerging energetic decay pathways and compact, multi-scale descriptions of interrelated optical, electronic, and thermal effects could aid future system design and implementation.

5.1 AuNP-PDMS membranes in plasmonic pervaporation

Plasmonic NPs dispersed in three-dimensional films polymers have broad application in photovoltaics,[19,188] sensing,[44,189] optoelectronics,[20,21] and catalysis.[190] Polydimethylsiloxane (PDMS) containing AuNPs (AuNP-PDMS) in particular have garnered interest in mechanical strain sensing,[189] biosensing,[23] transistors,[191] microfluidics,[45] and chemical separations.[22] Description of interrelated optical and thermal effects in AuNP-polymer dispersions has progressed beyond conventional continuum heat transfer, Mie theory,[47] Beer-Lambert law,[50] or effective medium approximations.[81,82] Enhanced light trapping by internal reflection could benefit

waveguides in thin film photovoltaics,[57] fluorescence in quantum dot nanocomposites,[58] and high refractive-index polymers.[59] However, the primary focus herein was utilization of plasmonic heating in AuNP-PDMS membranes as the thermodynamic driving force for solvent flux in a lab-scale pervaporation system.

Conservative estimates suggest distillation, the most prolific method of component separations in the chemical industry, accounts for about 5% of energy consumption in the United States.[192] Beyond energy consumption required to boil components, azeotropes formed in distillation can limit separation ability. Membrane separation processes, such as pervaporation, have seen widespread use as a lower energy, thermodynamically favorable alternative for water treatment and biofuel production.[193] However, membrane processes often still require heating to increase mass transfer across the membrane.[194] In pervaporation, the thermodynamic driving force is the component partial pressure difference between liquid feed and vapor permeate at vacuum pressure.[195] Development of next-generation membrane materials with lower operating costs could offer a new paradigm for efficient chemical separations.

Nanotechnology is becoming increasingly important in the development of membrane technology for chemical purification.[2] In particular, the scalability and localized heating capabilities of AuNP-PDMS films show significant potential in the plasmonic pervaporation system.[14] Highly localized plasmonic heating within AuNP-PDMS membrane has the potential to dramatically enhance flux across the membrane, while lowering energy requirements.[196] Efficient radiative-enhanced light trapping and enhanced thermal dissipation in AuNP-PDMS films, as discussed in Chapters 2 and 3, could improve energy efficiency of pervaporation by providing energy at the vaporization interface, without the need to heat the entire feed solution.[22]

Previous work within the group pioneered investigation of *in situ* reduction of AuNPs in PDMS for use in the lab-scale pervaporation system.[14] Novel AuNP-PDMS membranes containing uniform dispersion of *in situ* reduced AuNPs were fabricated and tested at various laser powers. Thermalization following resonant excitation resulted in butanol fluxes up to 2-fold above Au-free analogues. A coupled solution-diffusion and energy balance helped identify potential energy and utility cost savings possible with plasmonic pervaporation. It was determined that the process required more energy and capital due to inefficient plasmonic absorption, but could offer up to a 7-fold reduction in energy requirements with membrane optimization and reduction of energy losses into the feed.

This work improved membrane fabrication and understanding of underlying plasmon-induced heating capabilities to support long-term goals of reducing pervaporation energy requirements. Furthermore, several system upgrades improving laser uniformity, thermal imaging capabilities, gasket seals, and support mesh materials were implemented to improve the lab-scale setup. Asymmetric reduced (r)AuNP-PDMS membranes, discussed in Section 3.3, provide superior optothermal and physical characteristics, but at the expense of readily definable NP distributions. Second-generation PDMS films containing definable AuNP distributions showed enhanced solvent flux upon addition of AuNPs in PDMS, but anomalous heating effects in the presence of water at elevated excitation powers precluded precise characterization of achievable flux enhancements. Taken together, these studies are important step towards realization of plasmon-active membrane separators.

5.1.1 Advantages of asymmetric AuNP-PDMS membranes in pervaporation

Promising thermal and physical properties of asymmetric rAuNP-PDMS films show significant potential for use as pervaporation membranes.[22] Efficient optoplasmonic conversion to heat is arguably the most important aspect of these thin films as separation membranes. Since the thermodynamic driving force in pervaporation is the difference in partial pressure between the feed and permeate sides of the membrane, increasing the membrane temperature should increase this driving force. The asymmetry of the thin films is desired since the effect of the AuNPs on the mass transport properties of PDMS remains largely uncharacterized. Placing the Au-free PDMS layer in contact with the pervaporation feed side and making the AuNP-containing layer as thin as possible should result in transport characteristics and performance analogous to Au-free PDMS, a commonly-used dense membrane.

Morphological, optical, and thermal characteristics of asymmetric rAuNP-PDMS thin films distinguished in this work suggest that the AuNP-containing layer thickness can be reduced by factors of ten or more relative to prior work.[22] Since pervaporation flux is inversely proportional to membrane thickness, scalability and control of the diffusive Au layer is an important step. Diffusive reduction of Au into partially cured PDMS appeared superior to either reduction into fully cured PDMS or laminar formation of asymmetric Au-PDMS thin films. A thinner Au layer was produced quickly with a wide range of attainable optical and physical properties. The diffusive method produced AuNP-containing layers 3-7 times thinner than the laminar method. Furthermore, significant improvements to Au layer thickness and optothermal conversion are not anticipated for the laminar method. The practical limit to spin-coating PDMS is about 15 μm, and this was possible only when using high toluene dilutions, which further complicates characterization of the thin films and could affect structural integrity.[197]

Heating capability of the asymmetric, diffusion-reduced 0.05 mass-percent AuNP-PDMS film, 3000 W/°C, was 3-fold greater than PDMS with uniform AuNP distribution, 11-fold higher than thermally annealed AuNPs on glass, and 230-fold higher than liquid AuNP dispersions.[22] The 0.5 mass-percent asymmetric AuNP-PDMS film reached 54.5°C above ambient temperature, while the 0.05 mass-percent, 0.005 mass-percent, and Au-free PDMS films reached 29.9 °C, 8.2 °C, and 0.7 °C above ambient conditions, respectively, at 18 mW irradiation. Enhanced photothermal response relative to previous aqueous, silica, and PDMS samples likely resulted from increased NP density, dispersion in insulating PDMS, and reduced radiative emission relative to two-dimensional samples.[22] In contrast, significant improvements in heating ability via the laminar method is not anticipated since the 1.2 mass-percent TCA used in the AuNP-containing layer was at the allowable limit for proper PDMS crosslinking.

The key limitations in study of potential pervaporation enhancements using asymmetric rAuNP-PDMS films were difficulties in both controlling and characterizing AuNP concentration, size, and morphologies of rAuNPs in PDMS. Controlling the reductive process inside the curing PDMS remains problematic. Microscopic evidence of small AuNPs, irregular networks, Au aggregates, and cratering on the film surface were individually observed at different Au solution concentration using the diffusive-reduction method.[22] Furthermore, electron microscopy of rAuNPs within insulative polymers is nearly impossible, prohibiting accurate characterization of resulting AuNP size, shape, and concentration. Due to these limitations, the asymmetric rAuNP-PDMS thin films were not evaluated directly as membranes in the lab scale pervaporation system.

5.1.2 Water pervaporation with second-generation AuNP-PDMS membranes

Second-generation AuNP-PDMS films containing readily definable dispersions of 16 nm solution-synthesized AuNPs were the focus of subsequent testing within the lab-scale pervaporation system. Second-generation AuNP-PDMS films were fabricated using the same approach as discussed in Section 2.4.1, except the uncured AuNP-PDMS mixture was spincoated at 500 rpm for 1 min. This formed membranes approximately 60 µm thick, ideal for maximizing solvent flux and giving adequate mechanical support. An up to 1.5-fold improvement in optical extinction per AuNP and improved thermal dissipation in these AuNP-PDMS films at ca. 20-fold greater thicknesses were highlighted in Section 2.2 and 3.2, respectively.

Measured steady-state average water flux through the 1.76×10^{12} NPs/cm^3 AuNP-PDMS thin film membrane increased up to 1.2-fold relative to Au-free PDMS at 750 mW. This fell well short of the 2-fold enhancements observed prior using rAuNP-PDMS membranes.[14] While flux through AuNP-PDMS did increase from 0.037 to 0.043 kg/m^{2}hr relative to Au-free PDMS at 750 mW, flux values at 250 and 500 mW for each membrane were nearly identical. Flux enhancements appeared limited by apparent anomalous thermal effects in the presence of water. Average membrane temperature increase (ΔT) at each AuNP concentration converged as incident laser power increased to 750 mW; ΔT was 45% higher for 1.76×10^{12} NPs/cm^3 film relative to Au-free PDMS at 250 mW, but was only about 5 and 2% higher at 500 and 750 mW, respectively.

Optical and thermal characteristics of the stainless steel mesh support contributed in part to the unexpected convergence of membrane temperature at higher laser powers. The stainless steel mesh is highly conductive, so it effectively acted as a heat sink for thermal dissipation away from the thin AuNP-PDMS membrane. Furthermore, the stainless steel mesh attenuated almost 40% of incident light. This characteristic attenuation, while likely comprising mostly of reflection, not

absorption, could nonetheless dominate macroscale optical response compared to the AuNP-PDMS membranes. These potential mitigating factors were alleviated by selection of an insulative, highly transparent ethylene tetrafluoroethylene (ETFE) support mesh. While this ETFE support mesh represents an important system improvement, the convergence of membrane ΔT regardless of AuNP concentration at high laser powers was not fully resolved.
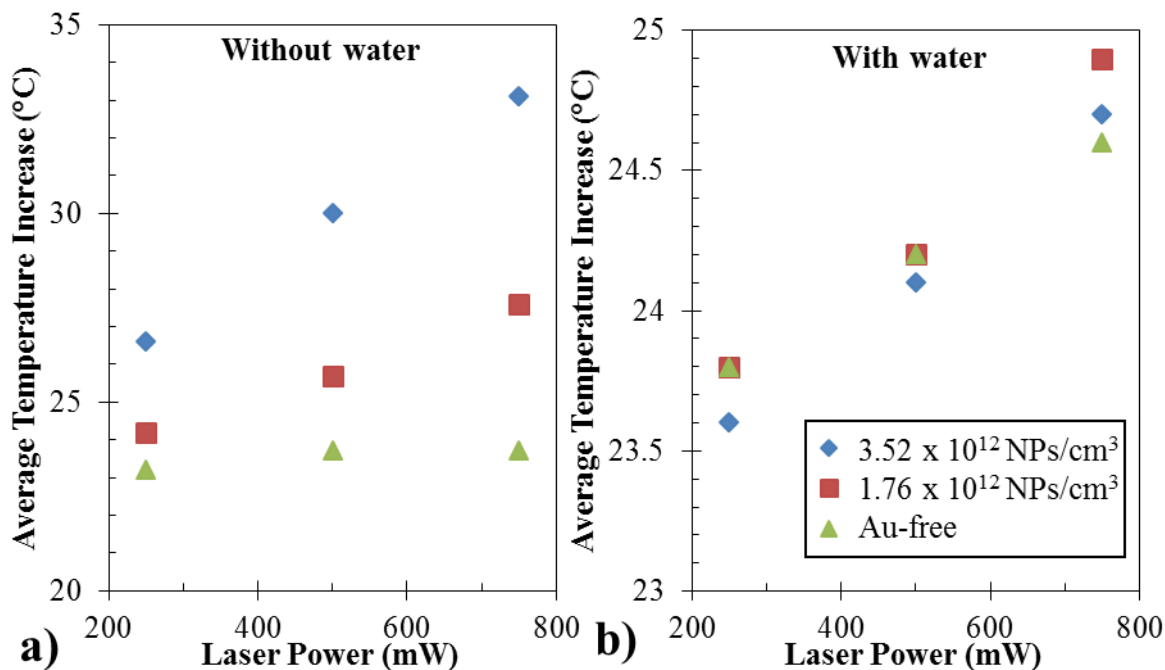
Figure 21: Average AuNP-PDMS membrane temperature increase a) without and b) with pervaporation cell feed water.

Decreasing ΔT between membranes was not anticipated from either optical attenuation or independent thermal characterization of ca. 60 µm AuNP-PDMS membranes absent adjacent feed water. For example, optical attenuation, measured using the integrating sphere apparatus described in Section 2.4.4, showed a linear increase in resonant attenuation per NP. Attenuation percentage above Au-free PDMS rose from ca. 1% at 0.469×10^{12} NPs/cm^3 to 3.5% at 1.76×10^{12} NPs/cm^3. Average membrane temperature increases with the adjacent ETFE mesh absent feed water

matched expected trends based on optical attenuation; measured ΔT in Figure 21a shows dependence on both AuNP concentration and incident laser power. However, ΔT increases only slightly with increasing laser power upon addition of feed water and exhibits no apparent dependence on AuNP concentration across the range of powers and concentrations examined.

The residual hydrophilic PVP (polyvinylpyrrolidone) coating on the AuNPs dispersed in PDMS is another possible culprit to limited heating enhancements observed within the system. While the PVP coating is necessary to minimize AuNP aggregation and solvent compatibility in uncured PDMS,[30] interaction with water molecules within the PDMS may disrupt thermoplasmonic dissipation. Water likely preferentially migrates towards the residual hydrophilic PVP left over from the isopropanol AuNP dispersion mixed into PDMS. Pockets of liquid water, or even vapor near irradiated AuNPs could create efficient scattering centers and inhibit plasmonic absorption. Preliminary optical transmission experiments in the presence of water did not yield increased transmission that would be anticipated if plasmonic absorption was dampened in the absence of other attenuating effects. Therefore, it appears possible anomalous scattering may contribute to suppressed plasmonic absorption and resulting thermal response. After consideration of these results and concurrent advancements within the group, it was determined the most prudent future step was focused development of PDMS membranes featuring ordered AuNP arrays, as discussed in Chapter 6.

5.1.3 Experimental setup

A schematic of the upgraded pervaporation system is given in Figure 22.[14] The membrane separator apparatus consists of feed and permeate tubes, membrane assembly, and two graduated pipettes used to measure component flux. The membrane assembly features the fused AuNP-

PDMS membrane and gasket along with the fused support ETFE (Ted Pella, Inc., Redding, CA, USA) mesh and gasket. Localized plasmonic excitation was supplied by a 532 nm diode laser (MXL-H-532, CNI, Changchun, China) whose power can be varied from 0-1 W using neutral density filtration. A diffuser and converging lens (Thorlabs, Newton, NJ, USA) were added to the laser to help ensure a uniform laser beam and subsequent heated membrane temperature. Laser power was measured with a power meter (PM310D, Thorlabs, Newton, NJ, USA) before and after each run to ensure the laser power did not vary significant over large periods of time. The feed temperature was recorded continuously with two thermocouples at various locations along the feed tube to characterize thermal losses into the feed.
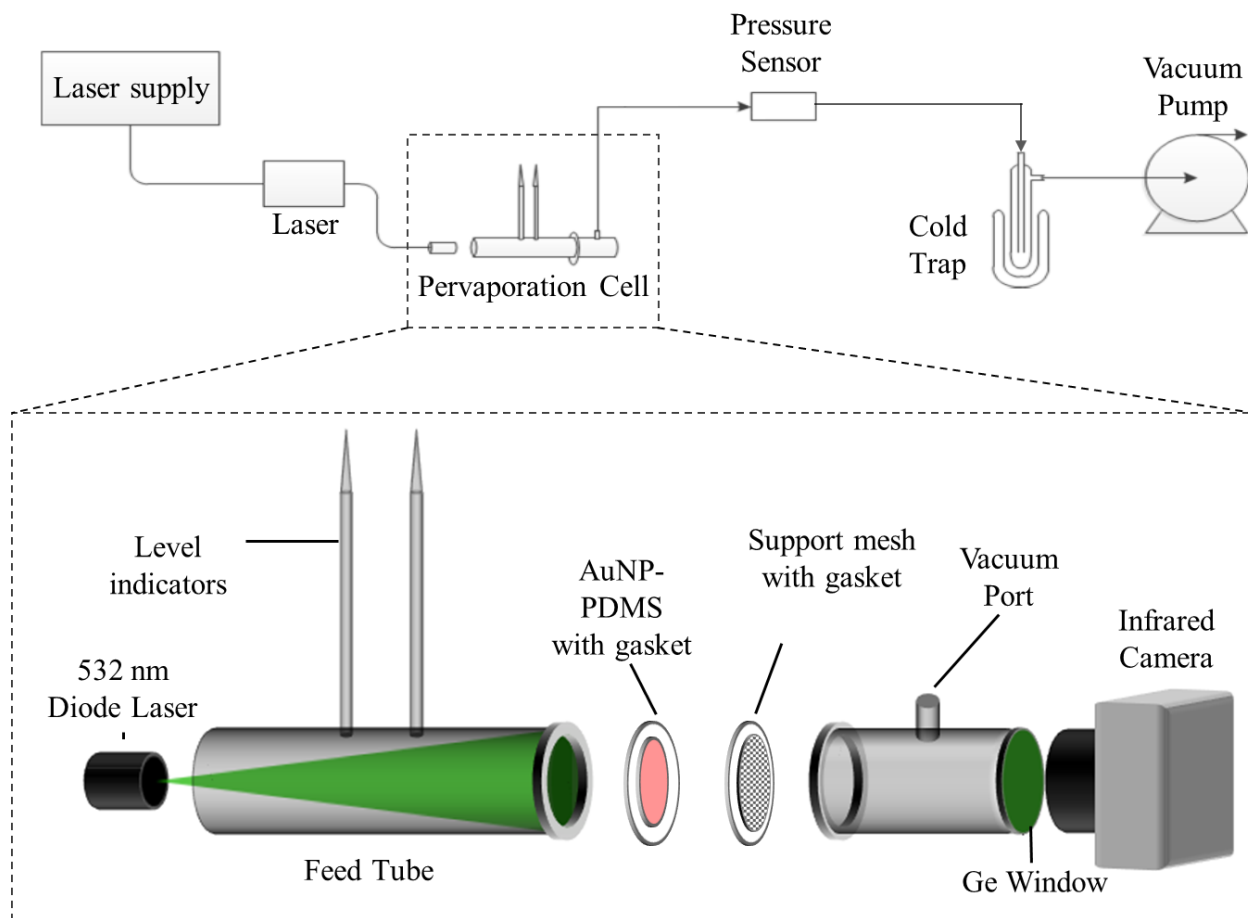

Figure 22: Schematic of lab-scale plasmonic pervaporation system.[14]

The temperature of the membrane surface was measured with an infrared (IR) camera (ICI 7320 P-Series, Infrared Cameras Inc., Beaumont, TX, USA). A germanium window transparent in the IR regime capped the permeate tube to allow accurate thermal measurements. Typical of pervaporation setups, a vacuum pump (DV-4E, JB Industries Inc., Aurora, IL, USA) and cold trap, consisting of IPA and dry ice, condensed and captured permeate. The vacuum pressure was kept constant throughout the experiment; measurements were recorded continuously with an absolute capacitance manometer (722B-100, MKS Instruments, Andover, MA, USA), a data acquisition card, and LabVIEW Signal Express (National Instruments, Austin, TX, USA).[14] The cell was enclosed in a plexiglass container in order to minimize forced convection.

The procedure for running a single pervaporation trial are as follows.[14] First, feed and flux level indicators were filled with distilled water. The flux level indicators were filled near the highest visible graduation to ensure complete flux measurement over long trials. Automated data recording systems for pressure, ambient and feed temperatures, membrane temperature, and flux were implemented. Feed volume changes were captured every 20 minutes with a webcam. To begin data collection, the vacuum pump was started and flux tubes were covered with parafilm to minimize evaporative losses. The system, absent laser excitation, was given two hours to reach steady-state operation. Before beginning the dynamic heating, membrane temperature data from the infrared camera was saved, the capture rate increased from 0.02 to 1 Hz, and then restarted. This was done to study the dynamic portion immediately following resonant laser excitation of AuNPs in PDMS in finer detail. This dynamic period with faster thermal capture rates lasted for 20 minutes, sufficient time for the membrane to reach thermal equilibrium. Following the dynamic portion, the thermal capture rate was lowered back to 0.02 Hz and the system ran uninterrupted for

14-24 hours. The fused membrane and mesh gasket supports allowed continuous operation for 24+ hours without loss in vacuum pressure, an improvement over the initial setup.

Flux calculations were performed using a MATLAB script that counts the number of pixels the water level dropped since the previous snapshot.[14] Small Styrofoam beads were used to improve water level visibility in recorded images. A conversion factor (a) of 480 pixels/mL was determined based on pixel resolution and physical dimensions, giving volume flux for each time interval. Mass flux was calculated as $J = a\rho\Delta p/A\Delta t$, where J is the pure water flux in kg, a is the pixel to volume conversion factor, ρ is density of water, A is the active membrane area (1.8×10^{-4} m^2), and Δt is the 10 minute time period between each measurement. Volume of recovered permeate was recorded for comparison with flux indicator values. A separate MATLAB script allowed facile analysis of membrane temperature distributions across all captured images. Membrane ΔT was given as the average ΔT for each trial across the entire steady-state laser excitation period.

5.2 Plasmon-enhanced Au-WS$_2$ nanosheets

Semiconducting 2D-TMDs provide a novel platform to explore plasmonic excitation and dissipation pathways with broad application in optoelectronics,[121,122] sensing,[123,124] photodetection,[125] and solar fuel production.[126] Au-decoration of WS$_2$, discussed in Section 4.1, exerted a measure of control over physical and optoelectronic properties. AuCl$_3$ preferentially reduces on multi-layer nanosheets; aggregates formed at higher Au content are easily removed via centrifugation, thereby leaving mostly monolayer Au-WS$_2$ nanosheets behind. These Au-WS$_2$ heterostructures exhibited enhanced broadband carrier generation and exciton damping, i.e., optical extinction and photolumsinescence (PL), relative to Au-free WS$_2$ analogues.

HET in developed Au-WS$_2$ heterostructures, with an estimated quantum efficiency of 14% based on measured and theoretical results, could drive photocatalytic reactions or generate photocurrent even at sub-bandgap, infrared energies. Energetic electron injection into physisorbed species and facilitation of high-energy reactions with hot carriers is promising. These high energy electrons from plasmonic NPs can dissociate hydrogen on metal NPs,[17] while improved photocatalytic hydrogen evolution reaction (HER) has been demonstrated with Au-decorated 2D TMDs.[198] HET from plasmonic NPs can even induce a 2H to 1T crystal phase transition in TMDs,[199] which increases conductivity and suppresses PL.[200] Concurrently, intense plasmon near-fields from adjacent NPs could improve intrinsic light absorption and carrier separation in adjacent semiconducting TMDs. These localized fields could also facilitate energy exchange between different frequencies for infrared energy harvesting[201] by increasing harmonic photon upconversion in monolayer WS$_2$, which exhibits an already strong intrinsic SHG response.[202] Overall, improvements in monolayer production and optoelectronic tunability resulting from *in situ* Au-decoration represents an important advance in the future study of NP-TMD heterostructures for use across a diverse range of applications.

6. CONCLUSIONS

6.1 Summary

This work advanced several key elements of photon dissipation into thermal or electronic energy in systems containing small, highly absorptive plasmonic AuNPs. Diffraction-induced optical extinction enhancements in random AuNP dispersions in 3D polymer films at interparticle separations near the resonant wavelength was reported for the first time. Complementary approaches developed in Chapter 2 distinguished contributions to optical extinction from isolated particles, interparticle interactions, and dielectric heterogeneity. Thermal dissipation following plasmonic absorption in these 3D polymer dispersions was extensively characterized in Chapter 3. Excellent agreement was obtained between measured and theoretical results that extended beyond conventional optical and one-dimensional heat transfer descriptions. These findings support robust design of resonant thermoplasmonics in emerging flexible photonic systems. In particular, Chapter 5 discusses how these AuNP-polymer films could reduce thermodynamic requirements in pervaporation for efficient chemical separations.

Concurrently, *in situ* reduction of plasmonic AuNPs on 2D WS_2 addressed two current material limitations of these emerging nanoscale semiconductors. Addition of plasmonic AuNPs yielded higher obtainable monolayer content and modified optoelectronic response following liquid exfoliation of bulk WS_2. Improved monolayer content, broadband optical extinction, and energetic electron injection were probed in Chapter 4 using a combination of advanced spectroscopic techniques and continuum electromagnetic description. Several optoelectronic and light harvesting applications were considered in Chapter 5 for the small Au-decorated WS_2 nanosheets developed herein, with use their possible use as photocatalysts considered particularly promising.[203]

6.2 Future Work

The idea of incorporating plasmon-active nanostructures into membrane separations is proliferating rapidly.[196] The natural progression of work described in Section 5.1 involves the incorporation of an ordered AuNP array into a thin polyethylene oxide (PEO)-PDMS film. Addition of PEO co-polymer improves hydrophilicity[204] and is therefore expected to enhance water pervaporation flux. In contrast to randomly dispersed NPs, emerging ordered arrays of plasmonic nanostructures allow for highly tunable, localized optical responses.[5,205] These diffractive coupled lattice resonances could permit order-of-magnitude improvement in pervaporation performance. Work is underway to develop fabrication methods to create these next-generation AuNP-PDMS membranes. Future study of these more advanced ordered AuNP systems are supported by the optothermal characterization and theoretical expertise developed herein.

To-date, little is known about the redox potentials of TMDs or the mechanism for sponteneous Au-decoration. Understanding redox conditions could faciliate more rapid progress towards decoration of more exotic nanostructure materials and shapes featuring tunable plasmon resonances.[185] A continous flow system previously developed within the group allows precise control over mass transfer-mediated reaction kinetics for electroless Au plating.[206] This system has been adapted for decoration of TMDs deposited onto planar substrates to provide more control over Au-reduction compared to batch reaction. It is anticipated Au-decoration of TMDs deposited on planar substrates would interface well with catalytic hydrogen evolution reaction (HER) testing.

Enhanced catalytic HER activity from Au-decorated, liquid-exfoliated nanosheets is viewed as a particularly promising application.[147] Small WS_2 nanosheets produced via liquid exfoliation are ideal since catalytic sites are believed to be dangling sulfur (S) bonds located primarily at edge or defect sites.[207] Electrochemical studies performed by collaborators suggest Au-decoration

enhances HER up to 5-fold in the absence of light-driven plasmonic effects.[152] Improved charge transport, a major limiting factor in utilization of liquid-exfoliated nanosheets[208] and modified edge chemistry are potential reasons for observed enhancement. It is proposed that as Au is preferentially reduced at edge S sites, abundant edge thiols are preferentially reduced to more catalytically active disulfides.[152]

These promising electrochemical results for Au-decorated WS_2 warrant further study of their potential as photocatalysts. Current materials used are plagued by incomplete absorption of broadband solar radiation and difficulty controlling generated carriers. Accurate description herein of local field enhancements and HET in these hybrid nanomaterials under light excitation is an important first step towards characterizing their full potential as photocatalysts. Intense plasmon local near-fields could enhance light absorption and carrier separation in adjacent 2D TMDs. Concomitantly, carrier injection from AuNPs on WS_2 could catalyze chemical reactions at sub-bandgap, infrared energies and facilitate high energy reactions with physisorbed species. Refinement of Au-WS_2 electrode deposition and photoelectrochemical measurement techniques are the subject of ongoing work in collaboration with researchers at both the University of Arkansas and Heidelberg University.

NOMENCLATURE

AFM	Atomic Force Microscopy
AuNP	Gold Nanoparticle
AuNP-PDMS	Gold Nanoparticle-Polydimethylsiloxane
AuNP-PVP	Gold Nanoparticle-Polyvinylpyrrolidone
Au-WS$_2$	Gold Decorated Tungsten Disulfide
CDA	Coupled Dipole Approximation
CVD	Chemical Vapor Deposition
DDA	Discrete Dipole Approximation
EELS	Electron Energy Loss Spectroscopy
EMT	Effective Medium Theory
FEA	Finite Element Analysis
HER	Hydrogen Evolution Reaction
HET	Hot Electron Transfer
IPA	Isopropanol
LPE	Liquid-phase Exfoliation
LSPR	Localized Surface Plasmon Resonance
MoS$_2$	Molybdenum Disulfide
PDMS	Polydimethylsiloxane
PL	Photoluminescence
PVP	Polyvinylpyrrolidone
rAuNP	Reduced Gold Nanoparticle

ROI	Region of Interest
RI	Refractive Index
$r_{w\text{-}s}$	Wigner-Seitz Radius
SEM	Scanning Electron Microscopy
SHG	Second Harmonic Generation
STEM	Scanning Transmission Electron Microscopy
TCA	Gold (III) Chloride
TEM	Transmission Electron Microscopy
TMD	Transition Metal Dichalcogenide
UV-vis	Ultraviolet-visible
WS_2	Tungsten Disulfide
XPS	X-Ray Photoelectron Spectroscopy
1D	One-dimensional
2D	Two-dimensional
3D	Three-dimensional

REFERENCES

1)   International Food Policy Research Institute, *Sustaining Growth via Water Productivity: 2030/2050 Scenarios*; 2011.

(2)   Pendergast, M. M.; Hoek, E. M. V. A Review of Water Treatment Membrane Nanotechnologies. *Energy Environ. Sci.* **2011**, *4*, 1946.

(3)   International Energy Agency. *World Energy Outlook 2013*; Paris, France, 2013.

(4)   Boltasseva, A.; Atwater, H. A. Low-Loss Plasmonic Metamaterials. *Science.* **2011**, *331*, 290–291.

(5)   Forcherio, G. T.; Blake, P.; DeJarnette, D.; Roper, D. K. Nanoring Structure, Spacing, and Local Dielectric Sensitivity for Plasmonic Resonances in Fano Resonant Square Lattices. *Opt. Express* **2014**, *22*, 17791.

(6)   DeJarnette, D.; Blake, P.; Forcherio, G. T.; Keith Roper, D. Far-Field Fano Resonance in Nanoring Lattices Modeled from Extracted, Point Dipole Polarizability. *J. Appl. Phys.* **2014**, *115*, 24306.

(7)   Park, J. H.; Von Maltzahn, G.; Ong, L. L.; Centrone, A.; Hatton, T. A.; Ruoslahti, E.; Bhatia, S. N.; Sailor, M. J. Cooperative Nanoparticles for Tumor Detection and Photothermally Triggered Drug Delivery. *Adv. Mater.* **2010**, *22*, 880–885.

(8)   Kang, B.; Afifi, M. M.; Austin, L. A.; El-Sayed, M. A. Exploiting the Nanoparticle Plasmon Effect: Observing Drug Delivery Dynamics in Single Cells via Raman/fluorescence Imaging Spectroscopy. *ACS Nano* **2013**, *7*, 7420–7427.

(9)   Zhang, J. Z. Biomedical Applications of Shape-Controlled Plasmonic Nanostructures: A Case Study of Hollow Gold Nanospheres for Photothermal Ablation Therapy of Cancer. *J. Phys. Chem. Lett.* **2010**, *1*, 686–695.

(10)   Xu, Y.; Heberlein, W. E.; Mahmood, M.; Orza, A. I.; Karmakar, A.; Mustafa, T.; Biris, A. R.; Casciano, D.; Biris, A. S. Progress in Materials for Thermal Ablation of Cancer Cells. *J. Mater. Chem.* **2012**, *22*, 20128.

(11)   Wang, C.; Ranasingha, O.; Natesakhawat, S.; Ohodnicki, P. R.; Andio, M.; Lewis, J. P.; Matranga, C. Visible Light Plasmonic Heating of Au-ZnO for the Catalytic Reduction of CO_2. *Nanoscale* **2013**, *5*, 6968–6974.

(12)   Hallett-Tapley, G. L.; Silvero, M. J.; Bueno-Alejo, C. J.; González-Béjar, M.; McTiernan, C. D.; Grenier, M.; Netto-Ferreira, J. C.; Scaiano, J. C. Supported Gold Nanoparticles as Efficient Catalysts in the Solventless Plasmon Mediated Oxidation of Sec-Phenethyl and Benzyl Alcohol. *J. Phys. Chem. C* **2013**, *117*, 12279–12288.

(13)   Vanherck, K.; Hermans, S.; Verbiest, T.; Vankelecom, I. Using the Photothermal Effect to Improve Membrane Separations via Localized Heating. *J. Mater. Chem.* **2011**, *21*, 6079–6087.

(14)   Russell, A. Plasmonic Pervaporation via Gold Nanoparticle-Functionalized Nanocomposite Membranes, Ph.D Dissertation, University of Arkansas, 2012.

(15)   Li, Y.; Verbiest, T.; Vankelecom, I. Improving the Flux of PDMS Membranes via Localized Heating through Incorporation of Gold Nanoparticles. *J. Memb. Sci.* **2013**, *428*, 63–69.

(16)   Clavero, C. Plasmon-Induced Hot-Electron Generation at Nanoparticle/metal-Oxide Interfaces for Photovoltaic and Photocatalytic Devices. *Nat. Photonics* **2014**, *8*, 95–103.

(17)   Mukherjee, S.; Libisch, F.; Large, N.; Neumann, O.; Brown, L. V.; Cheng, J.; Lassiter, J. B.; Carter, E. A.; Nordlander, P.; Halas, N. J. Hot Electrons Do the Impossible: Plasmon-Induced Dissociation of H_2 on Au. *Nano Lett.* **2013**, *13*, 240–247.

(18)   Lin, J.; Li, H.; Zhang, H.; Chen, W. Plasmonic Enhancement of Photocurrent in MoS_2 Field-Effect-Transistor. *Appl. Phys. Lett.* **2013**, *102*, 2013–2016.

(19)   Xie, F.-X.; Choy, W. C. H.; Wang, C. C. D.; Sha, W. E. I.; Fung, D. D. S. Improving the Efficiency of Polymer Solar Cells by Incorporating Gold Nanoparticles into All Polymer Layers. *Appl. Phys. Lett.* **2011**, *99*, 153304.

(20)   Noh, Y.; Zhao, N. I.; Caironi, M.; Sirringhaus, H. Downscaling of Self-Aligned, All-Printed Polymer Thin-Film Transistors. *Nat. Nanotechnol.* **2007**, *2*, 784–789.

(21)   Hung, Y. C.; Lin, T. Y.; Hsu, W. T.; Chiu, Y. W.; Wang, Y. S.; Fruk, L. Functional DNA Biopolymers and Nanocomposite for Optoelectronic Applications. *Opt. Mater.* **2012**, *34*, 1208–1213.

(22)   Dunklin, J. R.; Forcherio, G. T.; Berry, K. R.; Roper, D. K. Asymmetric Reduction of Gold Nanoparticles into Thermoplasmonic Polydimethylsiloxane Thin Films. *ACS Appl. Mater. Interfaces* **2013**, *5*, 8457–8466.

(23)   SadAbadi, H.; Badilescu, S.; Packirisamy, M.; Wuthrich, R. Integration of Gold Nanoparticles in PDMS Microfluidics for Lab-on-a-Chip Plasmonic Biosensing of Growth Hormones. *Biosens. Bioelectron.* **2013**, *44*, 77–84.

(24)   Venditti, I.; Fratoddi, I.; Russo, M. V.; Bearzotti, A. A Nanostructured Composite Based on Polyaniline and Gold Nanoparticles: Synthesis and Gas Sensing Properties. *Nanotechnology* **2013**, *24*, 155503.

(25)   Jain, P. K.; Lee, K. S.; El-Sayed, I. H.; El-Sayed, M. A. Calculated Absorption and Scattering Properties of Gold Nanoparticles of Different Size, Shape, and Composition: Applications in Biological Imaging and Biomedicine. *J. Phys. Chem. B* **2006**, *110*, 7238–7248.

(26)   DeJarnette, D.; Roper, D.; Harbin, B. Geometric Effects on Far-Field Coupling between Multipoles of Nanoparticles in Square Arrays. *J. Opt. Soc. Am. B* **2012**, *29*, 88.

(27)   DeJarnette, D.; Norman, J.; Roper, D. K. Attribution of Fano Resonant Features to Plasmonic Particle Size, Lattice Constant, and Dielectric Wavenumber in Square Nanoparticle Lattices. *Photonics Res.* **2014**, *2*, 15.

(28)   Blake, P.; Kühne, S.; Forcherio, G. T.; Roper, D. K. Diffraction in Nanoparticle Lattices Increases Sensitivity of Localized Surface Plasmon Resonance to Refractive Index Changes. *J. Nanophotonics* **2014**, *8*, 83084.

(29)   Dunklin, J. R.; Forcherio, G. T.; Berry, K. R.; Roper, D. K. Gold Nanoparticle-Polydimethylsiloxane Thin Films Enhance Thermoplasmonic Dissipation by Internal Reflection. *J. Phys. Chem. C* **2014**, *118*, 7523–7531.

(30)   Dunklin, J. R.; Forcherio, G. T.; Keith Roper, D. Gold Nanoparticle-Polydimethylsiloxane Films Reflect Light Internally by Optical Diffraction and Mie Scattering. *Mater. Res. Express* **2015**, *2*, 85005.

(31)   Bohren, C.F. D; Huffman, D.R. *Absorption and Scattering of Light by Small Particles*; Wiley: Hoboken, NJ, 1998; Vol. 31.

(32)   Ishimaru, A. *Wave Propagation and Scattering in Random Media*; Wiley: Hoboken, NJ, 1978; Vol. 8, No. 4.

(33)   Bright, R. M.; Musick, M. D.; Natan, M. J. Preparation and Characterization of Ag Colloid Monolayers. *Langmuir* **1998**, *14*, 5695-5701.

(34)   Berciaud, S.; Cognet, L.; Tamarat, P.; Lounis, B. Observation of Intrinsic Size Effects in the Optical Response of Individual Gold Nanoparticles. *Nano Lett.* **2005**, *5*, 515–518.

(35)   Kubo, S.; Diaz, A.; Tang, Y.; Mayer, T. S.; Khoo, I. C.; Mallouk, T. E. Tunability of the Refractive Index of Gold Nanoparticle Dispersions. *Nano Lett.* **2007**, *7*, 3418–3423.

(36)   Purcell, E. M.; Pennypacker, C. R. Scattering and Absorption of Light by Nonspherical Dielectric Grains. *Astrophys. J.* **1973**, *186*, 705.

(37)   Draine, B. T.; Flatau, P. J. Discrete-Dipole Approximation for Scattering Calculations. *J. Opt. Soc. Am. A* **1994**, *11*, 1491–1499.

(38)   Hecht, E. *Optics*; Addison-Wesley Longman: Boston, MA, 4th ed., 2002.

(39)   Powell, A. W.; Hjerrild, N.; Watt, A. A. R.; Assender, H. E.; Smith, J. M. Directional Plasmonic Scattering from Metal Nanoparticles in Thin-Film Environments. *Appl. Phys. Lett.* **2014**, *104*, 48–52.

(40)   Zhao, Q.; Zhao, X. P.; Qu, C. Z.; Xiang, L. Q. Diffraction Pattern and Optical Activity of

Complex Fluids under External Electric Field. *Appl. Phys. Lett.* **2004**, *84*, 1985–1987.

(41)   Born, M. *Principles of Optics*; Cambridge University Press: New York, NY, 7th ed., 1999.

(42)   Hu, J.; Li, L.; Lin, H.; Zhang, P.; Zhou, W.; Ma, Z. Flexible Integrated Photonics: Where Materials, Mechanics and Optics Meet. *Opt. Mater. Express* **2013**, *3*, 1313.

(43)   McDonald, J. C.; Whitesides, G. M. Poly(dimethylsiloxane) as a Material for Fabricating Microfluidic Devices. *Acc. Chem. Res.* **2002**, *35*, 491–499.

(44)   Massaro, A.; Spano, F.; Cingolani, R.; Athanassiou, A. Experimental Optical Characterization and Polymeric Layouts of Gold PDMS Nanocomposite Sensor for Liquid Detection. *IEEE Sens. J.* **2011**, *11*, 1780–1786.

(45)   Zhang, Q.; Xu, J.-J.; Liu, Y.; Chen, H.-Y. In-Situ Synthesis of Poly(dimethylsiloxane)–gold Nanoparticles Composite Films and Its Application in Microfluidic Systems. *Lab Chip* **2008**, *8*, 352–357.

(46)   Roper, D. K. Self-Assembly of Nanodroplets in Nanocomposite Materials in Nanodroplets Science and Technology. In *Nanodroplets*; Wang, Z. M., Ed.; Springer: New York, NY, 2013; Vol. 18, pp. 73–97.

(47)   Mie, G. Contributions to the Optics of Turbid Media, Particularly of Colloidal Metal Solutions. *Ann. Phys.* **1908**, *330*, 377–445.

(48)   Martinos, S. S. Comment on Experimental Test of the Mie Theory for Microlithographically Produced Silver Spheres. *Phys. Rev. B* **1989**, *40*, 8558.

(49)   Girifalco, L. A. *Statistical Mechanics of Solids*; Oxford University Press: New York, NY, 2003.

(50)   Roper, D. K.; Ahn, W.; Hoepfner, M. Microscale Heat Transfer Transduced by Surface Plasmon Resonant Gold Nanoparticles. *J. Phys. Chem. C* **2007**, *111*, 3636–3641.

(51)   Lebedev, A. N.; Gartz, M.; Kreibig, U.; Stenzel, O. Optical extinction by spherical particles in an absorbing medium: Application to composite absorbing film. *Eur. Phys. J. D* **1999**, *369*, 365–369.

(52)   Mundy, W. C.; Roux, J. A.; Smith, A. M. Mie Scattering by Spheres in an Absorbing Medium. *J. Opt. Soc. Am.* **1974**, *64*, 1593–1597.

(53)   Levy, O.; Stroud, D. Maxwell Garnett Theory for Mixtures of Anisotropic Inclusions: Application to Conducting Polymers. *Phys. Rev. B* **1997**, *56*, 8035–8046.

(54)   Mallet, P.; Guérin, C. A.; Sentenac, A. Maxwell-Garnett Mixing Rule in the Presence of Multiple Scattering: Derivation and Accuracy. *Phys. Rev. B* **2005**, *72*, 1–9.

(55) Hornyak, G. L.; Patrissi, C. J.; Martin, C. R.; Valmalette, J.; Dutta, J.; Hofmann, H. Dynamical Maxwell-Garnett Optical Modeling of Nanogold-porous Alumina Composites: Mie and Kappa Influence on Absorption Maxima. *NanoStructured Mater.* 1997, 9, 575–578.

(56) Coelho, P. J. The Role of Ray Effects and False Scattering on the Accuracy of the Standard and Modified Discrete Ordinates Methods. *J. Quant. Spectrosc. Radiat. Transf.* **2002**, *73*, 231–238.

(57) Xu, Z.; Yao, Y.; Brueckner, E. P.; Li, L.; Jiang, J.; Nuzzo, R. G.; Liu, G. L. Black Silicon Solar Thin-Film Microcells Integrating Top Nanocone Structures for Broadband and Omnidirectional Light-Trapping. *Nanotechnology* **2014**, *25*, 305301.

(58) Waldron, D. L.; Preske, A.; Zawodny, J. M.; Krauss, T. D.; Gupta, M. C. Lead Selenide Quantum Dot Polymer Nanocomposites. *Nanotechnology* **2015**, *26*, 75705.

(59) Griebel, J. J.; Namnabat, S.; Kim, E. T.; Himmelhuber, R.; Moronta, D. H.; Chung, W. J.; Simmonds, A. G.; Kim, K. J.; Van Der Laan, J.; Nguyen, N. A.; *et al.* New Infrared Transmitting Material via Inverse Vulcanization of Elemental Sulfur to Prepare High Refractive Index Polymers. *Adv. Mater.* **2014**, *26*, 3014–3018.

(60) O'Neill, A.; Khan, U.; Coleman, J. N. Preparation of High Concentration Dispersions of Exfoliated MoS_2 with Increased Flake Size. *Chem. Mater.* **2012**, *24*, 2414–2421.

(61) Swanson, N. L.; Billard, B. D. Optimization of Extinction from Surface Plasmon Resonances of Gold Nanoparticles. *Nanotechnology* **2003**, *14*, 353–357.

(62) Tribelsky, M. I.; Luk'yanchuk, B. S. Anomalous Light Scattering by Small Particles. *Phys. Rev. Lett.* **2006**, *97*, 1–4.

(63) Dunklin, J. R.; Bodinger, C.; Forcherio, G. T.; Roper, D. K. Plasmonic Extinction in Gold Nanoparticle-Polymer Films as Film Thickness and Nanoparticle Separation Decrease below Resonant Wavelength. *J. Nanophotonics* **2017**, *11*, 16002.

(64) Abargues, R.; Abderrafi, K.; Pedrueza, E.; Gradess, R.; Marqués-Hueso, J.; Valdés, J. L.; Martínez-Pastor, J. Optical Properties of Different Polymer Thin Films Containing in Situ Synthesized Ag and Au Nanoparticles. *New J. Chem.* **2009**, *33*, 1720.

(65) Guérin, C.-A.; Mallet, P.; Sentenac, A. Effective-Medium Theory for Finite-Size Aggregates. *J. Opt. Soc. Am. A* **2006**, *23*, 349–358.

(66) Roper, D. K.; Ahn, W.; Taylor, B.; Dall'Asen, A. G. Enhanced Spectral Sensing by Electromagnetic Coupling with Localized Surface Plasmons on Subwavelength Structures. *IEEE Sens. J.* **2010**, *10*, 531–540.

(67) Norman, J. C.; Dejarnette, D. F.; Roper, D. K. Polylogarithm-Based Computation of Fano Resonance in Arrayed Dipole Scatterers. *J. Phys. Chem. C* **2014**, *118*, 627–634.

(68) DeJarnette, D.; Norman, J.; Roper, D. K. Spectral Patterns Underlying Polarization-Enhanced Diffractive Interference Are Distinguishable by Complex Trigonometry. *Appl. Phys. Lett.* **2012**, *101*, 183104.

(69) Forcherio, G. T.; Roper, D. K. Optical Attenuation of Plasmonic Au-PDMS Nanocomposite Thin-Film Devices. *Appl. Opt.* **2013**, *52*, 6417–6427.

(70) Malasi, A.; Kalyanaraman, R.; Garcia, H. From Mie to Fresnel through Effective Medium Approximation with Multipole Contributions. *J. Opt.* **2014**, *16*, 65001.

(71) Kats, M. A.; Blanchard, R.; Ramanathan, S.; Capasso, F. Thin-Film Interference in Lossy, Ultra-Thin Layers. *Opt. Photonics News* **2014**, *25*, 40–47.

(72) Mejdoubi, A.; Malki, M.; Essone Mezeme, M.; Sekkat, Z.; Bousmina, M.; Brosseau, C. Optical Scattering and Electric Field Enhancement from Core-Shell Plasmonic Nanostructures. *J. Appl. Phys.* **2011**, *110*.

(73) Draine, B. T.; Flatau, P. J. Discrete-Dipole Approximation for Periodic Targets: Theory and Tests. *J. Opt. Soc. Am. A* **2008**, *25*, 2693–2703.

(74) Pedrueza, E.; Valdés, J. L.; Chirvony, V.; Abargues, R.; Hernández-Saz, J.; Herrera, M.; Molina, S. I.; Martínez-Pastor, J. P. Novel Method of Preparation of Gold-Nanoparticle-Doped TiO_2 and SiO_2 Plasmonic Thin Films: Optical Characterization and Comparison with Maxwell-Garnett Modeling. *Adv. Funct. Mater.* **2011**, *21*, 3502–3507.

(75) Dunklin, J. R.; Forcherio, G. T.; Roper, D. K. Geometric Optics of Gold Nanoparticle-Polydimethylsiloxane Thin Film Systems. *Opt. Mater. Express* **2014**, *4*, 375.

(76) Fahim, N.; Ouyang, Z.; Zhang, Y.; Jia, B.; Shi, Z.; Gu, M. Efficiency Enhancement of Screen-Printed Multicrystalline Silicon Solar Cells by Integrating Gold Nanoparticles via a Dip Coating Process. *Opt. Mater. Express* **2012**, *2*, 190.

(77) Berry, K. R.; Russell, A. G.; Blake, P. A.; Roper, D. K. Gold Nanoparticles Reduced in Situ and Dispersed in Polymer Thin Films: Optical and Thermal Properties. *Nanotechnology* **2012**, *23*, 11.

(78) Kwon, J. Y.; Lee, D. H.; Chitambar, M.; Maldonado, S.; Tuteja, A.; Boukai, A. High Efficiency Thin Upgraded Metallurgical-Grade Silicon Solar Cells on Flexible Substrates. *Nano Lett.* **2012**, *12*, 5143–5147.

(79) Simpson, T. R. E.; Tabatabaian, Z.; Jeynes, C.; Parbhoo, B.; Keddie, J. L. Influence of Interfaces on the Rates of Crosslinking in Poly(dimethyl Siloxane) Coatings. *J. Polym. Sci. A* **2004**, *42*, 1421–1431.

(80) Allen, M. S.; Allen, J. W.; Wenner, B. R.; Look, D. C.; Leedy, K. D. Application of Highly Conductive ZnO to the Excitation of Long-Range Plasmons in Symmetric Hybrid Waveguides. *Opt. Eng.* **2013**, *52*, 64603.

(81) Maxwell Garnett, J. C. XII. Colous in Metal Glasses and in Metallic Films. *Philos. Trans. R. Soc. A* **1904**, *203*, 385–420.

(82) Niklasson, G. A.; Granqvist, C. G.; Hunderi, O. Effective Medium Models for the Optical Properties of Inhomogeneous Materials. *Appl. Opt.* **1981**, *20*, 26.

(83) Scholl, J. A.; Koh, A. L.; Dionne, J. A. Quantum Plasmon Resonances of Individual Metallic Nanoparticles. *Nature* **2012**, *483*, 421–427.

(84) Nan, C. W. W.; Birringer, R.; Clarke, D. R. R.; Gleiter, H. Effective Thermal Conductivity of Particulate Composites with Interfacial Thermal Resistance. *J. Appl. Phys.* **1997**, *81*, 6692.

(85) Choy, T. C. Effective Medium Theory; Oxford University Press: New York, NY, 2nd ed., 2015.

(86) Jackson, J. Classical Electrodynamics; Wiley: Hoboken, NJ, 3rd ed., 1998.

(87) Fox, M. *Optical Properties of Solids*; Oxford University Press: New York, NY, 2nd ed. 2010.

(88) Rakic, A.D.; Djurisic, A. B.; Elazar, J. M.; Majewski, M. L. Optical Properties of Metallic Films for Vertical-Cavity Optoelectronic Devices. *Appl. Opt.* **1998**, *37*, 5271-5283.

(89) Konig, T. A.; Ledin, P. A.; Kerszulis, J.; Mahmoud, M. A.; El-sayed, M. A.; Reynolds, J. R.; Tsukruk, V. V. Electrically Tunable Plasmonic Behavior of Nanocube-Polymer Nanomaterials Induced by a Redox-Active Electrochromic Polymer. *ACS Nano* **2014**, *8*, 6182–6192.

(90) Dow Corning. *Sylgard® 184 Silicone Elastomer Product Information & Data Sheet*; http://www.dowcorning.com/DataFiles/090276fe80190b08.pdf, 2014.

(91) Flatau, P. J.; Draine, B. T. Fast near Field Calculations in the Discrete Dipole Approximation for Rectangular Rectilinear Grids. *Opt. Express* **2012**, *20*, 1247–1252.

(92) Forcherio, G. T.; Blake, P.; Seeram, M.; DeJarnette, D.; Roper, D. K. Coupled Dipole Plasmonics of Nanoantennas in Discontinuous, Complex Dielectric Environments. *J. Quant. Spectrosc. Radiat. Transf.* **2015**, *166*, 93–101.

(93) Blake, P.; Obermann, J.; Harbin, B.; Roper, D. K. Enhanced Nanoparticle Response from Coupled Dipole Excitation for Plasmon Sensors. *IEEE Sens.* **2011**, *11*, 3332–3340.

(94) DeJarnette, D.; Jang, G. G.; Blake, P.; Roper, D. K. Polarization Angle Affects Energy of Plasmonic Features in Fano Resonant Regular Lattices. *J. Opt.* **2014**, *16*, 105006.

(95) Brann, T.; Patel, D.; Chauhan, R.; James, K. T.; Bates, P. J.; Malik, M. T.; Keynton, R. S.; O'Toole, M. G.; Toole, M. G. O. Gold Nanoplates as Cancer-Targeted Photothermal

Actuators for Drug Delivery and Triggered Release. *J. Nanomater.* **2016**, *2016*.

(96)   Betzer, O.; Ankri, R.; Motiei, M.; Popovtzer, R. Theranostic Approach for Cancer Treatment: Multifunctional Gold Nanorods for Optical Imaging and Photothermal Therapy. *J. Nanomater.* **2015**, *2015*.

(97)   Mendes, M. J.; Morawiec, S.; Mateus, T.; Lyubchyk, A.; Águas, H.; Ferreira, I.; Fortunato, E.; Martins, R.; Priolo, F.; Crupi, I. Broadband Light Trapping in Thin Film Solar Cells with Self-Organized Plasmonic Nano-Colloids. *Nanotechnology* **2015**, *26*, 135202.

(98)   Peng, S.; Zhu, P.; Mhaisalkar, S. G.; Ramakrishna, S. Self-Supporting Three-Dimensional $ZnIn_2S_4$/PVDF-Poly(MMA-Co-MAA) Composite Mats with Hierarchical Nanostructures for High Photocatalytic Activity. *J. Phys. Chem. C* **2012**, *116*, 13849–13857.

(99)   Lisunova, M.; Dunklin, J. R.; Jenkins, S. V.; Chen, J.; Roper, D. K. The Unusual Visible Photothermal Response of Free Standing Multilayered Films Based on Plasmonic Bimetallic Nanocages. *RSC Adv.* **2015**, *5*, 15719–15727.

(100) Wang, X.; Wang, P.; Wang, J.; Hu, W.; Zhou, X.; Guo, N.; Huang, H.; Sun, S.; Shen, H.; Lin, T.; *et al.* Ultrasensitive and Broadband MoS_2 Photodetector Driven by Ferroelectrics. *Adv. Mater.* **2015**, *27*, 6575–6581.

(101) Ann, W.; Roper, D. K. Transformed Gold Island Film Improves Light-to-Heat Transduction of Nanoparticles on Silica Capillaries. *J. Phys. Chem. C* **2008**, *112*, 12214–12218.

(102) Dixon, S. C.; Peveler, W. J.; Noor, N.; Bear, J. C.; Parkin, I. P. Superhydrophobic Au/polymer Nanocomposite Films via AACVD/swell Encapsulation Tandem Synthesis Procedure. *RSC Adv.* **2016**, *6*, 31146–31152.

(103) Link, S.; Wang, Z. L.; El-Sayed, M. A. How Does a Gold Nanorod Melt? *J. Phys. Chem. B* **2000**, *104*, 7867–7870.

(104) Richardson, H. H.; Hickman, Z. N.; Govorov, A. O.; Thomas, A. C.; Zhang, W.; Kordesch, M. E. Thermooptical Properties of Gold Nanoparticles Embedded in Ice: Characterization of Heat Generation and Melting. *Nano Lett.* **2006**, *6*, 783–788.

(105) Keblinski, P.; Cahill, D. G.; Bodapati, A.; Sullivan, C. R.; Taton, T. A. Limits of Localized Heating by Electromagnetically Excited Nanoparticles. *J. Appl. Phys.* **2006**, *100*, 54305.

(106) Govorov, A. O.; Richardson, H. H. Generating Heat with Metal Nanoparticles. *Nano Today* **2007**, *2*, 30–38.

(107) Hoepfner, M. P.; Roper, D. K. Describing Temperature Increases in Plasmon-Resonant Nanoparticle Systems. *J. Therm. Anal. Calorim.* **2009**, *98*, 197–202.

(108) Russell, A. G.; McKnight, M. D.; Sharp, A. C.; Hestekin, J. A.; Roper, D. K. Gold nanoparticles allow optoplasmonic evaporation from open silica cells with a logarithmic approach to steady-state thermal profiles. *J. Phys. Chem. C* **2010**, *114*, 10132-10139.

(109) Russell, A. G.; McKnight, M. D.; Hestekin, J. A.; Roper, D. K. Thermodynamics of Optoplasmonic Heating in Fluid-Filled Gold-Nanoparticle-Plated Capillaries. *Langmuir* **2011**, *27*, 7799–7805.

(110) Berry, K. R.; Dunklin, J. R.; Blake, P. A.; Roper, D. K. Thermal Dynamics of Plasmonic Nanoparticle Composites. *J. Phys. Chem. C* **2015**, *119*, 10550–10557.

(111) Ebadi-Dehaghani, H.; Nazempour, M. Thermal Conductivity of Nanoparticles Filled Polymers. In *Smart Nanoparticles Technology*; Hashim, A., Ed.; 2012; pp. 519–534.

(112) Evans, W.; Prasher, R.; Fish, J.; Meakin, P.; Phelan, P.; Keblinski, P. Effect of Aggregation and Interfacial Thermal Resistance on Thermal Conductivity of Nanocomposites and Colloidal Nanofluids. *Int. J. Heat Mass Transf.* **2008**, *51*, 1431–1438.

(113) Oosthuizen, P. H.. *Natural Convective Heat Transfer from Narrow Plates*; Springer: New York, NY, 2013, *16*, 2177–2187.

(114) Dunklin, J. R.; Roper, D. K. Heat Dissipation of Resonant Absorption in Metal Nanoparticle-Polymer Films Described at Particle Separations near Resonant Wavelength. *J. Nanomater.* **2017**, *2017*, 2753934.

(115) Jiang, K.; Smith, D. A.; Pinchuk, A. Size-Dependent Photothermal Conversion Efficiencies of Plasmonically Heated Gold Nanoparticles. *J. Phys. Chem. C* **2013**, *117*, 27073–27080.

(116) O'Neal, J. T.; Bolen, M. J.; Dai, E. Y.; Lutkenhaus, J. L. Hydrogen-Bonded Polymer Nanocomposites Containing Discrete Layers of Gold Nanoparticles. *J. Colloid Interface Sci.* **2017**, *485*, 260–268.

(117) Mark, J. E. *Polymer Data Handbook*; Oxford University Press: New York, NY, 2nd ed., 2009.

(118) Buschow, K. et al. *Encyclopedia of Materials - Science and Technology*; Pergamon: Oxford, UK, 2001.

(119) Incropera, F. P.; DeWitt, D. P.; Bergman, T. L.; Lavine, A. S. *Fundamentals of Heat and Mass Transfer*; Wiley: Hoboken, NJ, 6th ed., 2006.

(120) Building and Solving a Non-Isothermal Laminar Flow Model. *COMSOL MULTIPHYSICS,* v 3.5, **2008**.

(121) Wang, Q. H.; Kalantar-Zadeh, K.; Kis, A.; Coleman, J. N.; Strano, M. S. Electronics and Optoelectronics of Two-Dimensional Transition Metal Dichalcogenides. *Nat. Nanotechnol.* **2012**, *7*, 699–712.

(122) Lee, K.; Kim, H. Y.; Lotya, M.; Coleman, J. N.; Kim, G. T.; Duesberg, G. S. Electrical Characteristics of Molybdenum Disulfide Flakes Produced by Liquid Exfoliation. *Adv. Mater.* **2011**, *23*, 4178–4182.

(123) Dong, B.; Cao, B.; He, Y.; Liu, Z.; Li, Z.; Feng, Z. Temperature Sensing and in Vivo Imaging by Molybdenum Sensitized Visible Upconversion Luminescence of Rare-Earth Oxides. *Adv. Mater.* **2012**, *24*, 1987–1993.

(124) Lee, K.; Gatensby, R.; McEvoy, N.; Hallam, T.; Duesberg, G. S. High-Performance Sensors Based on Molybdenum Disulfide Thin Films. *Adv. Mater.* **2013**, *25*, 6699–6702.

(125) Lopez-Sanchez, O.; Lembke, D.; Kayci, M.; Radenovic, A.; Kis, A. Ultrasensitive Photodetectors Based on Monolayer MoS_2. *Nat. Nanotechnol.* **2013**, *8*, 497–501.

(126) Nolan, H.; McEvoy, N.; O'Brien, M.; Berner, N. C.; Yim, C.; Hallam, T.; McDonald, A. R.; Duesberg, G. S. Molybdenum Disulfide/pyrolytic Carbon Hybrid Electrodes for Scalable Hydrogen Evolution. *Nanoscale* **2014**, *6*, 8185–8191.

(127) Novoselov, K. S.; Geim, A. K.; Morozov, S. V.; Jiang, D.; Zhang, Y.; Dubonos, S. V.; Grigorieva, I. V.; Firsov, A. A. Electric Field Effect in Atomically Thin Carbon Films. *Science* **2011**, *306*, 666.

(128) Reina, A.; Jia, X.; Ho, J.; Nezich, D.; Son, H.; Bulovic, V.; Dresselhaus, M. S.; Jing, K. Large Area, Few-Layer Graphene Films on Arbitrary Substrates by Chemical Vapor Deposition. *Nano Lett.* **2009**, *9*, 30–35.

(129) Eda, G.; Yamaguchi, H.; Voiry, D.; Fujita, T.; Chen, M.; Chhowalla, M. Photoluminescence from Chemically Exfoliated MoS_2. *Nano Lett.* **2011**, *11*, 5111–5116.

(130) Ferrari, A. C.; Bonaccorso, F.; Falko, V.; Novoselov, K. S.; Roche, S.; Bøggild, P.; Borini, S.; Koppens, F.; Palermo, V.; Pugno, N.; *et al.* Science and Technology Roadmap for Graphene, Related Two-Dimensional Crystals, and Hybrid Systems. *Nanoscale* **2014**, *7*, 4598–4810.

(131) Nicolosi, V.; Chhowalla, M.; Kanatzidis, M. G.; Strano, M. S.; Coleman, J. N. Liquid Exfoliation of Layered Materials. *Science.* **2013**, *340*, 1226419.

(132) Varrla, E.; Backes, C.; Paton, K. R.; Harvey, A.; Gholamvand, Z.; McCauley, J.; Coleman, J. N. Large-Scale Production of Size-Controlled MoS_2 Nanosheets by Shear Exfoliation. *Chem. Mater.* **2015**, *27*, 1129–1139.

(133) Coleman, J. N.; Lotya, M.; O'Neill, A.; Bergin, S. D.; King, P. J.; Khan, U.; Young, K.; Gaucher, A.; De, S.; Smith, R. J.; *et al.* Two-Dimensional Nanosheets Produced by Liquid Exfoliation of Layered Materials. *Science* **2011**, *331*, 568–571.

(134) Hernandez, Y.; Nicolosi, V.; Lotya, M.; Blighe, F.; Sun, Z.; De, S.; McGovern, I. T.; Holland, B.; Byrne, M.; Gunko, Y.; *et al.* High Yield Production of Graphene by Liquid

Phase Exfoliation of Graphite. *Nat. Nanotechnol.* **2008**, *3*, 563–568.

(135) Hanlon, D.; Backes, C.; Higgins, T. M.; Hughes, M.; O'Neill, A.; King, P.; McEvoy, N.; Duesberg, G. S.; Mendoza Sanchez, B.; Pettersson, H.; *et al.* Production of Molybdenum Trioxide Nanosheets by Liquid Exfoliation and Their Application in High-Performance Supercapacitors. *Chem. Mater.* **2014**, *26*, 1751–1763.

(136) Hanlon, D.; Backes, C.; Doherty, E.; Cucinotta, C. S.; Berner, N. C.; Boland, C.; Lee, K.; Harvey, A.; Lynch, P.; Gholamvand, Z.; *et al.* Liquid Exfoliation of Solvent-Stabilized Few-Layer Black Phosphorus for Applications beyond Electronics. *Nat. Commun.* **2015**, *6*, 8563.

(137) Khan, U.; May, P.; O'Neill, A.; Bell, A. P.; Boussac, E.; Martin, A.; Semple, J.; Coleman, J. N. Polymer Reinforcement Using Liquid-Exfoliated Boron Nitride Nanosheets. *Nanoscale* **2013**, *5*, 581–587.

(138) Backes, C.; Smith, R. J.; McEvoy, N.; Berner, N. C.; McCloskey, D.; Nerl, H. C.; O'Neill, A.; King, P. J.; Higgins, T.; Hanlon, D.; *et al.* Edge and Confinement Effects Allow in Situ Measurement of Size and Thickness of Liquid-Exfoliated Nanosheets. *Nat. Commun.* **2014**, *5*, 4576.

(139) Kern, J.; Trügler, A.; Niehues, I.; Ewering, J.; Schmidt, R.; Schneider, R.; Najmaei, S.; George, A.; Zhang, J.; Lou, J.; *et al.* Nanoantenna-Enhanced Light–Matter Interaction in Atomically Thin WS$_2$. *ACS Photonics* **2015**, *2*, 1260–1265.

(140) Bhanu, U.; Islam, M. R.; Tetard, L.; Khondaker, S. I. Photoluminescence Quenching in Gold-MoS$_2$ Hybrid Nanoflakes. *Sci. Rep.* **2014**, *4*, 5575.

(141) Brongersma, M. L.; Halas, N. J.; Nordlander, P. Plasmon-Induced Hot Carrier Science and Technology. *Nat. Nanotechnol.* **2015**, *10*, 25–34.

(142) Niu, L.; Coleman, J. N.; Zhang, H.; Shin, H.; Chhowalla, M.; Zheng, Z. Production of Two-Dimensional Nanomaterials via Liquid-Based Direct Exfoliation. *Small* **2016**, *12*, 272–293.

(143) Zhang, H. Ultrathin Two-Dimensional Nanomaterials. *ACS Nano* **2015**, *9*, 9451–9469.

(144) Huang, X.; Tan, C.; Yin, Z.; Zhang, H. Hybrid Nanostructures Based on Two-Dimensional Nanomaterials. *Adv. Mater.* **2014**, *26*, 2185–2204.

(145) Li, H.; Wu, J.; Yin, Z.; Zhang, H. Preparation and Applications of Mechanically Exfoliated Single-Layer and Multilayer MoS$_2$ and WSe$_2$ Nanosheets. *Acc. Chem. Res.* **2014**, *47*, 1067–1075.

(146) Yin, Z.; Chen, B.; Bosman, M.; Cao, X.; Chen, J.; Zheng, B.; Zhang, H. Au Nanoparticle-Modified MoS$_2$ Nanosheet-Based Photoelectrochemical Cells for Water Splitting. *Small* **2014**, *10*, 3537–3543.

(147) Kang, Y.; Gong, Y.; Hu, Z.; Li, Z.; Qiu, Z.; Zhu, X.; Ajayan, P. M.; Fang, Z. Plasmonic Hot

Electron Enhanced MoS$_2$ Photocatalysis in Hydrogen Evolution. *Nanoscale* **2015**, *7*, 4482–4488.

(148) Yang, X.; Liu, W.; Xiong, M.; Zhang, Y.; Liang, T.; Yang, J.; Xu, M.; Ye, J.; Chen, H. Au Nanoparticles on Ultrathin MoS$_2$ Sheets for Plasmonic Organic Solar Cells. *J. Mater. Chem. A* **2014**, *2*, 14798–14806.

(149) Sobhani, A.; Lauchner, A.; Najmaei, S.; Ayala-Orozco, C.; Wen, F.; Lou, J.; Halas, N. J. Enhancing the Photocurrent and Photoluminescence of Single Crystal Monolayer MoS$_2$ with Resonant Plasmonic Nanoshells. *Appl. Phys. Lett.* **2014**, *104*, 1–5.

(150) Miao, J.; Hu, W.; Jing, Y.; Luo, W.; Liao, L.; Pan, A.; Wu, S.; Cheng, J.; Chen, X.; Lu, W. Surface Plasmon-Enhanced Photodetection in Few Layer MoS$_2$ Phototransistors with Au Nanostructure Arrays. *Small* **2015**, *11*, 2392–2398.

(151) Manjavacas, A.; Liu, J. G.; Kulkarni, V.; Nordlander, P. Plasmon-Induced Hot Carriers in Metallic Nanoparticles. *ACS Nano* **2014**, *8*, 7630–7638.

(152) Dunklin, J. R.; Lafargue, P.; Vaynzof, Y.; Higgins, T. M.; Forcherio, G. T.; Benamara, M.; Roper, K.; Coleman, J. N.; Backes, C. Exploiting the Redox Edge Chemistry of Liquid-Exfoliated 2H-WS$_2$ to Yield Highly Monolayer-Rich Gold Decorated Nanosheets in Dispersion. *Nat. Chem.* **2017**, *Submitted*.

(153) Backes, C.; Szydłowska, B. M.; Harvey, A.; Yuan, S.; Vega-Mayoral, V.; Davies, B. R.; Zhao, P.; Hanlon, D.; Santos, E. J. G.; Katsnelson, M. I.; *et al.* Production of Highly Monolayer Enriched Dispersions of Liquid-Exfoliated Nanosheets by Liquid Cascade Centrifugation. *ACS Nano* **2016**, *10*, 1589–1601.

(154) Su, S.; Zhang, C.; Yuwen, L.; Chao, J.; Zuo, X.; Liu, X.; Song, C.; Fan, C.; Wang, L. Creating SERS Hot Spots on MoS$_2$ Nanosheets with in Situ Grown Gold Nanoparticles. *ACS Appl. Mater. Interfaces* **2014**, *6*, 18735–18741.

(155) Zhang, P.; Lu, X.; Huang, Y.; Deng, J.; Zhang, L.; Ding, F.; Su, Z.; Wei, G.; Schmidt, O. G. MoS$_2$ Nanosheets Decorated with Gold Nanoparticles for Rechargeable Li-O$_2$ Batteries. *J. Mater. Chem. A* **2015**, *3*.

(156) Fan, C.; Wang, L. Gold Nanoparticle-Decorated MoS$_2$ Nanosheets for Simultaneous Detection of Ascorbic Acid, Dopamine and Uric Acid. *RSC Adv.* **2014**, *4*, 27625–27629.

(157) Su, S.; Sun, H.; Xu, F.; Yuwen, L.; Fan, C.; Wang, L. Direct Electrochemistry of Glucose Oxidase and a Biosensor for Glucose Based on a Glass Carbon Electrode Modified with MoS$_2$ Nanosheets Decorated with Gold Nanoparticles. *Microchim. Acta* **2014**, *181*, 1497–1503.

(158) Su, S.; Sun, H.; Xu, F.; Yuwen, L.; Wang, L. Highly Sensitive and Selective Determination of Dopamine in the Presence of Ascorbic Acid Using Gold Nanoparticles-Decorated MoS$_2$ Nanosheets Modified Electrode. *Electroanalysis* **2013**, *25*, 2523–2529.

(159) Huang, X.; Zeng, Z.; Bao, S.; Wang, M.; Qi, X.; Fan, Z.; Zhang, H. Solution-Phase Epitaxial Growth of Noble Metal Nanostructures on Dispersible Single-Layer Molybdenum Disulfide Nanosheets. *Nat. Commun.* **2013**, *4*, 1444.

(160) Shi, Y.; Huang, J.-K.; Jin, L.; Hsu, Y.-T.; Yu, S. F.; Li, L.-J.; Yang, H. Y. Selective Decoration of Au Nanoparticles on Monolayer MoS₂ Single Crystals. *Sci. Rep.* **2013**, *3*, 1839.

(161) Cao, W.; Pankratov, V.; Huttula, M.; Shi, X. Y.; Saukko, S.; Huang, Z. J.; Zhang, M. Gold Nanoparticles on MoS₂ Layered Crystal Flakes. *Mater. Chem. Phys.* **2015**, *158*, 89–95.

(162) Blake, P.; Ahn, W.; Roper, D. K. Enhanced Uniformity in Arrays of Electroless Plated Spherical Gold Nanoparticles Using Tin Presensitization. *Langmuir* **2010**, *26*, 1533–1538.

(163) Forcherio, G. T.; Roper, D. K. Spectral Characteristics of Noble Metal Nanoparticle-Molybdenum Disulfide Heterostructures. *Adv. Opt. Mater.* **2016**, *4*, 1288–1294.

(164) Najmaei, S.; Mlayah, A.; Arbouet, A.; Girard, C.; Léotin, J.; Lou, J. Plasmonic Pumping of Excitonic Photoluminescence in Hybrid MoS₂-Au Nanostructures. *ACS Nano* **2014**, *8*, 12682–12689.

(165) Mak, K. F.; Lee, C.; Hone, J.; Shan, J.; Heinz, T. F. Atomically Thin MoS₂: A New Direct-Gap Semiconductor. *Phys. Rev. Lett.* **2010**, *105*, 136805.

(166) Choi, S. Y.; Yip, C. T.; Li, G.-C.; Lei, D. Y.; Fung, K. H.; Yu, S. F.; Hao, J. Photoluminescence Enhancement in Few-Layer WS₂ Films via Au Nanoparticles. *AIP Adv.* **2015**, *5*, 67148.

(167) Li, Y.; Chernikov, A.; Zhang, X.; Rigosi, A.; Hill, H. M.; Van Der Zande, A. M.; Chenet, D. A.; Shih, E. M.; Hone, J.; Heinz, T. F. Measurement of the Optical Dielectric Function of Monolayer Transition-Metal Dichalcogenides: MoS₂, MoSe₂, WS₂, and WSe₂. *Phys. Rev. B - Condens. Matter Mater. Phys.* **2014**, *90*, 205422.

(168) Liu, B.; Chen, L.; Liu, G.; Abbas, A. N.; Fathi, M.; Zhou, C. High-Performance Chemical Sensing Using Schottky-Contacted Chemical Vapor Deposition Grown Monolayer MoS₂ Transistors. *ACS Nano* **2014**, *8*, 5304–5314.

(169) Yu, Y.; Ji, Z.; Zu, S.; Du, B.; Kang, Y.; Li, Z.; Zhou, Z.; Shi, K.; Fang, Z. Ultrafast Plasmonic Hot Electron Transfer in Au Nanoantenna/MoS₂ Heterostructures. *Adv. Funct. Mater.* **2016**, *26*, 6394–6401.

(170) Forcherio, G. T.; Benamara, M.; Roper, D. K. Electron Energy Loss Spectroscopy of Hot Electron Transport between Gold Nanoantennas and Molybdenum Disulfide by Plasmon Excitation. *Adv. Opt. Mater.* **2016**, *5*, 1600572.

(171) Forcherio, G. T.; Dunklin, J. R.; Backes, C.; Vaynzof, Y.; Benamara, M.; Roper, D. K. Gold Nanoparticles Physicochemically Bonded onto Tungsten Disulfide Nanosheet Edges

Exhibit Augmented Plasmon Damping. *Appl. Phys. Lett.* **2017**, *Submitted*.

(172) Kociak, M.; Stéphan, O. Mapping Plasmons at the Nanometer Scale in an Electron Microscope. *Chem. Soc. Rev.* **2014**, *43*, 3865–3883.

(173) Li, Z.; Xiao, Y.; Gong, Y.; Wang, Z.; Kang, Y.; Zu, S.; Ajayan, P. M.; Nordlander, P.; Fang, Z. Active Light Control of the MoS_2 Monolayer Exciton Binding Energy. *ACS Nano* **2015**, *9*, 10158–10164.

(174) DeJarnette, D.; Roper, D. K. Electron Energy Loss Spectroscopy of Gold Nanoparticles on Graphene. *J. Appl. Phys.* **2014**, *116*, 54313.

(175) Hoggard, A.; Wang, L. Y.; Ma, L.; Fang, Y.; You, G.; Olson, J.; Liu, Z.; Chang, W. S.; Ajayan, P. M.; Link, S. Using the Plasmon Linewidth to Calculate the Time and Efficiency of Electron Transfer between Gold Nanorods and Graphene. *ACS Nano* **2013**, *7*, 11209–11217.

(176) Merki, D.; Hu, X. Recent Developments of Molybdenum and Tungsten Sulfides as Hydrogen Evolution Catalysts. *Energy Environ. Sci.* **2011**, *4*, 3878.

(177) Bigelow, N. W.; Vaschillo, A.; Iberi, V.; Camden, J. P.; Masiello, D. J. Characterization of the Electron- and Photon-Driven Plasmonic Excitations of Metal Nanorods. *ACS Nano* **2012**, *6*, 7497–7504.

(178) Vadukumpully, S.; Paul, J.; Valiyaveettil, S. Cationic Surfactant Mediated Exfoliation of Graphite into Graphene Flakes. *Carbon* **2009**, *47*, 3288–3294.

(179) Smith, R. J.; King, P. J.; Lotya, M.; Wirtz, C.; Khan, U.; De, S.; O'Neill, A.; Duesberg, G. S.; Grunlan, J. C.; Moriarty, G.; *et al.* Large-Scale Exfoliation of Inorganic Layered Compounds in Aqueous Surfactant Solutions. *Adv. Mater.* **2011**, *23*, 3944–3948.

(180) Gutkowicz-Krusin, D.; Draine, B. T. Propagation of Electromagnetic Waves on a Rectangular Lattice of Polarizable Points. *Astrophysics* **2004**, 1–17.

(181) Alcaraz de la Osa, R.; Albella, P.; Saiz, J. M.; Gonzalez, F.; Moreno, F. Extended Discrete Dipole Approximation and Its Application to Bianisotropic Media. *Opt. Express* **2010**, *18*, 23865–23871.

(182) Forcherio, G. T.; DeJarnette, D.; Benamara, M.; Roper, D. K. Electron Energy Loss Spectroscopy of Surface Plasmon Resonances on Aberrant Gold Nanostructures. *J. Phys. Chem. C* **2016**, *120*, 24950–24956.

(183) Johnson, P. B.; Christy, R. W. Optical Constants of the Noble Metals. *Phys. Rev. B* **1972**, *6*, 4370–4379.

(184) Feser, J.; Abder Rahman, S. DDSCAT Convert: A Target Generation Tool, 2016.

(185) Huang, X.; Zeng, Z.; Bao, S.; Wang, M.; Qi, X.; Fan, Z.; Zhang, H. Solution-Phase Epitaxial Growth of Noble Metal Nanostructures on Dispersible Single-Layer Molybdenum Disulfide Nanosheets. *Nat. Commun.* **2013**, *4*, 1444.

(186) Huang, X.; Jain, P. K.; El-Sayed, I. H.; El-Sayed, M. A. Gold Nanoparticles: Interesting Optical Properties and Recent Applications in Cancer Diagnostics and Therapy. *Nanomedicine* **2007**, *2*, 681–693.

(187) Tsai, C. Y.; Chien, H. T.; Ding, P. P.; Chan, B.; Luh, T. Y.; Chen, P. H. Effect of Structural Character of Gold Nanoparticles in Nanofluid on Heat Pipe Thermal Performance. *Mater. Lett.* **2004**, *58*, 1461–1465.

(188) Ferry, V. E.; Verschuuren, M. A.; Li, H. B. T.; Verhagen, E.; Walters, R. J.; Schropp, R. E. I.; Atwater, H. A.; Polman, A. Light Trapping in Ultrathin Plasmonic Solar Cells. *Opt. Express* **2010**, *18*, A237-A245.

(189) Ryu, D.; Loh, K. J.; Ireland, R.; Karimzada, M.; Yaghmaie, F.; Gusman, A. M. In Situ Reduction of Gold Nanoparticles in PDMS Matrices and Applications for Large Strain Sensing. *Smart Struct. Syst.* **2011**, *8*, 471–486.

(190) Adleman, J. R.; Boyd, D. A.; Goodwin, D. G.; Psaltis, D. Heterogenous Catalysis Mediated by Plasmon Heating. *Nano Lett.* **2009**, *9*, 4417–4423.

(191) Shi, J.; Chan-Park, M. B.; Li, C. M. Adhesive-Free Transfer of Gold Patterns to PDMS-Based Nanocomposite Dielectric for Printed High-Performance Organic Thin-Film Transistors. *ACS Appl. Mater. Interfaces* **2011**, *3*, 1880–1886.

(192) U.S. Energy Information Administration. U.S. Energy Facts Explained http://www.eia.gov/energyexplained/?page=us_energy_home (accessed Jan 18, 2017).

(193) Takhtravanchi, M.; Kaghazchi, T.; Kargari, A. Application of Membrane Separation Processes in Petrochemical Industry: A Review. *Desalination* **2009**, *235*, 199–244.

(194) Nagy, E.; Boldyryev, S. Energy Demand of Biofuel Production Applying Distillation And/or Pervaporation. *Chem. Eng. Trans.* **2013**, *35*, 265–270.

(195) Shao, P.; Huang, R. Y. M. Polymeric Membrane Pervaporation. *J. Memb. Sci.* **2007**, *287*, 162–179.

(196) Politano, A.; Cupolillo, A.; Profio, G. Di; Arafat, H. A.; Chiarello, G.; Curcio, E. When Plasmonics Meets Membrane Technology. *J. Phys. Condens. Matter* **2016**, *28*, 363003.

(197) Park, J.; Kim, H. S.; Han, A. Micropatterning of Poly(dimethylsiloxane) Using a Photoresist Lift-off Technique for Selective Electrical Insulation of Microelectrode Arrays. *J. Micromechanics Microengineering* **2009**, *19*, 1–18.

(198) Lukowski, M. A.; Daniel, A. S.; English, C. R.; Meng, F.; Forticaux, A.; Hamers, R. J.; Jin,

S. Highly Active Hydrogen Evolution Catalysis from Metallic WS$_2$ Nanosheets. *Energy Environ. Sci.* **2014**, *7*, 2608–2613.

(199) Kang, Y.; Najmaei, S.; Liu, Z.; Bao, Y.; Wang, Y.; Zhu, X.; Halas, N. J.; Nordlander, P.; Ajayan, P. M.; Lou, J.; *et al.* Plasmonic Hot Electron Induced Structural Phase Transition in a MoS$_2$ Monolayer. *Adv. Mater.* **2014**, *26*, 6467–6471.

(200) Voiry, D.; Yamaguchi, H.; Li, J.; Silva, R.; Alves, D. C. B.; Fujita, T.; Chen, M.; Asefa, T.; Shenoy, V. B.; Eda, G.; *et al.* Enhanced Catalytic Activity in Strained Chemically Exfoliated WS$_2$ Nanosheets for Hydrogen Evolution. *Nat. Mater.* **2013**, *12*, 850–855.

(201) Boyd, R. W.; Terhune, R. W.; Wang, C. C. *Nonlinear Optics*; Academic Press: Cambridge, MA, 3rd ed., 1996.

(202) Janisch, C.; Wang, Y.; Ma, D.; Mehta, N.; Elías, A. L.; Perea-López, N.; Terrones, M.; Crespi, V.; Liu, Z. Extraordinary Second Harmonic Generation in Tungsten Disulfide Monolayers. *Sci. Rep.* **2014**, *4*, 5530.

(203) Cheng, L.; Huang, W.; Gong, Q.; Liu, C.; Liu, Z.; Li, Y.; Dai, H. Ultrathin WS$_2$ Nanoflakes as a High-Performance Electrocatalyst for the Hydrogen Evolution Reaction. *Angew. Chemie - Int. Ed.* **2014**, *53*, 7860–7863.

(204) Yao, M.; Fang, J. Hydrophilic PEO-PDMS for Microfluidic Applications. *J. Micromechanics Microengineering* **2012**, *22*, 25012.

(205) Luk'yanchuk, B.; Zheludev, N. I.; Maier, S. a; Halas, N. J.; Nordlander, P.; Giessen, H.; Chong, C. T. The Fano Resonance in Plasmonic Nanostructures and Metamaterials. *Nat. Mater.* **2010**, *9*, 707–715.

(206) Jang, G. G.; Roper, D. K. Continuous Flow Electroless Plating Enhances Optical Features of Au Films and Nanoparticles. *J. Phys. Chem. C* **2009**, *113*, 19228–19236.

(207) Jaramillo, T. F.; Jørgensen, K. P.; Bonde, J.; Nielsen, J. H.; Horch, S.; Chorkendorff, I. Identification of Active Edge Sites for Electrochemical H$_2$ Evolution from MoS$_2$ Nanocatalysts. *Science* **2007**, *317*, 100–102.

(208) Kim, J.; Byun, S.; Smith, A. J.; Yu, J.; Huang, J. Enhanced Electrocatalytic Properties of Transition-Metal Dichalcogenides Sheets by Spontaneous Gold Nanoparticle Decoration. *J. Phys. Chem. Lett.* **2013**, *4*, 1227–1232.